

ISSN 2074-272X

науково-практичний
журнал

2020/6



EIE Електротехніка і Електромеханіка

Electrical Engineering

& Electromechanics

Електричні машини та апарати
Електротехнічні комплекси та системи
Електроізоляційна та кабельна техніка
Електричні станції, мережі і системи

Журнал включено до найвищої категорії «А»
Переліку фахових видань України

З 2015 р. журнал індексується у міжнародній
наукометричній базі Web of Science
Core Collection: Emerging Sources
Citation Index



«ELECTRICAL ENGINEERING & ELECTROMECHANICS»

SCIENTIFIC JOURNAL

was founded in 2002

Founders:

National Technical University «Kharkiv Polytechnic Institute» (Kharkiv, Ukraine)
State Institution «Institute of Technical Problems of Magnetism of the NAS of Ukraine» (Kharkiv, Ukraine)

EDITORIAL BOARD

Sokol Ye.I.	Editor-in-Chief , Professor, Corresponding member of NAS of Ukraine, Rector of NTU «KhPI», Ukraine
Korytchenko K.V.	Deputy Editor , Professor, National Technical University «Kharkiv Polytechnic Institute» (NTU «KhPI»), Ukraine
Rozov V.Yu.	Deputy Editor , Professor, Corresponding member of NAS of Ukraine, Director of State Institution «Institute of Technical Problems of Magnetism of the NAS of Ukraine» (SI «ITPM NASU»), Kharkiv, Ukraine
Baltag O.	Professor, Grigore T. Popa University Medicine and Pharmacy, Faculty of Medical Bioengineering, Iasi, Romania
Baranov M.I.	Professor, Research and Design Institute «Molniya» of NTU «KhPI», Ukraine
Batygin Yu.V.	Professor, Kharkiv National Automobile and Highway University, Ukraine
Bíró O.	Professor, Institute for Fundamentals and Theory in Electrical Engineering, Graz, Austria
Bolyukh V.F.	Professor, NTU «KhPI», Ukraine
Bouktir T.	Professor, Ferhat Abbas University, Setif 1, Algeria
Buriakovskiy S.G.	Professor, Director of Research and Design Institute «Molniya» of NTU «KhPI», Ukraine
Butkevych O.F.	Professor, Institute of Electrodynamics of NAS of Ukraine (IED of NASU), Kyiv, Ukraine
Colak I.	Professor, Nisantasi University, Istanbul, Turkey
Doležel I.	Professor, University of West Bohemia, Pilsen, Czech Republic
Féliachi M.	Professor, Technological Institute of Saint-Nazaire, University of Nantes, France
Grinchenko V.S.	Ph.D., SI «ITPM NASU», Kharkiv, Ukraine
Gurevich V.I.	Ph.D., Honorable Professor, Central Electrical Laboratory of Israel Electric Corporation, Haifa, Israel
Ida N.	Professor, The University of Akron, Ohio, USA
Kildishev A.V.	Associate Research Professor, Purdue University, USA
Klepikov V.B.	Professor, NTU «KhPI», Ukraine
Korovkin N.	Professor, Peter the Great Saint-Petersburg Polytechnic University, St. Petersburg, Russia
Korzeniewska E.	Professor, Lodz University of Technology, Institute of Electrical Engineering Systems, Poland
Kuznetsov B.I.	Professor, SI «ITPM NASU», Ukraine
Kyrylenko O.V.	Professor, Member of NAS of Ukraine, Director of IED of NASU, Kyiv, Ukraine
Maslov V.I.	Professor, National Science Center «Kharkiv Institute of Physics and Technology», Ukraine
Mi Zou	Ph.D., Chongqing University of Posts and Telecommunications, China
Mikhaylov V.M.	Professor, NTU «KhPI», Ukraine
Milykh V.I.	Professor, NTU «KhPI», Ukraine
Nacke B.	Professor, Gottfried Wilhelm Leibniz Universität, Institute of Electrotechnology, Hannover, Germany
Petrushin V.S.	Professor, Odessa National Polytechnic University, Ukraine
Podoltsev A.D.	Professor, IED of NASU, Kyiv, Ukraine
Rainin V.E.	Professor, Moscow Power Engineering Institute, Russia
Reutskiy S.Yu.	Ph.D., SI «ITPM NASU», Kharkiv, Ukraine
Rezinkin O.L.	Professor, NTU «KhPI», Ukraine
Rezinkina M.M.	Professor, NTU «KhPI», Ukraine
Shcherbak Ya.V.	Professor, NTU «KhPI», Ukraine
Shkolnik A.A.	Ph.D., Central Electrical Laboratory of Israel Electric Corporation, Haifa, Israel
Trichet D.	Professor, Institut de Recherche en Energie Electrique de Nantes Atlantique, Nantes, France
Vaskovskiy Yu.M.	Professor, National Technical University of Ukraine «Igor Sikorsky Kyiv Polytechnic Institute», Kyiv, Ukraine
Vinnikov D.	Professor, Tallinn University of Technology, Estonia
Yagup V.G.	Professor, O.M. Beketov National University of Urban Economy in Kharkiv, Ukraine
Yatchev I.	Professor, Technical University of Sofia, Bulgaria
Zagirnyak M.V.	Professor, Member of NAES of Ukraine, Rector of Kremenchuk M.Ostrohradskiy National University, Ukraine
Zgraja J.	Professor, Institute of Applied Computer Science, Lodz University of Technology, Poland
Grechko O.M.	Executive Managing Editor , Ph.D., NTU «KhPI», Ukraine

Journal «Electrical Engineering & Electromechanics» from no. 1 2015 is indexing in Web of Science Core Collection : Emerging Sources Citation Index (ESCI).

Also included in DOAJ (Directory of Open Access Journals), in EBSCO's database, in ProQuest's databases – Advanced Technologies & Aerospace Database and Materials Science & Engineering Database, in Gale/Cengage Learning databases.

Editorial office address:

National Technical University «Kharkiv Polytechnic Institute», Kyrpychova Str., 2, Kharkiv, 61002, Ukraine
phones: +380 57 7076281, +380 67 3594696, e-mail: a.m.grechko@gmail.com (**Grechko O.M.**)

ISSN (print) 2074-272X
ISSN (online) 2309-3404

© National Technical University «Kharkiv Polytechnic Institute», 2020
© State Institution «Institute of Technical Problems of Magnetism of the NAS of Ukraine», 2020

Printed 24 December 2020. Format 60 × 90 %. Paper – offset. Laser printing. Edition 200 copies.

Printed by Printing house «Madrid Ltd» (18, Gudanova Str., Kharkiv, 61024, Ukraine)



no. 6, 2020

TABLE OF CONTENTS

Electrical Machines and Apparatus

Snitkov K.I., Shabatura Y.V. A method of reducing the error in determining the angular displacements when using inductive sensors 3

Stavinskiy A.A., Tsyganov A.M. Design and technological proposals for improving a single-phase transformer with laminated magnetic core 11

Electrotechnical Complexes and Systems

Khlopenko I.N., Khlopenko N.J., Rozhkov S.A. Analysis and verification of the operation of the stabilizing robust controller's electrical circuit of the rotor flux-linkage control system 18

Lebedev V.A., Zhuk G.V., Ostroverkhov N.J., Khalimovskyy A.M. Control of valve electric drive coordinates of automated welding equipment feed mechanisms 24

Electrical Insulation and Cable Engineering

Palchykov O.O. Breakdown voltage of micron range air inclusions in capacitor paper 30

Power Stations, Grids and Systems

Bourouis B., Djeghloud H., Benalla H. An innovative algorithm for a hybrid FC/battery system energy management 35

Kouadri R., Slimani L., Bouktir T. Slime mould algorithm for practical optimal power flow solutions incorporating stochastic wind power and static VAR compensator device 45

Krasnozhon A.V., Buinyi R.O., Dihtyaruk I.V., Kvytsynskyi A.O. The investigation of distribution of the magnetic flux density of operating two-circuit power line 110 kV «ChTPP-Chernihiv-330» in the residential area and methods of its decreasing to a safe level 55

Lebied R., Lalalou R., Benalla H., Nebti K., Boukhechem I. Ameliorate direct power control of standalone wind energy generation system based on permanent magnet synchronous generator by using fuzzy logic control 63

K.I. Snitkov, Y.V. Shabatura

A METHOD OF REDUCING THE ERROR IN DETERMINING THE ANGULAR DISPLACEMENTS WHEN USING INDUCTIVE SENSORS

Goal. Representation of a special mathematical software for determining the angular displacements of the rotor of the induction angle sensor – resolver (rotating transformer) for applications in which the speed of the sensor's rotor is close to zero. As well as performing its experimental verification. Methodology. The presented method is based on the determination of the phase shift angle of the output signals of the induction sensor, which is determined by comparing the obtained arrangements of signal values with a circular discrete convolution in order to achieve the most precise approximation of the obtained signal values to cosine and sine. The conversion of orthogonal components to an angle is based on the use of a digital phase detector which is use of a software comparator and inverse trigonometric functions. Results. Based on the obtained results of mathematical modeling and experimental research, the characteristic dependencies of the angle of rotation of the rotor of the induction sensor relative to its stator, the nature of which is linear, were obtained. In addition, the estimation of measurement errors of angular displacements is carried out that occur when defining such angles by the method offered. The obtained results of the computer simulation taking into account the high signal noise, as well as the results of experimental investigations, confirm the high precision of this method and the fact that it can be used in systems where high positioning accuracy is required and the speed of the sensor shaft is close to zero. Originality. This article introduces, for the first time, special mathematical software for a new method of determining the angular displacements of the rotor of an induction sensor, which is based on the determination of the orthogonal components of the signal in combination with the use of a circular discrete convolution in the determination of the phase shift angle of the induction sensor signals. Practical meaning. The proposed method does not require the use of demodulators, counters and quadrant tables associated with conventional methods for determining the phase shift of signals. The presented method can be used to measure the full range of $0-2\pi$ angular displacements in real time, is simple and can be easily implemented using digital electronic circuitry. References 9, tables 3, figures 16.

Key words: angular displacements, mathematical method, induction sensor, rotating transformer, circular discrete convolution, orthogonal components, precision, phase shift.

У роботі виконано дослідження нового методу зменшення похибки визначення кутових переміщень за допомогою індукційного давача, його математичне забезпечення та експериментальна перевірка. Представлений метод базується на вимірюванні кута зсуву фаз сигналів давача, визначення якого здійснюється за допомогою співставлення оцифрованих значень сигналів давача із круговою дискретною згорткою та подальшим визначенням їх ортогональних складових. На основі значень отриманих ортогональних складових здійснюється визначення кута за допомогою цифрового детектору фази, в основі роботи якого лежить застосування програмного компаратору та обернених тригонометричних функцій. Запропонований метод не вимагає використання демодуляторів, лічильника та таблиць квадрантів, які асоціюються із традиційними методами визначення кута зсуву фаз сигналів. Представлений метод може бути використаний для вимірювання кутів у діапазоні $0-2\pi$, є простим, і може бути легко реалізований за допомогою цифрових засобів. Бібл. 9, табл. 3, рис. 16.

Ключові слова: кутові переміщення, математичний метод, індукційний давач, обертовий трансформатор, кругова дискретна згортка, ортогональні складові, прецизійність, зсув фази.

В работе выполнено исследование нового метода уменьшения погрешности определения угловых перемещений с помощью индукционного датчика, его математическое обеспечение и экспериментальная проверка. Представленный метод основан на измерении угла сдвига фаз сигналов датчика, определение которого осуществляется с помощью сопоставления оцифрованных значений сигналов датчика с круговой дискретной сверткой и последующим определением их ортогональных составляющих. На основе значений полученных ортогональных составляющих осуществляется определение угла с помощью цифрового детектора фазы, в основе работы которого лежит применение программного компаратора и обратных тригонометрических функций. Предложенный метод не требует использования демодуляторов, счетчика и таблиц квадрантов, которые ассоциируются с традиционными методами определения угла сдвига фаз сигналов. Представленный метод может быть использован для измерения углов в диапазоне $0-2\pi$, является простым, и может быть легко реализован с помощью цифровых средств. Библ. 9, табл. 3, рис. 16.

Ключевые слова: угловые перемещения, математический метод, индукционный датчик, вращающийся трансформатор, круговая дискретная свертка, ортогональные составляющие, точность, сдвиг фазы.

Introduction. Today, in many fields of science and technology as devices that provide information about the current state of the actuators, angle measuring systems are widely used. In most cases, especially for devices and mechanisms that work in extreme conditions, electromechanical sensors (angle sensors) are used, the work of which is aimed at converting angular displacements into an information signal.

As is known from [1] to determine the angular displacements, there are a large number of types of sensors, such as: optical encoder, gyroscopic sensors,

magnetic encoder, and induction sensors. However, the use of the above types of sensors in angular measurement systems should be used taking into account the purpose of such systems, environmental conditions and requirements for their accuracy. There is no doubt that today optical encoders have become widely used in angular measuring and positioning systems. However, despite their widespread use, positioning systems continue to operate today, using induction electromechanical transducers as part of the control system, both in the field of armaments

© K.I. Snitkov, Y.V. Shabatura

and military equipment, and in industries. The use of induction electromechanical transducers in the above fields is explained by their ability to operate in difficult operating conditions and unpretentiousness to external conditions [2]. However, along with the positive properties, they also have disadvantages – induction mechanical transducers do not provide high enough accuracy to identify angular displacements. In particular, in tracking systems, positioning systems and automated weapons guidance systems, where such sensors are the main sensors of angular movements. The use of the aforementioned sensors such as optical encoder, electron gyroscope, with the appropriate bit rate, would allow the identification of angular displacements with higher accuracy, the requirements for which, to date, reach tens of angular seconds. However, their use does not meet the above requirements for the operating conditions of such systems. In addition, in the case of modernization of angle measuring systems, which operate on the basis of the use of an induction sensor, by replacing it with modern digital encoder will involve significant financial costs, as well as design changes in the system.

Thus, given the above, there is a need to increase the accuracy of determining the angular displacements using an induction sensor, which is used in existing and advanced angle measuring systems based on the use of special mathematical processing of the information signal of such a sensor.

Analysis of publications. Today, many publications are known, which consider both hardware and software methods and means of determining the angle of rotation of the rotor of the induction sensor, most of which are considered in [3]. The analysis of these publications provides an opportunity to gain knowledge about the existing methods of determining the angular displacements of the induction sensor, as well as to get acquainted with promising areas of future research.

In particular, the use of analog hardware (so-called signal filters), which operate on the basis of the use of R , C elements really do reduce the error of identification of the angle, but with insufficient accuracy. Moreover, its further increase is impossible due to the influence of destabilizing factors, such as temperature, time, frequency, which affect both the parameters of R , C elements and the parameters of the induction angle sensor [4]. Also, digital tools offered by leading electronics manufacturers (e.g. Texas Instruments, Freescale Semiconductor, Analog Devices) have become widespread, as ready-made solutions for processing information signals of the induction converter based on the implementation of simple calculations using modern electronic components in combination with microcontroller technology [5]. Also, in [6], the latest software and hardware method for identifying the angle of rotation of the rotor of the induction sensor, which is based on the use of phase autotuning frequency is proposed. Using the proposed scheme of this software and hardware method, there is no need to demodulate the signal, use a table of quadrants, pulse counters and digital-to-analog converters. However, the error in determining the angles of rotation of the rotor of the sensor when using this method is 0.3 % over the full

range of values 0-360°. Also, such a hardware-software method is based on the proposed scheme, the implementation of which is carried out using simple electronic elements, in particular, resistors, and therefore the ambient temperature factor will affect the accuracy of the identification results.

In [7, 8] methods of converting sensor signals into an angular position based on the application of mathematical calculations using a polynomial of the 3rd order [7], and generating auxiliary sinusoidal signals [8], for the implementation of which semiconductor components and microcontrollers are used are presented. As a result of application of such methods high accuracy of definition of angular positions at high frequency of rotation of a shaft is reached. However, in the above methods, it is proposed to demodulate the sine and cosine signals to determine the angle of rotation, and therefore it is assumed that the sensor shaft must rotate at a given speed required to modulate these signals. Based on the above, the use of such methods is impossible in systems such as stabilization, positioning, or systems using gearless actuators, where the speed of rotation of the sensor shaft is close to zero.

Thus, **the goal of the work** is the development of special mathematical software for determining the angular displacements of the rotor of the induction sensor based on the determination of orthogonal components from the digital values of the sensor signals using circular discrete convolution. Also in the paper the experimental check of the developed special mathematical tool for induction angle measuring sensors in which the speed of rotation of a rotor is close to zero is carried out.

In this work, an induction sensor – resolver (rotating transformer) is used as an angle sensor. The design of such sensors is typical and consists of two windings placed on the stator in the same magnetic system, but their geometric axes are perpendicular to each other. Similarly, the rotor windings are in the same magnetic system and are mutually perpendicular to each other. A typical way to provide excitation of a rotating transformer is to connect one of its stator windings to the mains, and the other winding is short-circuited or connected to a potentiometer, which is implemented in the method considered in [7].

However, **the essence** of the implementation of the **method** proposed by the authors of this work is not to measure the amplitudes of the signal with its subsequent demodulation, but to determine the phase shift between input and output signals, which can be done by connecting both induction windings of the sensor to the power supply of sinusoidal voltages, as shown of (Fig. 1).

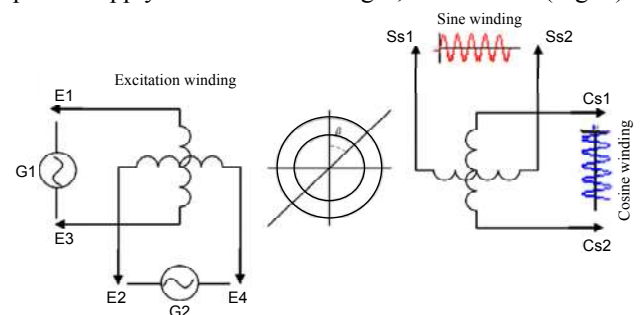


Fig. 1. Configuration of induction sensor windings

Figure 1 shows a diagram of the specified configuration of the windings of the induction sensor – a rotating transformer to determine the phase shift of the output signal depending on the angle of rotation of the rotor of this sensor. The excitation voltage G1, G2, which is equal in amplitude and frequency, but shifted relative to each other by 90°, is applied to the terminals of the excitation winding E1-E3 and E2-E4, respectively, which can be described by the following expressions:

$$G1 = U_{fs} = A \cdot \sin(\omega t), \quad (1)$$

$$G2 = U_{fc} = A \cdot \cos(\omega t), \quad (2)$$

where A is the amplitude of the supply voltage of the sensor, ω is the angular frequency of the excitation signal, t is the time.

Due to the receipt of symmetrical current supply, in the air gap of the magnetic system of the induction sensor there is a rotating magnetic field, the vector of which has a constant value and rotates uniformly with the supply frequency. Then the signals generated on the terminals Ss1-Ss2 of the winding «sine winding» and on the terminals Cs1-Cs2 of the winding «cosine winding» take the form of a sinusoidal voltage of constant frequency, which are shifted in phase relative to the excitation voltage of the sensor, and the phase shift will be determined by the rotation angle of the induction sensor rotor, because the rotation of the magnetic field vector is carried out at a constant speed, so the maxima of the output signals will correspond to the time of passage of the magnetic field vector through the direction of the axis of the longitudinal winding of the induction sensor rotor. The description of the signals on the terminals Ss1-Ss2 of the winding «sine winding» and on the terminals Cs1-Cs2 of the winding «cosine winding» can be made by the following expressions:

$$U_{ss} = k \cdot A \cdot \sin(\omega t + \beta), \quad (3)$$

$$U_{cs} = k \cdot A \cdot \cos(\omega t + \beta), \quad (4)$$

where U_{ss} is the value of the signal at the terminals Ss1-Ss2 of the winding «sine winding», U_{cs} is the value of the signal at the terminals Cs1-Cs2 of the winding «cosine winding», k is the transformation factor, β is the angle of rotation of the rotor relative to the stator (in other words, β is the angle phase shift of the signal winding relative to the excitation winding).

Determination of the rotation angle of the rotor of the induction sensor relative to the stator is based on the method of determining orthogonal components from arrays of values that contain information about the signals of the sensor using a circular discrete convolution, which can be implemented according to the proposed simplified block diagram (Fig. 2).

In Fig. 2 the following notations are accepted: U_{fs} , U_{fc} – analog values of signals coming from the excitation winding and described by expressions (1) and (2); U_{ss} , U_{sc} – analog values of signal windings (3), (4); ADC (analog-to-digital converter) – m -channel analog-to-digital converter (ADC) with N_{ADC} bit rate and sampling frequency f_{adc} ; $U_{DC_{fc}}$, $U_{DC_{fs}}$, $U_{DC_{ss}}$, $U_{DC_{sc}}$ – digital values of signals of excitation windings and signals of signal windings after passing of the ADC block;

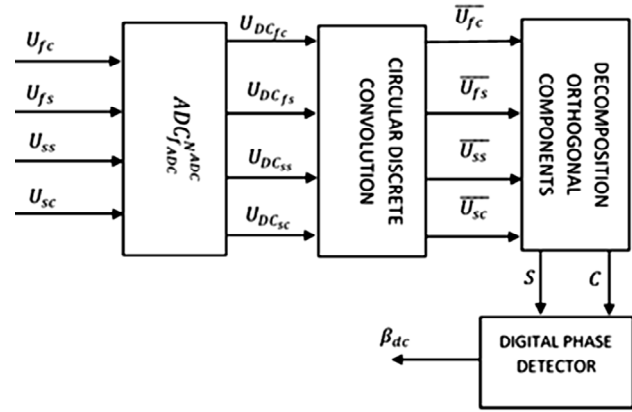


Fig. 2. Simplified block diagram of the proposed method for determining the angular displacements of the induction sensor

Circular Discrete Convolution – a block for forming a discrete convolution of the signal by multiplying the arrays, which are formed on the basis of the values of the signals obtained from the sensor windings with the values of the generated sinusoidal signals; $\overline{U_{fc}}$, $\overline{U_{fs}}$, $\overline{U_{ss}}$, $\overline{U_{sc}}$ – the results of the formation of arrays of values of the circular discrete convolution of the signal of the induction sensor in digital form; Decomposition Orthogonal Components – the block of release of orthogonal components, the result of which calculation is a pair of numbers S and C , which come to the block Digital Phase Detector – the block of digital phase detection. The result of the calculation in the Digital Phase Detector is the angle β_{dc} which is equal to the angle of the rotor position. Thus, as follows from the description of the operation of the above circuit, to implement the proposed method it is involved to use modern means for converting an analog signal into a digital code, as well as the use of microprocessor technology to perform calculations.

The operation of the proposed circuit is as follows: signals U_{fs} , U_{fc} , U_{ss} , U_{sc} which are described by expressions (1)-(4), come to the block $ADC_{f_{ADC}}^{N_{ADC}}$, the operation of which should convert the values of signals as functions of continuous variables into a function of discrete variables as a finite number samples of discrete values. Therefore, the values of the signals after the ADC conversion can be described by the following expressions:

$$U_{DC_{fc}} = A \cdot \frac{\text{trunc}(2^{N_{ADC}-1} \cdot \left(\frac{A + \text{rnd}(\delta) - \frac{\delta}{2}}{A} \right) \cdot \cos(\omega t_{si}))}{2^{N_{ADC}-1}}, \quad (5)$$

$$U_{DC_{fs}} = A \cdot \frac{\text{trunc}(2^{N_{ADC}-1} \cdot \left(\frac{A + \text{rnd}(\delta) - \frac{\delta}{2}}{A} \right) \cdot \sin(\omega t_{si}))}{2^{N_{ADC}-1}}, \quad (6)$$

$$U_{DC_{ss}} = A \cdot \frac{\text{trunc}(2^{N_{ADC}-1} \cdot \left(\frac{A + \text{rnd}(\delta) - \frac{\delta}{2}}{A} \right) \cdot \sin(\omega t_{si} + \beta))}{2^{N_{ADC}-1}}, \quad (7)$$

$$U_{DC_{sci}} = A \cdot \frac{\text{trunc}(2^{N_{ADC}-1} \cdot \left(\frac{A + \text{rnd}(\delta) - \frac{\delta}{2}}{A} \right) \cdot \cos(\omega t_{si} + \beta))}{2^{N_{ADC}-1}}, \quad (8)$$

where $U_{DC_{fci}}$, $U_{DC_{fsi}}$ are the digital values of the signals of the excitation winding of the induction sensor, $U_{DC_{ssi}}$, $U_{DC_{sci}}$ are the digital values of the signals of the sine winding and cosine winding, respectively; *trunc* function is the function of rounding a number to an integer value; *rnd* function is the software generator of random variables; δ is the value of random perturbations, which reaches 1 %, which is known from experimental studies [9], one of the results of such a study is shown in Fig. 3; $2^{N_{ADC}-1}$ is the ADC bit rate is reduced by one bit, which is used to determine the polarity of the function; t_{si} is the signal sampling period, which is determined by the formula:

$$t_{si} = i \cdot T_{adc}, \quad (9)$$

where i is the sequence number of the ADC sample, which takes values from 0 to N_s ; T_{adc} is the ADC reference period:

$$T_{adc} = \frac{1}{f_{adc}}, \quad (10)$$

$$N_s = \frac{f_{adc}}{f}, \quad (11)$$

where f_{adc} is the ADC sampling frequency; f is the excitation frequency of the induction sensor; N_s is the number of ADC samples.

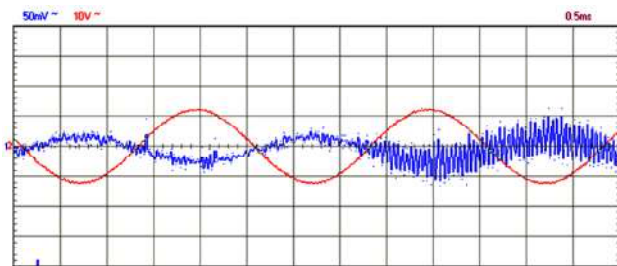


Fig. 3. Influence of random perturbations on the signal amplitude of the induction sensor

The obtained arrays of signal values $U_{DC_{fci}}$, $U_{DC_{fsi}}$, $U_{DC_{ssi}}$, $U_{DC_{sci}}$ are fed to the Circular Discrete Convolution block, in which the signal convolution is formed due to their multiplication with the generated sine function, thus digital signal filtering takes place. Based on this, formation of the signal convolution can be described by the following expressions:

$$\overline{U_{fc_i}} = \sum_{j=0}^{N_s} \left[U_{DC_{fci}} \cdot U_{\sin_i} \begin{cases} i-j, & \text{if } i-j \geq 0 \\ (i-j)+N_s, & \text{otherwise} \end{cases} \right] \cdot \frac{2}{N_s}, \quad (12)$$

$$\overline{U_{fs_i}} = \sum_{j=0}^{N_s} \left[U_{DC_{fsi}} \cdot U_{\sin_i} \begin{cases} i-j, & \text{if } i-j \geq 0 \\ (i-j)+N_s, & \text{otherwise} \end{cases} \right] \cdot \frac{2}{N_s}, \quad (13)$$

$$\overline{U_{ss_i}} = \sum_{j=0}^{N_s} \left[U_{DC_{ssi}} \cdot U_{\sin_i} \begin{cases} i-j, & \text{if } i-j \geq 0 \\ (i-j)+N_s, & \text{otherwise} \end{cases} \right] \cdot \frac{2}{N_s}, \quad (14)$$

$$\overline{U_{sc_i}} = \sum_{j=0}^{N_s} \left[U_{DC_{sci}} \cdot U_{\sin_i} \begin{cases} i-j, & \text{if } i-j \geq 0 \\ (i-j)+N_s, & \text{otherwise} \end{cases} \right] \cdot \frac{2}{N_s}, \quad (15)$$

where

$$U_{\sin_i} = \sin\left(2 \cdot \pi \cdot \frac{i}{N_s}\right). \quad (16)$$

The result of graphical modeling of expressions (12)-(13) is shown in Fig. 4, and expressions (14)-(15) – in Fig. 5.

After filtering through the digital filter of the Circular Discrete Convolution block, the digital signal arrays $\overline{U_{fc_i}}$, $\overline{U_{fs_i}}$, $\overline{U_{ss_i}}$, $\overline{U_{sc_i}}$ arrive at the Decomposition Orthogonal Components block, where they are decomposed into orthogonal components in the form of a pair of numbers S i C and which are essentially vector coordinates in the Cartesian coordinate system:

$$S = \sum_{i=0}^{N_s-1} \left(\overline{U_{ss_i}} \cdot \overline{U_{fs_i}} + \overline{U_{sc_i}} \cdot \overline{U_{fc_i}} \right), \quad (17)$$

$$C = \sum_{i=0}^{N_s-1} \left(\overline{U_{ss_i}} \cdot \overline{U_{fc_i}} - \overline{U_{sc_i}} \cdot \overline{U_{fs_i}} \right), \quad (18)$$

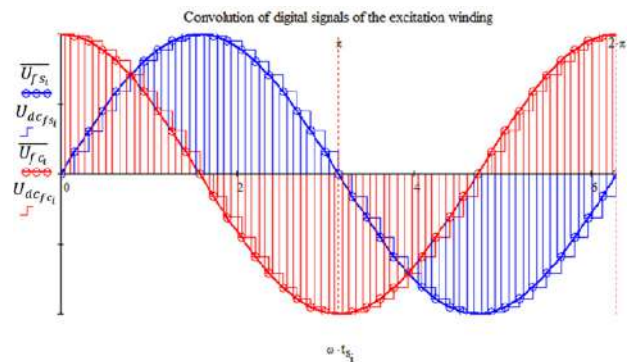


Fig. 4. Graphical representation of circular discrete convolution of digital signals of the excitation winding of the induction sensor

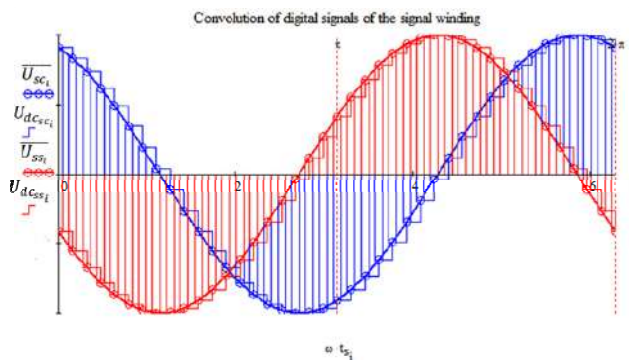


Fig. 5. Graphical representation of circular discrete convolution of digital signals of the signal windings of the induction sensor

To determine the phase shift of the signal, and hence the angle of rotation of the rotor relative to the stator of the sensor, the values of orthogonal components S and C go to the Digital Phase Detector, which converts the coordinates of the vector into the angular value of the rotor position in real time according to the algorithm shown in Fig. 6.

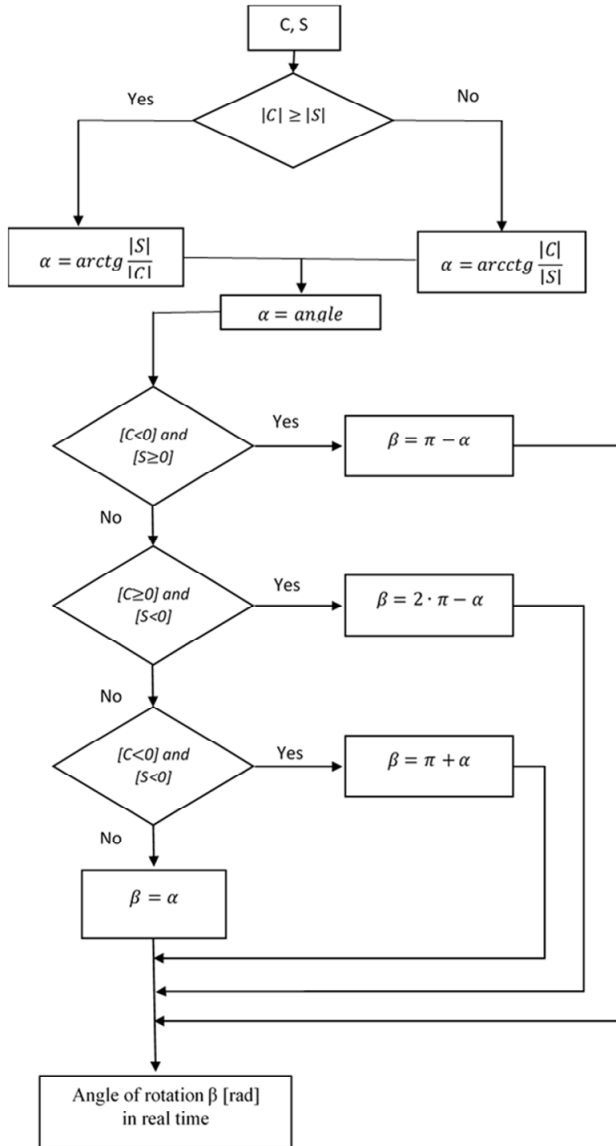


Fig. 6. Algorithm of the Digital Phase Detector block operation

On the basis of expressions (1)-(18) computer simulation was performed using the values of the parameters of real ADC and induction sensor, which are listed in Table 1.

Table 1

ADC and induction sensor parameters		
Parameter	Values	Units
ADC		
Bit rate	2^{16}	Bit
Frequency of samples	$10 \cdot 10^3$	Hz
Induction sensor		
Amplitude of excitation voltage	12	V
Frequency of excitation voltage	400	Hz

The results of this computer simulation are shown in Fig. 7, where φ is the value of the angles that are set, β_s is the value of the angles that are determined.

In addition, the constructed mathematical models allowed to obtain the dependencies of the errors in determining the angle (based on the method of determining orthogonal components using a circular discrete convolution) on the angle of rotation of the rotor of the induction sensor:

$$\delta = \varphi - \beta_s, \quad (19)$$

where δ is the error of determining the angle in absolute values (rad).

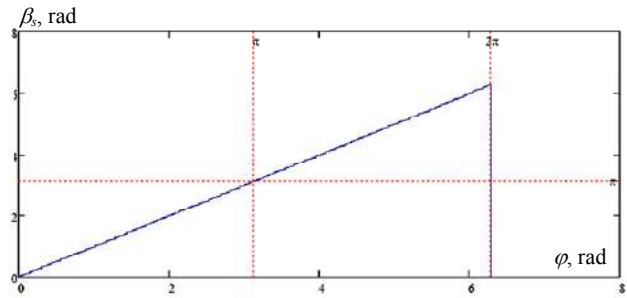


Fig. 7. Dependence of the determined angle β_s on the angle of rotation of the rotor of the induction sensor φ in the full range of angular displacements $0 - 2\pi$

The graphical result of modeling expression (19) is shown in Fig. 8.

Simulation of the error δ dependencies of the angle β_s determination on the angle of rotation of the rotor of the induction sensor φ allows to obtain the value of the root mean square error θ

$$\theta = \sqrt{\frac{1}{N-1} \sum_{i=0}^{N-1} (\delta_i^2)} = 9.73 \cdot 10^{-5} (\text{rad}), \quad (20)$$

where N is the number of defined angles, in the range from 0 to 2π , which in a computer experiment takes the value of 60,000.

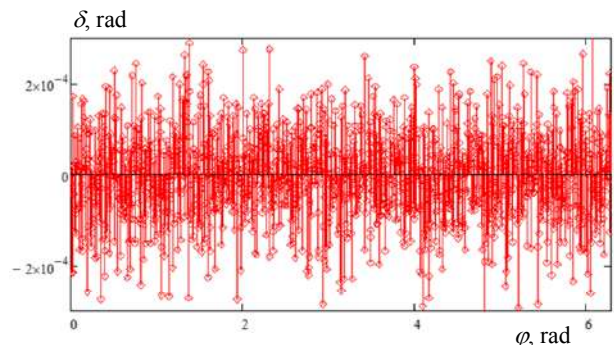


Fig. 8. Dependence of errors δ of the determination of the angle β_s on the angle of rotation of the rotor of the induction sensor φ

Experimental verification of the obtained results.

In order to confirm the results of theoretical modeling of the proposed method, an experimental study was conducted using laboratory equipment, the general view of which is shown in Fig. 9.

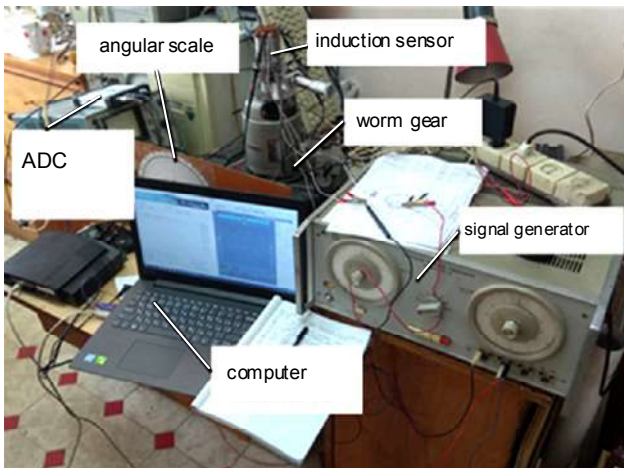


Fig. 9. Experimental equipment for determining angular displacements

The composition of such equipment includes the following components: worm gear (Fig. 10), which is designed to position the exact angles of movement, which consists of a worm wheel (position 1.a in Fig. 10) with 588 teeth and a worm shaft (position 1.b in Fig. 10), connected to an angular scale (Fig. 9), which has 360 divisions. Therefore, the rotation of the worm shaft by 360 divisions of the scale corresponds to the fact that the worm wheel will move by $1.068 \cdot 10^{-2}$ rad. Therefore, moving the worm shaft by one scale division will move the worm wheel by $2.967 \cdot 10^{-5}$ rad.

As an induction sensor (Fig. 9) a rotating transformer VT-5 KF3.031.104 (Fig. 11,a) of accuracy class A, the nominal technical parameters of which correspond to the data of Table 1 was used. Excitation of such a sensor with the required voltage and frequency is carried out using a laboratory two-channel signal generator type G6-26 (Fig. 11,b).

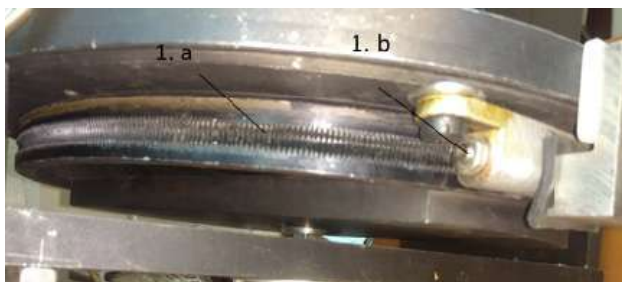


Fig. 10. Worm gear (general view): 1.a – worm wheel; 1.b – worm shaft

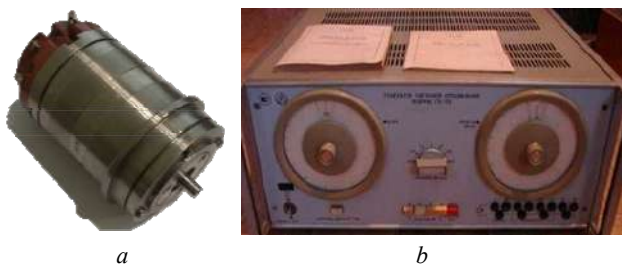


Fig. 11. General view: a – rotating transformer VT-5; b – two-channel signal generator type G6-26

ADC (Fig. 9) and digital oscilloscope INSTRUSTAR ISDS2062B (Fig. 12,a) were used as a converter of input analog signals into a discrete code in the form of an array of values with the subsequent transfer of these arrays via USB interface to a computer (Fig. 9) performing mathematical processing. The MEGATRON M600 optical encoder is also used in the experimental setup for additional control of the accuracy of worm transmission (Fig. 12,b).

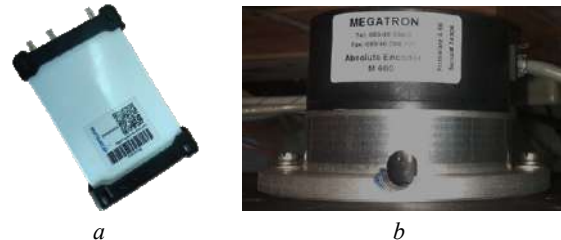


Fig. 12. General view:
a – digital oscilloscope INSTRUSTAR ISDS2062B,
b – optical encoder MEGATRON M600

The description of functioning of experimental installation can be carried out on the basis of use of its structural scheme (Fig. 13).

On the common axis of the installation the worm gear is assembled – 1 (Fig. 13), in which the worm wheel 1.a placed in a horizontal plane with two ends of the output shaft. One end of the output shaft is connected to the rotor of the optical digital encoder 7, and the other end of the output shaft through the adapter is connected to the rotor of the induction sensor of the angle 3. Thus, by rotating the worm shaft 1.b of the worm gear 1, the worm wheel rotates with the output ends of the shaft, and hence the rotation of the rotor of the digital encoder on one side and the rotation of the rotor of the induction sensor on the other side.

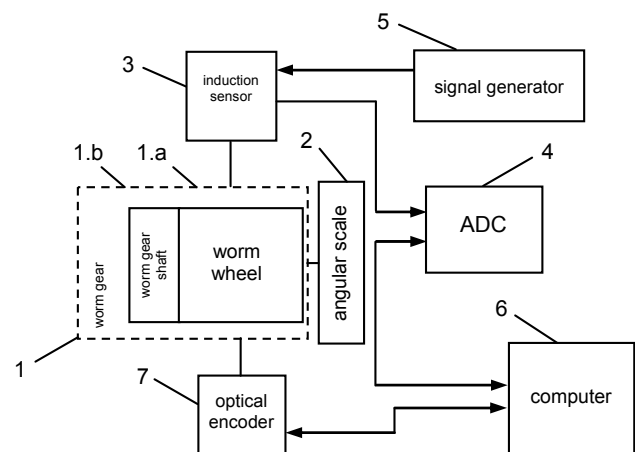


Fig. 13. Block diagram of the experimental installation:
1 – worm gear; 1.a – worm wheel; 1.b – worm gear shaft;
2 – angular scale; 3 – induction sensor; 4 – ADC; 5 – signal generator, 6 – computer, 7 – optical encoder

In turn, the induction sensor 3 receives excitation voltages from the signal generator 5, which are applied to both of its stator windings (excitation windings), and these excitation signals are equal in amplitude and

frequency, but shifted from each other by 90° . To represent the signals in digital form, its windings are connected to ADC 4, the role of which in this installation is performed by a digital oscilloscope, which, in turn, is connected to a computer via a USB interface. Also, a digital optical encoder 7 is connected to the computer for power supply and information exchange via the interface RS-232.

To reflect the results of the study, it was taken into account that in expression (20) as N (number of defined angles) 60,000 values was used, the number of which inevitably affects the root mean square error, but to display this number of experimental values is impossible due to their significant number beyond the scope of this paper. Therefore, the display of the results of determining the angles of rotation of the rotor of the induction sensor relative to its stator will be in the range from 0 to 2π with a step $\pi/4$, which reflects the completeness of the range of determining the values of angles by the proposed method. The results of such a study are given in Table 2, and its graphical representation – in Fig. 14.

Table 2
Results of measuring the angles of rotation of the rotor of the induction sensor in the range from 0 to 2π and the measurement error

Angle of rotation φ , rad	The measurement result by encoder α , rad	The measurement result by the proposed method β , rad	Error, δ rad
0	0	0	0
$\pi/4$	0.7853541	0.785423	$-2.481e-5$
$\pi/2$	1.5707623	1.5707155	$8.078e-5$
$3\pi/4$	2.356187	2.3560015	$1.929e-4$
π	3.1414934	3.1415226	$7.004e-5$
$5\pi/4$	3.9269856	3.9271619	$-1.71e-4$
$3\pi/2$	4.7124053	4.7124368	$-4.781e-5$
$7\pi/4$	5.4977544	5.4979427	$-1.556e-4$
2π	6.2831808	6.2831571	$2.824e-5$

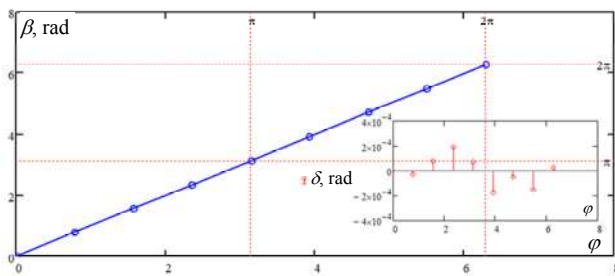


Fig. 14. Dependence of measuring angles β on the angle of rotation of the rotor of the induction sensor φ and the error of their measurements δ

Also, to assess the precision of this method, in the experimental study the values of the angle φ are set in the range from 0 to $2.968 \cdot 10^{-3}$ rad with a step of $1.484 \cdot 10^{-4}$ rad. The results of such studies are given in Table 3. Also Fig. 15 shows the graphical dependencies of the measuring angle β on the angle of rotation of the rotor of the induction sensor φ , and Fig. 16 – dependence of errors δ of the determination of the angle β on the angle of rotation of the rotor of the induction sensor φ .

Table 3
Results of measuring the angles of rotation of the rotor of the induction sensor in the range from 0 to $2.968e-3$ rad

Angle of rotation φ , rad	The measurement result by encoder α , rad	The measurement result by the proposed method β , rad	Error δ , rad
0	0	0	0
$1.484e-4$	$1.5432383e-4$	$3.240248e-4$	$-1.756e-4$
$2.968e-4$	$2.8634171e-4$	$3.9410138e-4$	$-9.73e-5$
$4.452e-4$	$4.4453627e-4$	$6.3563009e-4$	$-1.904e-4$
$5.936e-4$	$5.5750648e-4$	$5.6524419e-4$	$2.835e-5$
$7.42e-4$	$8.1863463e-4$	$1.040776e-3$	$-2.988e-4$
$8.904e-4$	$8.596197e-4$	$6.8755041e-4$	$2.028e-4$
$1.039e-3$	$1.0080408e-3$	$8.3604738e-4$	$2.027e-4$
$1.187e-3$	$1.1244657e-3$	$8.3653092e-4$	$3.507e-4$
$1.336e-3$	$1.2784218e-3$	$1.2367585e-3$	$9.883e-5$
$1.484e-3$	$1.4806882e-3$	$1.6892879e-3$	$-2.053e-4$
$1.632e-3$	$1.5963308e-3$	$1.61913e-3$	$1.325e-5$
$1.781e-3$	$1.7276265e-3$	$1.6229882e-3$	$1.578e-4$
$1.929e-3$	$1.9333049e-3$	$2.0505456e-3$	$-1.214e-4$
$2.078e-3$	$2.0740721e-3$	$2.1002799e-3$	$-2.27e-5$
$2.226e-3$	$2.1709733e-3$	$2.2081033e-3$	$1.787e-5$
$2.374e-3$	$2.3909902e-3$	$2.6908347e-3$	$-3.165e-4$
$2.523e-3$	$2.5283926e-3$	$2.6856021e-3$	$-1.628e-4$
$2.671e-3$	$2.6501764e-3$	$2.7511128e-3$	$-7.994e-5$
$2.82e-3$	$2.7910538e-3$	$2.5065176e-3$	$3.131e-4$
$2.968e-3$	$3.0097617e-3$	$2.9269924e-3$	$4.097e-5$

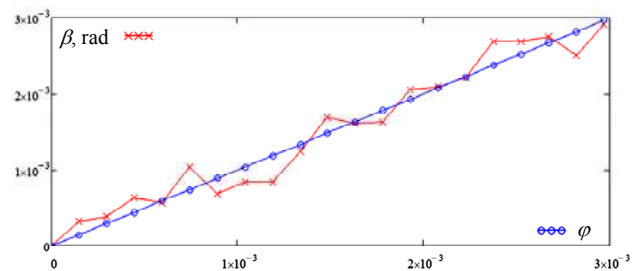


Fig. 15. Dependence of the measuring angle β on the angle of rotation of the rotor of the induction sensor φ

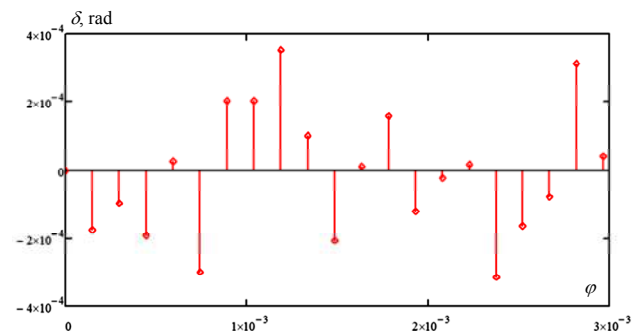


Fig. 16. Dependence of errors δ of the determination of angle β from the angle of rotation of the rotor of the induction sensor φ

The results of the obtained values of errors δ , which are listed in Table 3, with their subsequent substitution in expression (20), allow to estimate the root mean square error of determining the angles of rotation of the rotor of

the induction sensor relative to its stator. The result of this calculation is $1.913e-4$ rad, and thus allows to confirm a sufficiently high precision of the proposed method.

Conclusions.

1. This paper presents special mathematical software for a new method for reducing the error of determining the angular displacements of the rotor of the induction sensor, which is based on determining the angle of phase shift of the signals. This method uses a circular discrete convolution to achieve the most accurate approximation of the obtained signal values to the cosine and sine, respectively. Then the orthogonal components are determined and the phase shift angle in the full range of $0-2\pi$ of angular displacements is determined with the help of a digital detector.

2. The presented results of computer modeling and the results of experimental research are somewhat different, which can be explained by the fact that during the experimental study an analog-to-digital converter of lower bit size than in the mathematical model is used. However, the obtained results of computer simulation taking into account the high level of signal noise and the results of experimental research allow to confirm the high precision of this method and the fact that it can be used in systems where high positioning accuracy is required and the sensor shaft speed is close to zero. .

3. The authors propose software and hardware to solve this problem, and its implementation can be carried out on the basis of the use of commercial analog-to-digital converters and inexpensive microprocessors. However, the parameters of such electronic components will influence on the accuracy and speed of determining the angles of movement of the rotor of the induction sensor by the proposed method, and therefore it involves developing a methodology for choosing hardware and its impact on the accuracy and speed of the angle measurement process which may be the next development of research in this field.

REFERENCES

1. Hicks T., Atherton P. *The Nano Positioning Book: Moving and Measuring to Better Than a Nanometre*. ISTE Publishing Company, 1997. 120 p.

How to cite this article:

Snitkov K.I., Shabatura Y.V. A method of reducing the error in determining the angular displacements when using inductive sensors. *Electrical engineering & electromechanics*, 2020, no. 6, pp. 3-10. doi: 10.20998/2074-272X.2020.6.01.

2. Auger F., Mansouri-Toudert O., Chibah A. Design of advanced resolver-to-digital converters. *Modeling and Simulation of Electric Machines, Converters and Systems. 10th International Conference ELECTRIMACS*. Cergy-Pontoise (France), 6-8 June 2011.

3. Sivappagari C.M.R., Konduru N.R. Review of RDC soft computing techniques for accurate measurement of resolver rotor angle. *Sensors and Transducers*, 2013, vol. 150, no. 3, pp. 1-11.

4. Zavgorodny V.D., Moroz V.I., Petrova O.A. Quantum-mechanical model of induction type angle sensors (Part 4. Analysis of output signal processing methods). *Electrical engineering & electromechanics*, 2003, no. 4, pp. 36-41. (Ukr).

5. Verma A., Chellamuthu A. Design considerations for resolver-to-digital converters in electric vehicles. *Analog Applications Journal*, 2016, vol. Q1, pp. 9-13.

6. Benammar M., Gonzales A.S.P. A Novel PLL Resolver Angle Position Indicator. *IEEE Transactions on Instrumentation and Measurement*, 2016, vol. 65, no. 1, pp. 123-131. doi: 10.1109/TIM.2015.2476280.

7. Wang S., Kang J., Degano M., Buticchi G. A Resolver-to-Digital Conversion Method Based on Third-Order Rational Fraction Polynomial Approximation for PMSM Control. *IEEE Transactions on Industrial Electronics*, 2019, vol. 66, no. 8, pp. 6383-6392, doi: 10.1109/TIE.2018.2884209.

8. Wang Y., Zhu Z., Zuo Z. A Novel Design Method for Resolver-to-Digital Conversion. *IEEE Transactions on Industrial Electronics*, 2014, vol. 62, no. 6, pp. 3724-3731. doi: 10.1109/tie.2014.2375254.

9. Shabatura Y.V., Snitkov C.I., Seredyuk B.O. Mathematical model for determination of angular variables using the angular induction sensor in the phase mode for guiding a typical artillery system. *SDirect24*, 2018, no. 2/(7). Available at: <https://www.sdirect24.org/nato-deep-no-7> (accessed 15 June 2020).

Received 23.09.2020

Accepted 08.11.2020

Published 24.12.2020

K.I. Snitkov¹, adjunct,

Y.V. Shabatura¹, Doctor of Technical Science, Professor,

¹ Hetman Petro Sahaidachnyi National Army Academy,

32, Heroes of Maidan Str., Lviv, 79026, Ukraine,

e-mail: canstantin@gmail.com, shabaturayuriy@gmail.com

A.A. Stavinskiy, A.M. Tsyganov

DESIGN AND TECHNOLOGICAL PROPOSALS FOR IMPROVING A SINGLE-PHASE TRANSFORMER WITH LAMINATED MAGNETIC CORE

Goal. The purpose of the work is to analyze the features and substantiate the advantages of the spatial radial electromagnetic system of a single-phase transformer with rectangular sections of the rods of a charged magnetic circuit. Methodology. Improvement of single-phase transformers is possible by structural-geometric transformations of active elements. The justification of the advantages of such transformations is achieved by the method of invariant objective functions with dimensionless optimization components and universal relative controlled variables. Results. Replacing the rectangular contours of the variants of a planar magnetic circuit with a hexagonal circuit leads to a decrease in the volume of steel and the loss of three angular zones of changes in the direction of the magnetic flux relative to the texture compared to planar counterparts. The separation of the windings into sections with an arrangement on three rods leads to a decrease in the average length of the coil. Originality. A three-core magnetic core can consist of rod and jugular-angular parallelogram plates of anisotropic and isotropic electrical steel. It is advisable to combine a combination of steels by integral welding of billets with subsequent separation into chevron jugular-rod elements. The method called on has developed mathematical models of the mass, cost, and active power losses of variants of a single-phase electromagnetic system of a transformer with rod and armor planar and spatial radial three-core magnetic cores. Practical significance. It was found that the decrease in the extrema of the mass and cost indicators, as well as the calculated decrease, under the condition that the coefficients of additional losses are identical, the extrema of the losses of the single-phase radial three-rod system of the transformer relative to the planar analogue with a bar stocked magnetic wire from anisotropic steel, respectively 13,0-12,3 %, 15,3-10,1 % and 15,1-18,1 % with copper windings and 10,8-10,2 %, 12,8-13,7 % and 12,6-12,3 % with aluminum windings. The main indicators of traditional single-phase systems with rod and armored magnetic circuits differ insignificantly, which is consistent with early known optimization and calculation data of transformers. References 10, tables 4, figures 4.

Key words: single-phase transformer, electromagnetic system options, target functions, a combination of electrical steels, mass, cost, loss.

Розглянута можливість удосконалення однофазних трансформаторів на основі просторової радіальної електромагнітної системи з тристрижневим магнітопроводом. Стрижневі та ярменно-кутові ділянки такого магнітопроводу можуть бути виготовлені з паралелограмних пластин анізотропної і ізотропної сталі та з'єднані інтегральним зварюванням заготовок, що розділяються на шевронні елементи. На основі методу інваріантних цільових функцій з безрозмірними оптимізаційними складовими й універсальними відносними керуваннями змінними розроблено математичні моделі маси, вартості і втрат активної потужності планарних і радіальної систем зі стрижневим, броньовим та тристрижневим шихтованими магнітопроводами з прямокутними перерізами. Отримані безрозмірні числові значення показників технічного рівня вказаних варіантів, що характеризують переваги радіальної тристрижневої електромагнітної системи. Бібл. 10, табл. 4, рис. 4.

Ключові слова: однофазний трансформатор, варіанти електромагнітної системи, цільові функції, комбінація електротехнічних сталей, маса, вартість, втрати.

Рассмотрена возможность усовершенствования однофазных трансформаторов на основе пространственной радиальной электромагнитной системы с трехстрержневым магнитопроводом. Стержневые и ярменно-угловые участки такого магнитопровода могут быть выполнены из параллелограмных пластин анизотропной и изотропной стали и соединены интегральной сваркой в разделяемых на шевронные элементы заготовках. На основе метода инвариантных целевых функций с безразмерными оптимизационными составляющими и универсальными относительными управляемыми переменными разработаны математические модели массы, стоимости и потерь активной мощности планарных и радиальной систем с стержневым, броневым и трехстрержневым шихтованными магнитопроводами с прямоугольными сечениями. Получены безразмерные числовые значения показателей технического уровня указанных вариантов характеризующие преимущества радиальной трехстрержневой электромагнитной системы. Библ. 10, табл. 4, рис. 4.

Ключевые слова: однофазный трансформатор, варианты электромагнитной системы, целевые функции, комбинация электротехнических сталей, масса, стоимость, потери.

Introduction. In the period from 1970 to 2000, the losses of transformers were reduced to 50 % [1]. Further increases in energy costs are constantly driving the reduction of losses. With almost incomplete loading of transformers during the service life, reducing no-load losses becomes a priority. It is also important to reduce the weight and cost of each new development of the transformer [1-8]. The main losses of electricity occur in distribution networks with transformers with power of up to 1000 kV·A, among which a significant part are single-phase transformers. Such transformers are produced mainly with rectangular sections of rod and armored

planar magnetic cores. The powers of transformers with rectangular cross-sections of rods of laminated magnetic circuits have been increasing recently [8]. The structures of single-phase and three-phase planar electromagnetic systems (EMS) have remained unchanged for a century, which is associated with technological conservatism and the rejection of costs for new developments [2, 3, 7]. In connection with the known shortcomings and the practical limit of the development of traditional designs [2-6], as well as in connection with the need for further energy saving, the tasks of finding and justifying the advantages

© A.A. Stavinskiy, A.M. Tsyganov

of new technical solutions for EMS of transformers are important and relevant.

In the majority of modern works systematized in [7], the main methods and directions for improving transformers, as in the past decades, are the use of new electrical materials. Cardinal methods of energy saving in transformer construction are based on complex technologies for the production of composite conductors of windings with "high-temperature" superconductivity and amorphous electrical steel (ES). However, the cost increases significantly, and questions arise about the specifics of the design, operation and assembly of transformer and technological equipment. Such issues and disadvantages include: the exit of the winding from superconductivity after a protective shutdown, a decrease in the magnetic flux density of the nominal mode and saturation, technological sensitivity to mechanical influences and the fragility of a multilayer amorphous tape. New insulating materials for traditional conductors and cooling systems ("cable" and "SF6" transformers) are being created, and the characteristics of anisotropic and isotropic ES are improved.

There is also known a method for improving transformers by transforming the structures and configurations of EMS elements using both traditional and new materials and existing technological capabilities and equipment [2-6].

The problematic issue of transformer construction is the increase in losses of the finished magnetic core relative to the specific losses of ES [1, 4-7]. In twisted magnetic cores, regardless of the texture, the losses increase due to the irregular distribution of the magnetic field in the cross section with different lengths and saturation of the elementary layers of ES. In laminated magnetic cores made of anisotropic ES, regardless of the shape of the joint, a sharp increase in losses in the angular zones of rotation of the magnetic flux relative to the direction of the texture occurs.

The goal of the work is the substantiation of the advantages of the spatial radial EMS of a single-phase transformer with a three-rod laminated magnetic core over traditional planar versions with rectangular cross-sections of the rods.

According to [4-6], reduction of losses is possible on the basis of a combination of brands of different ES in sections or elements of magnetic cores.

Reducing the losses of the corner zones of planar laminated magnetic cores with rectangular winding windows is achieved by a combination and alternation of anisotropic and isotropic ES in the rods and yokes [5]. In this case, the transition of the flow from the rod to the yoke occurs in the isotropic ES, but the losses in the rod and yoke sections from the isotropic ES increase relative to similar anisotropic sections.

A significant reduction in no-load losses is possible by performing all corner sections of the combined magnetic core from isotropic ES and all rod and yoke sections from anisotropic ES. However, such a solution in the variants of the EMS planar topology with rod (Fig. 1) and armored (Fig. 2) magnetic cores doubles the number of joints and increases the additional losses and reactive power losses. The task of overlapping joints and ensuring

the structural integrity of the magnetic core becomes more complicated.

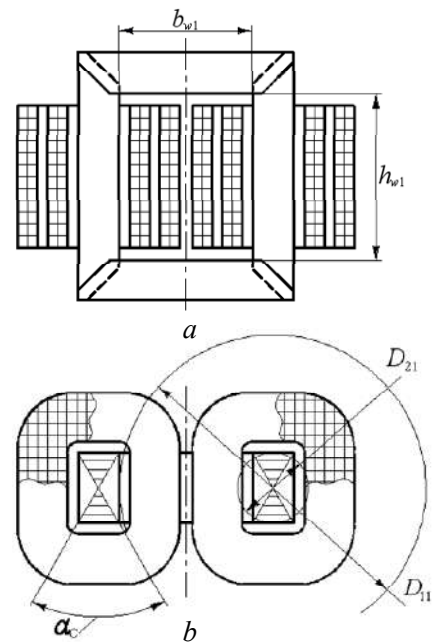


Fig. 1. Single-phase planar electromagnetic system with bar magnetic core in the longitudinal (a) and cross-sections (b)

Replacing the rectangular outer contour of the EMS magnetic core (Fig. 1,a) with the contour of a symmetric hexagon creates a spatial radial EMS with minimum volume of the corner zones of the three-rod magnetic core [2] (Fig. 3). The rectangular sections of the winding coils in the windows of the traditional magnetic core are converted into almost triangular sections (Fig. 3,a). In this case, an increase in the winding sections to three leads to a slight decrease in the average length of a turn of the EMS windings (Fig. 3) relative to the analogs (Fig. 1, 2).

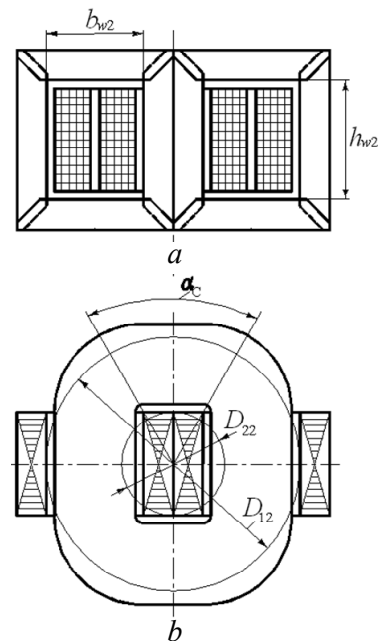


Fig. 2. Single-phase planar electromagnetic system with armored magnetic core in the longitudinal (a) and cross-sections (b)

These features create the prerequisites for improving single-phase EMS. The rhombic configuration of the yoke-angular region creates the minimum mass of the flow turning zones relative to the texture direction. When minimizing the outer EMS contour (Fig. 3), the inner contour can be hexagonal with small central corners of the smaller edges. The connection of the rod and yoke-angular sections, respectively, of anisotropic and isotropic ES forms a magnetic core of chevron elements with a reduction in joints from six to three. Laminating of such elements "interlaced" (Fig. 3,a) leads to rotation of adjacent oblique joints by 180° and solidity of the magnetic circuit. It becomes expedient to solve the problem of permanently joining anisotropic and isotropic sections of chevron plates in joints using a special welding method. Such a joint should reduce current and no-load losses and allow separation of the ES strip.

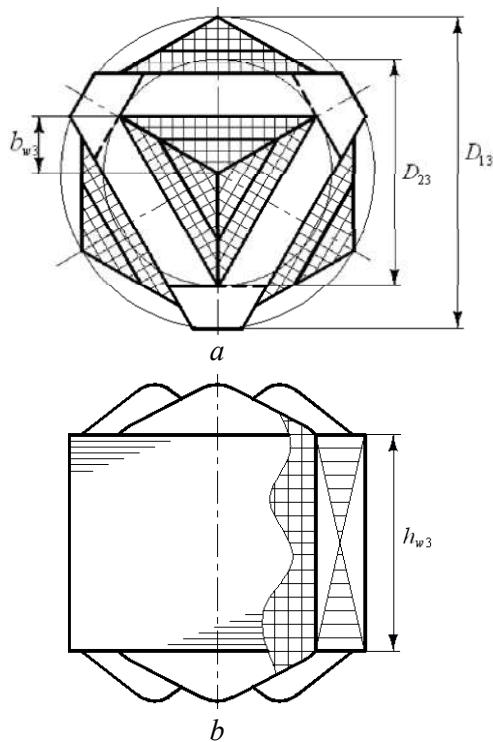


Fig. 3. Single-phase spatial electromagnetic system with three-rod magnetic core in a cross-section (a) and with fragment of a longitudinal section (b)

Elimination of significant complications in the production of magnetic cores with the connection of joints of isotropic and anisotropic ES is possible by integral welding and transverse separation of workpieces. Workpieces of the ES combination for transverse separation into composite plates of the EMS magnetic core (Fig. 3) are formed by combining and joining along the joint lines of fragments of strips of anisotropic (Fig. 4,a) and isotropic (Fig. 4,b) ES. One, two or more fragments of an isotropic ES strip can be welded to a fragment (fragments) of an anisotropic ETS strip. Before joining the fragments, the anisotropic components are located with the texture direction parallel to the separation lines (Fig. 4,c). The separated sections of fragments with two or several seams are divided at specified angles into plates (Fig. 4,d) with a combination of ES.

Assessment of the effect of structural EMS transformations on the characteristics of the transformer should be carried out by the method of invariant structural synthesis.

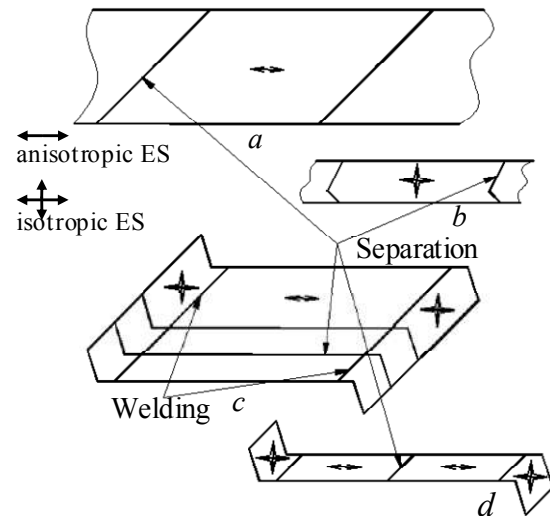


Fig. 4. Components of the combined magnetic core: transverse separation of rolled anisotropic ES (a) and isotropic ES (b) of electrical steels on fragments; welding of fragments along the lines of joints into a workpiece and its transverse division into sections (c); division of sections of fragments into combined plates (d)

The well-known optimization mathematical models of transformers, in particular [1, 9, 10], contain geometrical controlled variables (CV) of EMS elements (diameter of the rod forming contour, aspect ratio of the rectangular cross-section of the rod) and electromagnetic loads (EML). Such models allow performing parametric optimization of transformers of specific powers, structural designs, cooling systems and purposes based on specified criteria. The use of such models complicates the structural synthesis of EMS.

Comparison of EMS options (Fig. 1–3) is carried out by a universal method of structural-parametric synthesis [3, 8]. For a generalized comparison by the named method of any i -th options, in this work the rod ($i=1$), armor ($i=2$) and radial ($i=3$) EMS, ij of objective functions with indicators (components) \hat{I}_{ij}^* of the form [3] in dimensionless (relative) units are used:

$$F_{ijcu(al)} = (I_T)^{3/4} K_j I_{ijcu(al)}^*, \quad (1)$$

where I_T is the indicator of the initial data and EML of the transformer; K_j is the component of the specific characteristics of used ES corresponding to the indicator $\hat{I}_{ijcu(al)}^*$ of the EMS with a copper (aluminum) winding.

The main objective functions of structural (in this work) and structural-parametric synthesis characterize the mass ($j=1$), cost ($j=2$) and active power losses ($j=3$) of the EMS of the transformer. The extrema ($\hat{I}_{ijcu(al)}^*$) of the optimization indicators (1) are determined by numerical calculations. The named extrema represent indicators of the technical level of the i -th variant of EMS [3].

The values of $\hat{I}_{i1(2)cu(al)}^*$ are determined by the filling factor of the winding window with conductive material

K_w (voltage class) and invariant (acceptable for any structures and configurations of EMS elements) relative geometric CVs. The main geometric CVs are determined by the ratio of the sizes of the diameters of the calculated circles of the magnetic core D_{1i} and D_{2i} (Fig. 1–3), as well as by the ratio of the height h_{wi} and the width b_{wi} of the winding window. An additional relative CV used in the part of EMS is the trigonometric function $t(\alpha_c)$ of the central angle of the rod α_c (Fig. 1, c, 2, c):

$$F_{i1(2)cu(al)}^* = f_{i1(2)cu(al)} [K_w, x_c, y_w, t(\alpha_c)]; \quad (2)$$

$$x_c = D_{1j} / D_{2j}; \quad (3)$$

$$y_w = h_{wj} / b_{wj}. \quad (4)$$

The optimization indicator $I_{i3cu(al)}^*$, in addition to the CVs (3), (4), depends on the relative electromagnetic CV losses z_l [3, 8]

$$F_{i3cu(al)}^* = f_{i3cu(al)} [K_w, x_c, y_w, t(\alpha_c), z_l]. \quad (5)$$

The electromagnetic CV is determined by the ratio of the coefficients of the additional short-circuit $K_{lcu(al)}$ and the no-load K_{lc} losses, the ratio of the specific losses of the winding (depends on the specific losses $I_{lcu(al)}^*$ and the current density $J_{wcu(al)}$ of the winding) and the specific losses of ES l_{st} , and also the values of the density of copper (aluminum) $\gamma_{cu(al)}$ and ES γ_{st}

$$z_{lcu(al)} = \frac{K_{lcu(al)} I_{lcu(al)} J_{wcu(al)}^2 \gamma_{cu(al)}}{K_{lc} \gamma_{st} l_{st}}. \quad (6)$$

Mathematical models of optimization comparison (structural synthesis) should provide a comparison of EMS options based on the identity of their electromagnetic power (I_T equality), invariance (universality) of the CV and independence from the conditions of a specific technical specification of parametric synthesis.

These conditions correspond to the objective functions $F_{i1(2)cu(al)}$ (1), the optimization components of which and the optimal geometric EMS ratios according to the particular criteria of the minimums of mass and cost are determined only by the geometric CVs and do not depend on the EML [3]. However, the objective functions $F_{i3cu(al)}$ are additionally determined by the EML. Therefore, in order to exclude the dependence of the generalized structural synthesis on the power, the type of cooling and other design data and limitations, the CV (6) and the value of the $F_{i3cu(al)}^*$ indicator should accordingly change and be determined in a certain real design range of the known minimum and maximum calculated EML values.

For an adequate comparison of EMS (Fig. 1–3), in addition to the identity of I_T , electrical materials, voltage classes, filling factors of the ETS magnetic core K_{st} and the average values of the magnetic flux density amplitudes of the cross-sections of the magnetic core elements are taken accordingly. The real windings of each EMS are replaced by the calculated windings [3] of structurally and configurationally equivalent reactors.

Due to the lack of experimental data on the specific losses of a three-rod magnetic core and a magnetic core of combined connected plates, for a preliminary comparison of the I_{i3}^* indicators, the design of a radial three-rod EMS with three anisotropic parallelogram ES plates in each layer of the magnetic core is adopted. In this case, it is possible to estimate the dependence of losses on the structural features of the EMS (Fig. 1–3) in the same range of variation of the electromagnetic CV (6). The real design range of change of $z_{lcu(al)}$ of transformers calculated using ES 3407 is taken. It is found that such a range of change of the electromagnetic relative CV is identical for copper and aluminum windings [8]

$$3 \leq z_{lcu(al)} \leq 24.$$

Indicators (2), (5) of the objective functions (1) of the rod EMS (Fig. 1) are represented by the equations:

$$I_{i1cu(al)}^* = \left[\frac{8}{\sqrt[4]{\sin \alpha_c K_{st} K_w y_w \left(x_c - \sin \frac{\alpha_c}{2} \right)^2}} \right]^3 \{0,5 K_{st} \times \\ \times \sin \alpha_c \left[\left(x_c - \sin \frac{\alpha_c}{2} \right) 0,5 y_w + \left(x_c - \sin \frac{\alpha_c}{2} \right) + \sin \alpha_c \right] + \\ + K_w y_w \{0,25 \left(x_c - \sin \frac{\alpha_c}{2} \right)^2 [\cos \alpha_c + \sin \alpha_c + \\ + \frac{\pi}{4} \left(x_c - \sin \frac{\alpha_c}{2} \right)]\} \gamma_{wcu(al)} / \gamma_{st} \}; \quad (7)$$

$$I_{i2cu(al)}^* = \left[\frac{8}{\sqrt[4]{\sin \alpha_c K_{st} K_w y_w \left(x_c - \sin \frac{\alpha_c}{2} \right)^2}} \right]^3 \{0,5 K_{st} \times \\ \times \sin \alpha_c \left[\left(x_c - \sin \frac{\alpha_c}{2} \right) 0,5 y_w + \left(x_c - \sin \frac{\alpha_c}{2} \right) + \sin \alpha_c \right] + \\ + K_w y_w \{0,25 \left(x_c - \sin \frac{\alpha_c}{2} \right)^2 [\cos \alpha_c + \sin \alpha_c + \\ + \frac{\pi}{4} \left(x_c - \sin \frac{\alpha_c}{2} \right)]\} C_{wcu(al)} \gamma_{wcu(al)} / (C_{st} \gamma_{st}) \}; \quad (8)$$

$$I_{i3cu(al)}^* = K_{lc} \left[\frac{8}{\sqrt[4]{\sin \alpha_c K_{st} K_w y_w \left(x_c - \sin \frac{\alpha_c}{2} \right)^2}} \right]^3 \times \\ \times \{0,5 K_{st} \sin \alpha_c \left[\left(x_c - \sin \frac{\alpha_c}{2} \right) 0,5 y_w + \left(x_c - \sin \frac{\alpha_c}{2} \right) + \right. \\ \left. + \sin \alpha_c \right] + K_w y_w \{0,25 \left(x_c - \sin \frac{\alpha_c}{2} \right)^2 [\cos \alpha_c + \sin \alpha_c + \right.$$

$$+ \frac{\pi}{4} \left(x_c - \sin \frac{\alpha_c}{2} \right) \left. \right\} z_{lcu(al)} \gamma_{wcu(al)} / \gamma_{st} \left. \right\}. \quad (9)$$

Indicators (2), (5) of the objective functions (1) of the armor EMS (Fig. 2) are determined by the equations:

$$I_{21cu(al)}^* = \left[\sqrt[4]{\frac{8}{\sin \alpha_c K_{st} K_w \gamma_w \left(x_c - \sin \frac{\alpha_c}{2} \right)^2}} \right]^3 \times \left\{ 0,5 K_{st} \sin \alpha_c \left[\left(x_c - \sin \frac{\alpha_c}{2} \right) 0,5 \gamma_w + \left(x_c - \sin \frac{\alpha_c}{2} \right) + \sin \frac{\alpha_c}{2} \right] + K_w \gamma_w \left\{ 0,25 \left(x_c - \sin \frac{\alpha_c}{2} \right)^2 \left[2 \cos \frac{\alpha_c}{2} + 2 \sin \frac{\alpha_c}{2} + \frac{\pi}{2} \left(x_c - \sin \frac{\alpha_c}{2} \right) \right] \right\} \gamma_{wcu(al)} / \gamma_{st} \right\}; \quad (10)$$

$$I_{22cu(al)}^* = \left[\sqrt[4]{\frac{1}{0,5 \sin \alpha_c K_{st} K_w \gamma_w \left(x_c - \sin \frac{\alpha_c}{2} \right)^2}} \right]^3 \times \left\{ 0,5 K_{st} \sin \alpha_c \left[\left(x_c - \sin \frac{\alpha_c}{2} \right) 0,5 \gamma_w + \left(x_c - \sin \frac{\alpha_c}{2} \right) + \sin \frac{\alpha_c}{2} \right] + K_w \gamma_w \left\{ 0,25 \left(x_c - \sin \frac{\alpha_c}{2} \right)^2 \left[\cos \alpha_c + \sin \alpha_c + \frac{\pi}{2} \left(x_c - \sin \frac{\alpha_c}{2} \right) \right] \right\} C_{wcu(al)} \gamma_{wcu(al)} / (C_{st} \gamma_{st}) \right\}; \quad (11)$$

$$I_{23cu(al)}^* = K_{lc} \left[\sqrt[4]{\frac{1}{0,5 \sin \alpha_c K_{st} K_w \gamma_w \left(x_c - \sin \frac{\alpha_c}{2} \right)^2}} \right]^3 \times \left\{ 0,5 K_{st} \sin \alpha_c \left[\left(x_c - \sin \frac{\alpha_c}{2} \right) 0,5 \gamma_w + \left(x_c - \sin \frac{\alpha_c}{2} \right) + \sin \frac{\alpha_c}{2} \right] + K_w \gamma_w \left\{ 0,25 \left(x_c - \sin \frac{\alpha_c}{2} \right)^2 \left[\cos \alpha_c + \sin \alpha_c + \frac{\pi}{2} \left(x_c - \sin \frac{\alpha_c}{2} \right) \right] \right\} z_{lcu(al)} \gamma_{wcu(al)} / \gamma_{st} \right\}. \quad (12)$$

$$+ \sin \frac{\alpha_c}{2} \left. \right\} + K_w \gamma_w \left\{ 0,25 \left(x_c - \sin \frac{\alpha_c}{2} \right)^2 \left[\cos \alpha_c + \sin \alpha_c + \frac{\pi}{2} \left(x_c - \sin \frac{\alpha_c}{2} \right) \right] z_{lcu(al)} \gamma_{wcu(al)} / \gamma_{st} \right\}. \quad (12)$$

The equations of indicators (2), (5) of the objective functions (1) of the radial three-rod EMS (Fig. 3) are as follows:

$$I_{31cu(al)}^* = 2,394 \left[\sqrt[4]{\frac{1}{K_{st} K_w \gamma_w (x_c - 1)}} \right]^3 \left\{ K_w \gamma_w (x_c - 1) \times (x_c + 0,5) + 0,75 K_w \times (y_w + 2x_c - 0,9532) \gamma_{wcu(al)} / \gamma_{st} \right\}; \quad (13)$$

$$I_{32cu(al)}^* = 2,394 \left[\sqrt[4]{\frac{1}{K_{st} K_w \gamma_w (x_c - 1)}} \right]^3 \left\{ K_w \gamma_w (x_c - 1) \times (x_c + 0,5) + 0,75 K_w (y_w + 2x_c - 0,9532) \times C_{wcu(al)} \gamma_{wcu(al)} / C_{st} \gamma_{st} \right\}; \quad (14)$$

$$I_{33cu(al)}^* = 2,394 K_{lc} \left[\sqrt[4]{\frac{1}{K_{st} K_w \gamma_w (x_c - 1)}} \right]^3 \times \left\{ K_{st} \gamma_w (x_c - 1) (x_c + 0,5) + 0,75 K_w \times z_{lcu(al)} (y_w + 2x_c - 0,9532) \right\}. \quad (15)$$

Calculations according to equations (7) – (15) are performed at $K_{st} = 0.97$ and values $K_w = 0.3; 0.25; 0.15$, as well as in real ranges of cost ratios $C_{wcu(al)}$ and C_{st} of copper (aluminum) winding conductors, taking into account insulation and ES:

$$(C_{wcu} / C_{st}) = 3,5 - 5,5; (C_{wal} / C_{st}) = 3 - 4,7.$$

The results of calculations of indicators of the technical level of EMS (Fig. 1–3) are shown in Table 1–4.

From the calculation results of Table 1–4 the potential for improvement of single-phase transformers with laminated magnetic cores based on a spatial radial electromagnetic system with a three-rod magnetic circuit follows.

Table 1

Extreme values of indicators of the mass of options for single-phase electromagnetic systems of transformers with copper and aluminum windings

Designation of mass indicator extremum	Value of mass indicator extremum, at values of winding window fill factor		
	0,3	0,25	0,2
$(I_{11}^*)_{cu}$	20,201	21,234	22,633
$(I_{11}^*)_{al}$	11,841	12,605	13,641
$(I_{21}^*)_{cu}$	20,714	21,941	23,600
$(I_{21}^*)_{al}$	12,747	13,656	14,887
$(I_{31}^*)_{cu}$	17,574	18,544	19,859
$(I_{31}^*)_{al}$	10,556	11,275	12,251

Table 2

Extreme values of indicators of the cost of options for single-phase electromagnetic systems of transformers with copper windings

Designation of cost indicator extremum	Winding window fill factor	Value of cost indicator extremum, at values of ratio of material costs		
		3,5	4,5	5,5
$(I_{12}^*)'_{cu}$	0,3	38,789	44,721	50,229
	0,25	40,205	46,228	51,815
	0,2	42,122	48,271	53,963
$(I_{22}^*)'_{cu}$	0,3	37,694	43,003	47,906
	0,25	39,374	44,215	52,337
	0,2	41,648	47,215	52,337
$(I_{32}^*)'_{cu}$	0,3	32,855	37,687	45,164
	0,25	34,183	39,101	43,651
	0,2	35,982	41,016	45,664

Table 3

Extreme values of indicators of the cost of options for single-phase electromagnetic systems of transformers with aluminum windings

Designation of cost indicator extremum	Winding window fill factor	Value of cost indicator extremum, at values of ratio of material costs		
		3	3,8	4,7
$(I_{12}^*)'_{al}$	0,3	19,268	21,601	24,009
	0,25	20,276	22,671	25,137
	0,2	21,641	24,118	26,664
$(I_{22}^*)'_{al}$	0,3	19,878	22,064	24,303
	0,25	21,075	23,335	25,643
	0,2	22,697	25,055	27,458
$(I_{32}^*)'_{al}$	0,3	16,798	18,736	20,729
	0,25	17,745	19,741	21,788
	0,2	19,028	21,101	23,224

Table 4

Extreme values of indicators of the loss of options for single-phase electromagnetic systems of transformers with copper and aluminum windings

Designation of loss indicator extremum	Winding window fill factor	Value of loss indicator extremum, at values of electromagnetic controlled variable		
		3	8	24
$(I_{13}^*)'_{cu}$	0,3	35,613	62,764	125,456
	0,25	36,975	64,508	127,754
	0,2	38,819	66,868	130,873
$(I_{13}^*)'_{al}$	0,3	19,268	31,663	59,145
	0,25	21,276	32,952	60,846
	0,2	21,64	34,699	63,148
$(I_{23}^*)'_{cu}$	0,3	34,914	59,137	113,562
	0,25	36,531	61,207	116,289
	0,2	38,722	64,011	120,308
$(I_{23}^*)'_{al}$	0,3	19,451	31,329	55,938
	0,25	21,075	32,861	57,957
	0,2	22,697	34,935	60,692
$(I_{33}^*)'_{cu}$	0,3	30,261	52,321	102,786
	0,25	31,539	53,953	104,935
	0,2	33,269	56,165	107,846
$(I_{33}^*)'_{al}$	0,3	16,798	27,027	49,392
	0,25	17,745	28,237	50,985
	0,2	19,028	29,877	53,143

Conclusions.

1. It is found that the decrease in the extrema of the mass and cost indicators, as well as the calculated decrease, with the conditional identity of the additional loss coefficients, the extrema of active power loss of a single-phase radial three-rod EMS of the transformer relative to a planar analogue with a rod laminated magnetic circuit made of anisotropic ES is, respectively, 13-12.3 %, 15.3-10.1 % and 15.1-18.1 % with copper windings and 10.8-10.2 %, 12.8-13.7 % and 12.6-12.3 % with aluminum windings.

2. Decrease in the number and volume of ES of the angular zones of the magnetic core of the radial three-rod EMS relative to traditional planar analogs creates the prerequisites for additional energy saving by reducing the main and additional losses of the magnetic cores; it also seems expedient to combine anisotropic and isotropic ES in the rod and yoke-angular sections.

3. The main technical level indicators of traditional single-phase planar EMS with rod and armored magnetic cores differ insignificantly, which agrees with the previously known optimization and design data of transformers.

REFERENCES

1. Lizunov S.D., Lokhanin A.K. *Power Transformers. A Reference Book*. Moscow, Energoatomizdat Publ., 2004. 616 p. (Rus).
2. Stavinskiy A.A. Evolution of structures and preconditions for transformers and reactors improvement via electromagnetic system circuit transformation (systems with laminated and twisted magnetic circuits). *Electrical engineering & electromechanics*, 2011, no. 6, pp. 33-38. (Rus).
3. Stavinskiy A.A., Stavinskiy R.A., Avdeeva E.A. Optimization comparative analysis of the structures of static electromagnetic systems. Part 1. Variants and a method for evaluating transformations. *Electricity*, 2014, no. 9, pp. 34-43. (Rus).
4. Kefalas T.D., Kladas A.G. Reduction of cost and losses of transformers by using composite magnetic cores. *2014 International Conference on Electrical Machines (ICEM)*, Sep. 2014. doi: 10.1109/icelmach.2014.6960499.
5. Levin M.I., Pentegov I.V., Rymar S.V., Lavreniuk A.V. New approaches at construction of magnetic conductors for mains transformers. *Electrical engineering & electromechanics*, 2015, no. 1, pp. 20-24. doi: 10.20998/2074-272x.2015.1.04. (Rus).
6. Magdaleno-Adame S., Melgoza-Vazquez E., Olivares-Galvan J.C., Escarela-Perez R. Loss reduction by combining electrical steels in the core of power transformers. *International Transactions on Electrical Energy Systems*, 2016, vol. 26, no. 8, pp. 1737-1751. doi: 10.1002/etep.2175.
7. Kostinskiy S.S. The review of the condition of branch of transformer manufacture and tendencies of development of the design of power transformers. *Izvestiya vysshikh uchebnykh zavedenii. Problemy energetiki*, 2018, vol. 20, no. 1-2, pp. 14-32. (Rus). doi: 10.30724/1998-9903-2018-20-1-2-14-32.
8. Stavinskiy A.A., Avdeeva O.A., Tsiganov O.M., Stavinskiy R.A., Sadoviy O.S. Comparison of three-phase transformers with rectangular and circular conversion of laminated magnetic cores (active power losses). *Bulletin of NTU «KhPI». Series: «Electric machines and electromechanical energy conversion»*, 2019, no. 4 (1329), pp. 38-43. (Ukr). doi: 10.20998/2409-9295.2019.4.06.
9. Khatri A., Rahi O.P. Optimal design of transformer: A Compressive bibliographical survey. *International Journal of Scientific Engineering and Technology*, 2012, vol. 1, no. 2, pp. 159-167.
10. Amadi-Echendu J.E., Mafutsana J.M. A bibliographic review of trends in design and management of electrical power transformers. *Proceedings of the 2016 International Conference on Industrial Engineering and Operations Management*. Cuala Lumpur, Malaysia. 10 March, 2016, pp. 2010-2018.

Received 06.09.2020

Accepted 09.10.2020

Published 24.12.2020

A.A. Stavinskiy¹, Doctor of Technical Science, Professor,
A.M. Tsyganov¹, Assistant,
¹Mykolayiv National Agrarian University,
9, George Gongadze Str., Mykolaiv, 54020, Ukraine,
e-mail: andrey.stavynskiy@mnau.edu.ua,
potomkinske@gmail.com

How to cite this article:

Stavinskiy A.A., Tsyganov A.M. Design and technological proposals for improving a single-phase transformer with laminated magnetic core. *Electrical engineering & electromechanics*, 2020, no. 6, pp. 11-17. doi: 10.20998/2074-272X.2020.6.02.

I.N. Khlopenko, N.J. Khlopenko, S.A. Rozhkov

ANALYSIS AND VERIFICATION OF THE OPERATION OF THE STABILIZING ROBUST CONTROLLER'S ELECTRICAL CIRCUIT OF THE ROTOR FLUX-LINKAGE CONTROL SYSTEM

On the basis of the classical theory of robust control, the theory of stability and the theory of continued fractions, the linearized mathematical model, the procedure for calculating and designing an analog electrical circuit of the H_∞ -suboptimal robust controller of the flux-linkage control system of the rotor of an asynchronous electric drive, protected by Ukrainian Patent no.137157, were built. The circuit contains three operational amplifiers, several resistors and capacitors. The proposed mathematical model, the procedure for calculating and choosing the parameters of the resistors and capacitors of the circuit take into account the random variations of the object and the controller within the specified boundaries. An analytical relationship between the transfer function coefficients and the resistances of the resistors and the capacitances of the capacitors of the controller's electrical circuit was established. On a specific example, by calculation according to the developed algorithm, the limiting values of the tolerances of the circuit's resistances of the resistors and capacitances of the capacitors were identified and these values were selected with a margin from the standard series. Analysis of noise filtering by the electrical circuit of the controller in the Multisim package shows its insensitivity to noise spreads within fairly wide boundaries. References 10, table 1, figures 4.

Key words: asynchronous electric drive, flux-linkage control system, robust controller, electrical circuit.

На базі класичної теорії робастного управління, теорії стійкості і теорії ланцюгових дробів побудовано лінеаризована математична модель, процедура розрахунку і проектування аналогової електричної схеми H_∞ -субоптимального робастного регулятора системи управління потокочепленням ротора асинхронного електроприводу, що захищена патентом України № 137157. Схема містить три операційних підсилювача, кілька резисторів і конденсаторів. Запропонована математична модель, процедура розрахунку і вибору параметрів резисторів і конденсаторів схеми враховують випадкові варіації об'єкта і регулятора в заданих межах. Встановлено аналітичний зв'язок між коефіцієнтами передавальної функції і опором резисторів і ємностями конденсаторів електричної схеми регулятора. На конкретному прикладі розрахунковим шляхом за розробленим алгоритмом виявлені граничні значення допусків опорів резисторів і ємностей конденсаторів схеми і здійснений їх вибір із запасом зі стандартних рядів. Аналіз фільтрації завад електричною схемою регулятора в пакеті Multisim показує її нечутливість до розмахів завад у досить широких межах. Бібл. 10, табл. 1, рис. 4.

Ключові слова: асинхронний електропривод, система управління потокочепленням, робастний регулятор, електрична схема.

Introduction. In the patent [1], an analog electrical circuit of the H_∞ -suboptimal robust controller of the flux-linkage control system of the rotor of an asynchronous electric drive is proposed. Its design was carried out in the following sequence. First, a mathematical model of the control object was built and the transfer function of the controller was calculated, as in works [2-4]. Then this function was expanded into a continued fraction [4]. The coefficients of this fraction were used to construct a circuit diagram of the controller. This scheme is made in the form of an active quadripole. This quadripole contains nine resistors and three capacitors. The nominal values of such resistances and capacities of such elements are determined in this work in the process of rounding off their calculated values to the values of standard series [5], and their accuracy is based on the calculation of the stability of the rotor flux-linkage control system with random variations of the parameters of the object, resistors and capacitors of the circuit within the specified boundaries. At the same time, to set the boundaries of random change in the nominal values of resistances and capacitances, the rounding errors of their calculated values and the spread in the values of permissible deviations by standard series are taken into account. An

unreasonable choice of these elements of a high-precision circuit can lead to a significant increase in its cost, and the choice of low accuracy – to a loss of efficiency. A compromise between cost and accuracy can be achieved theoretically only in the process of analyzing the stability of the flux-linkage control system with random variations of the nominal parameters of real circuit elements. However, such an analysis cannot be carried out without determining the analytical relationships between the coefficients of the transfer function of the controller and the parameters of the resistors and capacitors of the circuit, which vary randomly within the specified boundaries. Due to the linearity of the mathematical model of the robust flux-linkage control system [4], such formulas cannot be obtained exactly [6, 7]. Therefore, it is necessary to quickly check the operation of the circuit. It can be done in the interactive package Multisim. Such a check makes it possible to evaluate not only the operability of the designed circuit, but also the level of noise inhibition by this robust controller circuit [8].

The above approach allows solving the considered problem of analyzing and checking the operation of the electrical circuit of the controller. It was proposed by us

© I.N. Khlopenko, N.J. Khlopenko, S.A. Rozhkov

in [4]. However, in this work, only the relationship between the coefficients of the transfer function of the controller and the parameters of its structural scheme was taken into account. Therefore, in this work, this relationship between the coefficients of the transfer function of the H_∞ -suboptimal robust controller and its electrical circuit is taken into account when analyzing and checking the operation of the circuit.

The aim of the work is to analyze and check the operation of the stabilizing H_∞ -suboptimal robust controller's electrical circuit of the rotor flux-linkage control system.

Research methods and results. Consider an undefined control object [4], consisting of a frequency converter and stator and rotor windings of an asynchronous electric motor. Represent the equations of its state in the normal operator matrix form (1):

$$\begin{aligned} px &= Ax + Bu, \\ y &= Cx, \end{aligned} \quad (1)$$

where

$$A = \begin{bmatrix} -\frac{1}{T_2} & \frac{L_{12}I_n}{T_2\Psi_n} & 0 \\ 0 & -\frac{1}{T_{1eq}} & \frac{E_n}{R_{1eq}T_{1eq}I_n} \\ 0 & 0 & -\frac{1}{T_{fc}} \end{bmatrix};$$

$$B = \begin{bmatrix} 0 & 0 & \frac{K_{fc}U_n}{T_{fc}E_n} \end{bmatrix}^T; \quad C = [1 \ 0 \ 0];$$

where p is the Laplace operator; $x=(x_1, x_2, x_3)^T$ is the phase vector, where $x_1=\Psi/\Psi_n$; $x_2=I/I_n$; $x_3=E/E_n$; Ψ is the rotor flux-linkage vector's module; I is the current in the rotor flux-linkage channel; E is the EMF of the frequency converter; $u=U/U_n$ is the control action; U is the controller output voltage; y is the one-dimensional vector of the output, along which the feedback is closed; T_{fc} , K_{fc} are the time constant and gain coefficient of the frequency converter; $T_{1eq}=L_{1eq}/R_{1eq}$ is the electromagnetic time constant of the stator winding, where $R_{1eq}=R_1+(k_r)^2R_2$ and $L_{1eq}=\sigma L_1$ are its equivalent resistance and the leakage inductance; R_1 , R_2 are the active resistances of the stator and rotor windings; $T_2=L_2/R_2$ is the electromagnetic time constant of the rotor winding; L_1 , L_2 are the inductances of stator and rotor windings; L_{12} is the mutual inductance of stator and rotor windings; $k_r=L_{12}/L_2$; $\sigma=1-(L_{12})^2/(L_1L_2)$ is the coefficient of magnetic field scattering.

The extended system of equations [4] with uncertain parameters of the object K_{fc} , R_{1eq} , R_2 , L_1 , L_2 and L_{12} corresponding to Eq. (1) is represented in the form (2):

$$\begin{aligned} px &= Ax + B_1w + B_2u, \\ z &= C_1x + D_{11}w + D_{12}u, \\ y &= C_2x + D_{21}w + D_{22}u, \end{aligned} \quad (2)$$

where

$$A = \begin{bmatrix} -\frac{R_{2n}}{L_{2n}} & \frac{R_{2n}}{L_{2n}} & 0 \\ 0 & -\frac{R_{1eqn}}{L_{1eqn}} & \frac{R_{1eqn}}{L_{1eqn}} \\ 0 & 0 & -\frac{1}{T_{fc}} \end{bmatrix};$$

$$B_1 = \begin{bmatrix} 0 & 0 & 0 & \frac{pR_2}{L_{2n}} & \frac{pL_{12}}{L_{2n}} & -pL_2 & -\frac{pR_2}{L_{2n}} \\ 0 & -pL_{1eq} & -\frac{pR_{1eq}}{L_{1eqn}} & 0 & 0 & 0 & 0 \\ \frac{pK_{fc}}{T_{fc}} & 0 & 0 & 0 & 0 & 0 & 0 \end{bmatrix};$$

$$C_1 = \begin{bmatrix} 0 & 0 & 0 \\ 0 & -\frac{R_{1eqn}}{L_{1eqn}} & \frac{R_{1eqn}}{L_{1eqn}} \\ 0 & R_{1eqn} & 0 \\ 0 & R_{2n} & 0 \\ 0 & R_{2n} & 0 \\ -\frac{R_{2n}}{L_{2n}} & \frac{R_{2n}}{L_{2n}} & 0 \\ R_{2n} & 0 & 0 \end{bmatrix}; \quad C_2 = [1 \ 0 \ 0];$$

$$D_{11} = \begin{bmatrix} 0 & 0 & 0 & 0 & 0 & 0 & 0 \\ 0 & -pL_{1eq} & -\frac{pR_{1eq}}{L_{1eqn}} & 0 & 0 & 0 & 0 \\ 0 & 0 & 0 & 0 & 0 & 0 & 0 \\ 0 & 0 & 0 & 0 & 0 & 0 & 0 \\ 0 & 0 & 0 & pR_2 & 0 & 0 & 0 \\ 0 & 0 & 0 & \frac{pR_2}{L_{2n}} & \frac{pL_{12}}{L_{2n}} & -pL_2 & -\frac{pR_2}{L_{2n}} \\ 0 & 0 & 0 & 0 & 0 & 0 & 0 \end{bmatrix};$$

$$B_2^T = \begin{bmatrix} 0 & 0 & \frac{1}{T_{fc}} \end{bmatrix}; \quad D_{12}^T = [1 \ 0 \ 0 \ 0 \ 0 \ 0 \ 0];$$

$$D_{21} = [0 \ 0 \ 0 \ 0 \ 0 \ 0 \ 0]; \quad D_{22} = [0];$$

where $z = (z_1, z_2, \dots, z_7)^T$, $w = (w_1, w_2, \dots, w_7)^T$ are, respectively, the input and output uncertainty vectors interconnected by the matrix expression $w(p)=\Delta(p)z(p)$, in which the uncertainty matrix $\Delta(p)$ has a diagonal form.

The system of Eq. (2) is used to numerically determine the transfer function of the H_∞ -suboptimal controller using the mixed sensitivity method [9]. This transfer fractional-rational function for the nominal object has the form (3):

$$K(p) = k \frac{p^2 + b_1p + b_2}{a_0p^3 + a_1p^2 + a_2p + a_3}, \quad (3)$$

where k , b_1 , b_2 , a_0 , a_1 , a_2 , a_3 are the some coefficients, the values of which are determined during the numerical solution of the problem.

The transfer function (3) vanishes at the point $p = \infty$. Therefore, it can be expanded by the Euclidean method into a continued fraction. Then, after multiplying the numerator and denominator of this fraction by a scale

factor μ , it can be represented in the vicinity of the point $p = \infty$ by a ladder RC function (4):

$$\frac{k_\mu}{c_1 p + \frac{1}{r_1 + \frac{1}{c_2 p + \frac{1}{r_2 + \frac{1}{c_3 p + \frac{1}{r_3}}}}}}, \quad (4)$$

where $k_\mu = k\mu$.

As is known, the coefficients of this function correspond to the calculated values of the resistances (r_i values) of resistors and capacities (c_i values) of capacitors.

The relationship between the coefficients of the transfer function (3) and the ladder RC function (4) is determined in the process of folding the fraction (4) into a fractional rational expression and equating the coefficients of this expression with the corresponding coefficients of expression (3). As a result of such transformations, the following relations between them were found (5):

$$\begin{aligned} b_1 &= \frac{1}{c_2} \left(\frac{1}{r_2} + \frac{1}{r_1} \right) + \frac{1}{c_3} \left(\frac{1}{r_3} + \frac{1}{r_2} \right); \\ b_2 &= \frac{1}{c_2 c_3} \left(\frac{1}{r_2 r_3} + \frac{1}{r_1 r_3} + \frac{1}{r_1 r_2} \right); \quad a_0 = \frac{c_1}{\mu}; \\ a_1 &= \frac{1}{\mu} \left(\frac{1}{r_1} + c_1 b_1 \right); \\ a_2 &= \frac{1}{\mu} \left\{ \frac{1}{r_1} \left[\frac{1}{c_2 r_2} + \frac{1}{c_3} \left(\frac{1}{r_3} + \frac{1}{r_2} \right) \right] + c_1 b_2 \right\}; \\ a_3 &= \frac{1}{\mu c_2 c_3 r_1 r_2 r_3}; \quad \mu = c_1 n. \end{aligned} \quad (5)$$

To make relationship between the coefficients of the ladder circuit (4) with the resistances and capacitances of the electrical circuit of the robust controller, expressions (6) are used:

$$\begin{aligned} c_1 &= C1; \quad r_1 = R1; \quad c_2 = C2; \\ r_2 &= R2; \quad c_3 = C3; \quad r_3 = R3; \end{aligned} \quad (6)$$

where $R1, R2, R3$ are resistances of resistors; $C1, C2, C3$ are capacitances of capacitors.

If among the coefficients (6) of the ladder RC function there are negative capacitance c_i with index i and negative resistance r_k with index k , then they are replaced by expressions of the form:

$$c_i = -C_i \frac{R4}{R5}; \quad r_k = -R_k \frac{R6}{R7}. \quad (7)$$

Moreover, the indices in the right-hand sides of Eq. (7) denote the numbers of capacitors and resistances of the circuit according to Fig. 1; $R4=R5$ and $R6=R7$; the fractions in Eq. (7) are irreducible, because the resistances of the circuit are selected with tolerances.

The written Eq. (7) with negative parameters of capacitance and resistance correspond to active circuits based on operational amplifiers studied in [10].

The relationship of the numerator k_μ of the ladder RC function (4) with the resistances $R8$ and $R9$ of the operational amplifier of the circuit is described by the equation (8):

$$k_\mu = \frac{R9}{R8}. \quad (8)$$

Relations (6) – (8) make it possible to construct a basic electrical circuit of the controller. This circuit for $i = k = 2$ is shown in Fig. 1. It contains negatrons of negative capacitance NC and negative resistance NR, designed to suppress interference, and differs from circuit [1] only in other designations of resistance and capacitance indexes.

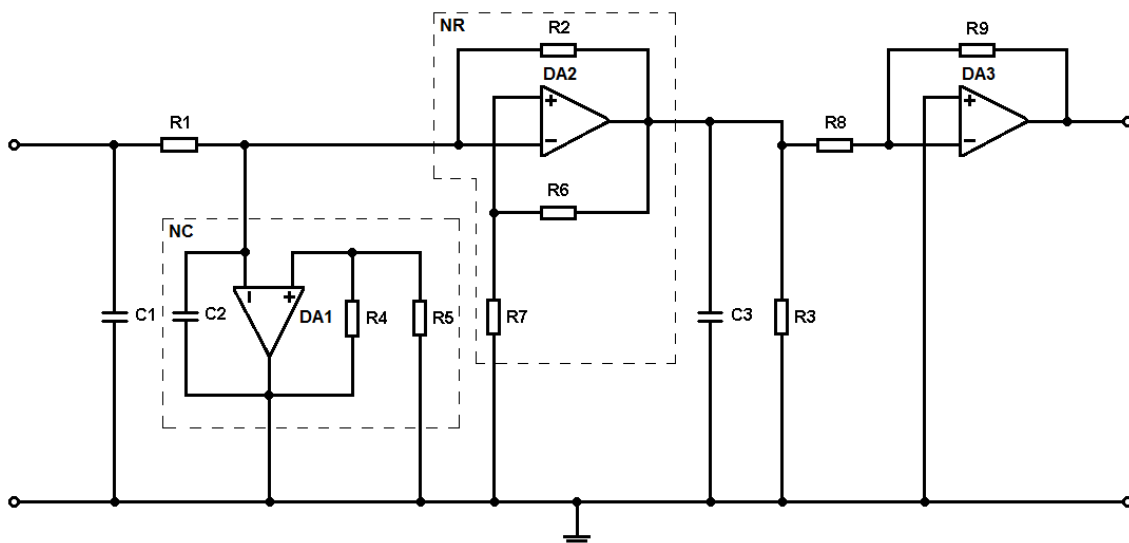


Fig. 1 Electrical circuit of a robust controller

The choice of the resistances of the resistors and capacitances of the capacitors of the electrical circuit is carried out in the process of rounding the calculated

values of the RC function coefficients (4) to the values of the standard series, and their permissible deviations are determined from the calculation of the stability of the

robust rotor flux-linkage control system with random variations in the object parameters (1) and controller (4) within the specified boundaries. In this case, the resistances $R4...R7$ of the circuit resistors are selected from design considerations, and their accuracy from the same stability calculation.

The procedure for calculating and selecting the parameters of resistors and capacitors of the electrical circuit of a stabilizing robust rotor flux-linkage controller consists of the following sequence of actions:

1. The transfer function (3) of the controller of the nominal object is calculated.

2. The decomposition of the found transfer function into a continued fraction is performed and the ladder RC function (4) is compiled.

3. The coefficients of the ladder RC function (4) are rounded to the values of standard series [5].

4. The transfer function of the controller (3) is formed programmatically according to Eq. (5) – (8).

5. The boundaries of the change in the nominal parameters of the object, the resistances of the resistors and capacitances of the capacitors of the electric circuit of the controller are set, taking into account the rounding error of their calculated values to the values of the standard series [5], as well as the accuracy of manufacture and cost.

6. A software system for the stabilization of the rotor flux-linkage consisting of the series-connected transfer functions of the controller (3) and the object (1), covered by a single feedback is made.

7. Curves of flux-linkage transient processes for a closed system and a Bode diagram for an open control system are calculated with random variations in the parameters of the object and the controller within the given boundaries.

8. The accuracy of stabilization of the flux-linkage is determined by the ranges of the curves of steady-state transient processes of the rotor flux-linkage, and by the Bode diagram the stability margins in amplitude and phase were determined.

9. The calculation according to items 5 – 8 is repeated until a compromise in the choice of the controller's electrical circuit element's tolerances and their cost is achieved.

The calculations were performed at the following nominal values of the initial data of the object (1): $T_{fc} = 0,001$ s; $R_{1n} = 2,65$ Ω ; $R_{2n} = 2$ Ω ; $L_{1n} = 0,186$ H; $L_{2n} = 0,189$ H; $L_{12n} = 0,179$ H; $\sigma = 0,0996$, corresponding to an asynchronous electric drive with a MDXMA100-32 motor.

Calculated from these data, the nominal values of the parameters of the robust controller (3) turned out to be equal: $k = 5,016 \cdot 10^5$; $b_1 = 148,963$; $b_2 = 1,0612 \cdot 10^4$; $a_0 = 1$; $a_1 = 1,451 \cdot 10^4$; $a_2 = 1,262 \cdot 10^7$; $a_3 = 3,532 \cdot 10^7$. The calculated values of the resistances and capacitances of the ladder RC function (4) at $\mu = 10^{-5}$ corresponding to these parameters were: $c_1 = 10$ μ F; $r_1 = 6,963$ Ω ; $c_2 = -197$ μ F; $r_2 = -5,709$ Ω ; $c_3 = 12,56$ mF; $r_3 = 28,79$ Ω . These values were rounded to the values of standard

series [5]. These series, rounded values of quantities to the values of series, rounding errors and recommended tolerances of the series are shown in Table 1.

Table 1
Selection of resistances and capacitances of the circuit

Designation	A row according to [5]	Value	Rounding error, %	Recommended row tolerance, %	
R1	Ω	E96	6,98	-0,24	2
R2		E96	5,69	0,33	2
R3		E24	30	-4,2	5
R4		E24	100	0	5
R5		E24	100	0	5
R6		E96	100	0	2
R7		E96	100	0	2
R8		E24	100	0	5
R9		E24	510	-1,7	5
C1	μ F	E24	10	0	5
C2		E24	200	-1,5	5
C3	mF	E24	13	-3,5	5

The undefined parameters $K_{fc}/K_{fc n}$, R_{1eq} , R_2 , L_1 , L_2 and L_{12} of the object (1) varied within the range of ± 90 %, the resistances $R1$, $R2$, $R6$, $R7$ – in the range of ± 3 %; $R3$, $R4$, $R5$, $R8$, $R9$ and capacitance $C1$, $C2$, $C3$ – in the range of ± 10 %. These errors of elements overlap the values of row tolerances recommended by [5] and other guiding documents approximately twice.

Fig. 2 shows 20 curves of the rotor flux-linkage transient processes corresponding to random variations of the undefined parameters of the object and the controller selected by the Monte Carlo method within the given boundaries. They are obtained in the MATLAB application packages with a single abrupt change in the reference action.

As seen, the curves of transient processes shown in Fig. 2 do not go beyond the boundaries of 3 % tube.

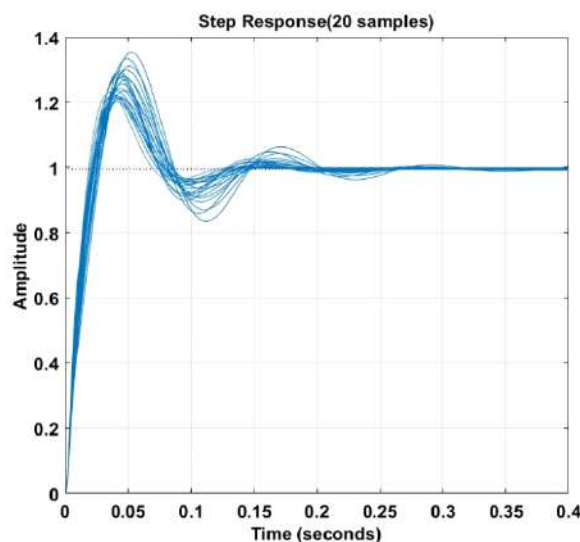


Fig. 2. Rotor flux-linkage transient processes

Fig. 3 shows a Bode diagram with 20 generated amplitude $L(\omega)$ curves and 20 phase $\varphi(\omega)$ frequency response curves with the same undefined parameters as in the previous case. From the amplitude $L(\omega)$ and phase

$\varphi(\omega)$ characteristics presented in this diagram, it can be seen that the system is stable, since the amplitude characteristic crosses the abscissa axis earlier than the phase characteristic, finally falling off, going beyond the angle value of -180 degrees. In this case, the calculated values of the stability margin in amplitude is 19.2 dB, and in phase is 50.6 degrees for the nominal values of the parameters of the object and the controller with scatter of random curves not exceeding 4 dB for amplitude and 15 degrees for phase frequency characteristics.

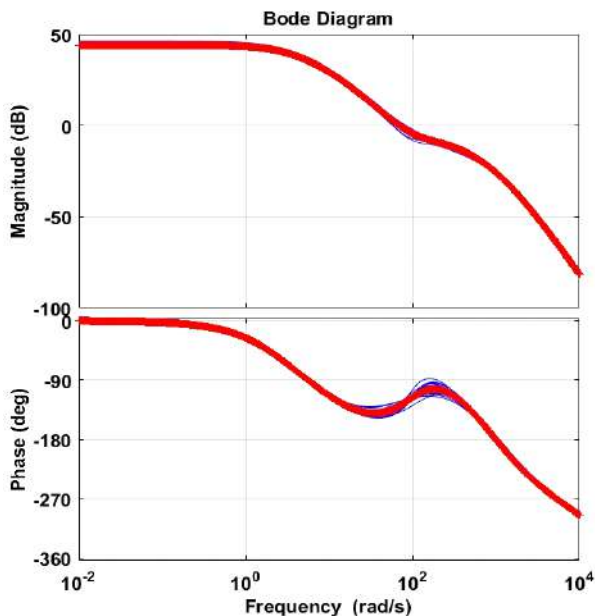


Fig. 3. Open-loop Bode diagram

Checking the operation of the circuit, which is shown in Fig. 1, was carried out in the Multisim package. Its modeling was carried out with random variations in the resistances of resistors and capacitances of capacitors of the specified accuracy. A constant voltage of 1 V and a harmonic signal with a frequency of 20, 50, 5000 Hz and an amplitude of 0.5 V were applied to the input of the circuit, which approximated the limit values of interference during the operation of the controller in the flux-linkage control system (for example, sensor noise, contacts in connectors, electromagnetic fields, interference with the frequency of the supply network, etc.). The voltage filtered by the controller was recorded at the output of the circuit. Recording of these voltages was carried out continuously with a multimeter (Fig. 4).

As expected, the electrical circuit of the H_∞ -suboptimal robust controller provides high-precision noise suppression. In this case, both with accurate and with rounded values of resistances and capacitances, the same voltage value of 11.8 V is set at the output, regardless of the frequency of the interference at the input. This voltage is approximately an order of magnitude less than the steady-state value calculated by Eq. (3) at $p = 0$, because at the output from the circuit it is always determined with an accuracy to a constant factor.

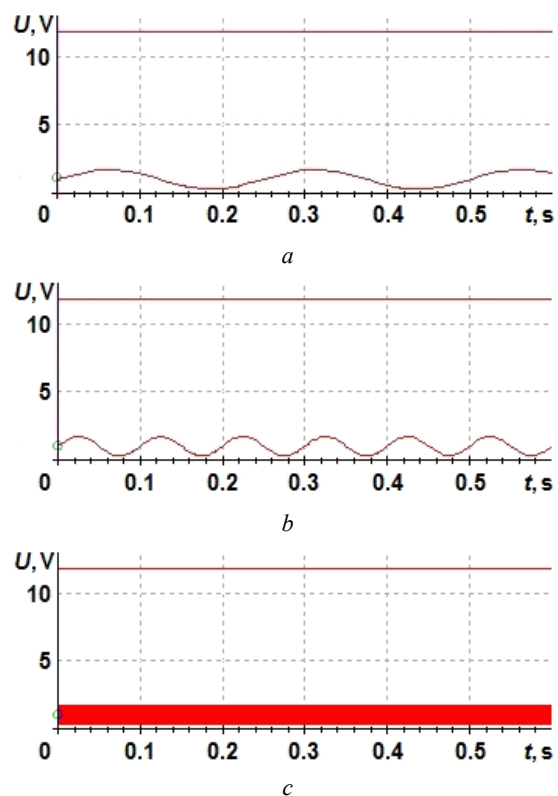


Fig. 4. Dependence of voltage U at the input (sinusoidal line) and output (straight line) on time t :
 a – 20 Hz; b – 50 Hz; c – 5000 Hz

Conclusions.

1. For the first time, analytical dependences of the ladder RC function coefficients on the resistances of the resistors and capacitances of the capacitors of the H_∞ -suboptimal robust controller's circuit diagram were obtained, which allow, together with the control object within the ranges of the specified boundaries of the change in the undefined parameters of the object, the resistances and capacitances of the controller, to carry out calculations and analysis of stability of the stabilizing flux-linkage system and the selection on this basis of resistors and capacitors of the circuit from the series of preferred values, taking into account the margin of tolerances.

2. Based on the calculation and analysis of the stability of the robust flux-linkage control system and the obtained analytical expressions describing the relationship between the coefficients of the transfer function of the robust controller and the resistances of the resistors and capacitances of the capacitors of the electrical circuit of the controller, the limiting values of the tolerances for the selection of resistors and capacitors of the circuit from the preferred series, identified by a specific example.

3. The analysis of the filtering of sinusoidal signals of various frequencies by the electric circuit of the regulator in the Multisim package carried out using the same example, taking into account the selected limit values of the tolerances of resistors and capacitors, shows its insensitivity to these signals.

REFERENCES

1. Khlopenko N.Y., Rozhkov S.O., Khlopenko I.M. *Sistema vektornogo keruvannya shvidkisty asinhronnogo elektrodviguna* [Asynchronous motor vector speed control system]. Patent UA, no. 137157, 2019. (Ukr).
2. Polilov E.V., Rudnev E.S., Skorik S.P. Synthesis of robust control algorithms for a synchronous electric motor means H_∞ -theory. *Transactions of Kremenchuk Mykhaylo Ostrogradskiy State University*, 2010, iss. 4/2010 (63), part 3, pp. 15-20. (Ukr).
3. Rudnev E.S., Morozov D.I. μ -synthesis of robust speed controller of synchronous electric drives. *Electrotechnic and Computer Systems*, 2015, vol. 20, no. 96, pp. 42-50. (Rus). doi: **10.15276/eltecs.20.96.2015.06**.
4. Khlopenko I.N., Rozhkov S.A., Khlopenko N.J. Stability and accuracy of the robust system for stabilizing the rotor flux-linkage of an asynchronous electric drive at random variations of the uncertain parameters within the specified boundaries. *Electrical engineering & electromechanics*, 2018, no. 4, pp. 35-39. doi: **10.20998/2074-272X.2018.4.06**.
5. *GOST 28884-90. Riady predpochtitel'nykh znachenii dlia rezistorov i kondensatorov* [GOST 28884-90. Preferred number series for resistors and capacitors]. Moscow, Standartinform Publ., 2006. (Rus).
6. Kuznetsov B.I., Nikitina T.B., Kolomiets V.V., Bovdui I.V. Improving of electromechanical servo systems accuracy. *Electrical engineering & electromechanics*, 2018, no. 6, pp. 33-37. doi: **10.20998/2074-272X.2018.6.04**.
7. Kuznetsov B.I., Nikitina T.B., Bovdui I.V., Kobilyanskiy B.B. Improving of electromechanical stabilization systems accuracy. *Electrical engineering & electromechanics*, 2019, no. 2, pp. 21-27. doi: **10.20998/2074-272X.2019.2.04**.
8. Khlopenko N., Rozhkov S., Khlopenko I. Filtration Of Undesired Signals By The Robust Controller In The Rotor Flux-Linkage Control System. *Scientific Bulletin Kherson State Maritime Academy*, 2019, vol. 1, no. 20, pp. 122-131. (Rus). doi: **10.33815/2313-4763.2019.1.20.122-131**.
9. Richard Y., Chiang R., Michael G., Safonov M. *MATLAB: Robust Control Toolbox. User's Guide. Version 2*, 1998. 230 p. Available at: <http://www.mathworks.com> (Accessed 12 May 2016).
10. Petrenko I.A. Study of circuit negatrons properties, implemented on operational amplifiers. *Technology audit and production reserves*, 2016, vol. 2, no. 1 (28), pp. 40-50. doi: **10.15587/2312-8372.2016.66910**.

Received 08.09.2020

Accepted 17.10.2020

Published 24.12.2020

I.N. Khlopenko¹, Graduate Student,
 N.J. Khlopenko¹, Doctor of Technical Science, Professor,
 S.A. Rozhkov¹, Doctor of Technical Science, Professor,
¹ Kherson State Maritime Academy,
 20, Ushakova Ave., Kherson, 73000, Ukraine.
 e-mail: khlopenko.ivan@gmail.com,
 khlopenko.n@gmail.com,
 rozhkov_ser@meta.ua

How to cite this article:

Khlopenko I.N., Khlopenko N.J., Rozhkov S.A. Analysis and verification of the operation of the stabilizing robust controller's electrical circuit of the rotor flux-linkage control system. *Electrical engineering & electromechanics*, 2020, no. 6, pp. 18-23. doi: **10.20998/2074-272X.2020.6.03**.

V.A. Lebedev, G.V. Zhuk, N.J. Ostroverkhov, A.M. Khalimovskyy

CONTROL OF VALVE ELECTRIC DRIVE COORDINATES OF AUTOMATED WELDING EQUIPMENT FEED MECHANISMS

Goal. Finding ways to improve the quality of operation of the electrode wire feeder in terms of increasing the frequency of undistorted pulse feed with controlled characteristics, in particular its speed, as well as developing methods to simplify the adjustment of regulators of fast-acting electric drive to improve the results of the arc welding and surfacing process. Methodology. In the work, methods of analysis of existing technical solutions were used to increase the speed of operation of electric drives for a specific purpose with the choice of the most rational solution based on the use of the method of synthesis of a control system based on the concept of inverse problems of dynamics with subsequent computer simulation, confirming the adequacy of the applied method of synthesis of high-speed systems. Results. The authors considered the possibilities of increasing the speed of control systems for gearless computerized electric drives in a system with modern designs of valve electric drives for electrode wire feeding systems. A mathematical model of a rectifier motor has been developed with some assumptions that significantly influenced the simulation results. The new possibilities are based on the use of an original synthesis method based on the use of the concept of the inverse problem of dynamics with the subsequent study of the operation of the automatic control system for pulse wire feed, which was performed with aperiodic adjustment of the velocity contour by different methods. This approach made it possible to obtain the necessary laws of electric drive control without the traditional solution of the optimization problem. The developed control system for the electrode wire feed with pulsed motion algorithms provided the required linear movement of the wire at a pulse repetition rate of 100 Hz. The carried out computer simulation of the new control system confirmed the results of the study. It was found that an increase in the pulse time duration over 50 % of the pulse repetition period for given feed frequencies leads to an increase in the wire movement in the pulse, as well as to a decrease in the worked out frequency of the wire linear displacement feed. It was not possible to provide the required wire movement in the impulse feed mode for aperiodic adjustment of the speed loop with a P-controller for the same system parameters. Originality. The development was carried out for a specific application in the electrode wire feed systems of mechanized and automatic equipment for consumable electrode arc welding with obtaining certain algorithms of pulse motion. To effectively solve the complex problem of increasing the frequency of feed pulses with the provision of a displacement step, an original technique of the concept of inverse dynamic problems with confirmation of the result by mathematical modeling by practical results was used. Practical significance. The use of standard settings of the valve electric drive of mechanized and automatic welding equipment provides the frequency of undistorted electrode wire feed in the pulse mode of the feed mechanisms up to 50 Hz. New possibilities of settings made it possible to increase the frequency of wire feed, which makes it possible to raise the quality indicators of welded products - the formation of a welded joint, a decrease in electrode metal losses, an increase in the mechanical properties of a welded joint. References 16, figures 6.

Key words: valve electric drive, automatic control system, adjustment of regulators, pulse wire feed mechanism, welding equipment.

Дослідження показали, що використання стандартного налаштування контуру швидкості на симетричний оптимум системи керування механізмом подачі автоматизованого зварювального обладнання забезпечує частоту імпульсної подачі електродного дроту до 60 Гц та покращення якості зварних з'єднань. На основі концепції зворотних задач динаміки в поєднанні з мінімізацією функціоналу миттєвого значення кінетичної енергії синтезовано регулятор швидкості, що дозволило підвищити частоту імпульсів до 100 Гц при відпрацюванні необхідного лінійного переміщення дроту. Це істотно розширює можливості зварювання і наплавлення. Система керування механізмом подачі дроту реалізована на основі безредукторного вентильного електропривода. Бібл. 16, рис. 6.

Ключові слова: вентильний електропривод, система автоматичного керування, налаштування регуляторів, механізм імпульсної подачі дроту, зварювальне обладнання.

Исследования показали, что использование стандартной настройки контура скорости на симметричный оптимум системы управления механизмом подачи автоматизированного сварочного оборудования обеспечивает частоту импульсной подачи электродной проволоки до 60 Гц и улучшение качества сварных соединений. На основе концепции обратных задач динамики в соединении с минимизацией функционала мгновенного значения кинетической энергии синтезирован регулятор скорости, что позволило повысить частоту импульсов до 100 Гц при отработке требуемого линейного перемещения проволоки. Это существенно расширяет возможности электродуговой сварки и наплавки. Система управления механизмом подачи проволоки реализована на основе безредукторного вентиального электропривода. Библ. 16, рис. 6.

Ключевые слова: вентильный электропривод, система автоматического управления, настройка регуляторов, механизм импульсной подачи проволоки, сварочное оборудование.

Introduction. Mechanized and automatic electric arc welding and surfacing using electrode wire is constantly being improved on the basis of technical and technological innovations [1, 2]. One of the ways to improve the quality indicators of welding and surfacing is the use of pulse methods of influence on the arc process, which are carried out both by means of a welding current

source [3, 4] and pulse feed of an electrode wire [5, 6]. The relevance of the search for technical solutions that provide an increase in the frequency of wire feed pulses above 60 Hz for the required range of linear displacement per pulse is due to the task of improving the quality of welding and surfacing [7]. One of the main directions of

© V.A. Lebedev, G.V. Zhuk, N.J. Ostroverkhov, A.M. Khalimovskyy

improving the technology of welding and surfacing with a pulse feed of an electrode wire is the use of high-speed gearless computerized electric drives based on valve electric motors. In this work, on the basis of the concept of inverse problems of dynamics (CIPD) in conjunction with minimization of local functionals of instantaneous values of energies, a synthesis of a control system for a pulsed electrode wire with a valve electric drive (VED) is performed. On the basis of computer simulation of the dynamic processes of the system using MATLAB/Simulink, satisfactory results were obtained, in particular, the speed of operation, which is so necessary for obtaining pulses of electrode wire movement to control the transfer of electrode metal droplets in a controlled mode into the weld pool. A comparative analysis of the results of operation with the control system based on the standard setting of controllers is carried out.

Features of control of wire feeders based on VED.

Perspective direction is due to the control of the transfer of electrode metal and associated with it the following main advantages of the process [8]:

- the possibility of a significant improvement in the structure of the weld metal and deposited layer;
- implementation of the task of controlling the shape of the welded joint, the value of reinforcement and penetration;

- reduction of energy and resource consumption.

The implementation of the controlled pulse feed process can be carried out in several ways using different systems. Recently, the most rational technical solution for obtaining a controlled pulse feed is the use of feed mechanisms based on specially developed valve electric motors with a conventional gearless roller propulsion mechanism and a computerized control system [9].

Investigation of the characteristics of the welding process using a valve electric drive with standard settings of the controllers made it possible to determine that the frequency of the pulse feed with a certain step of moving the electrode wire significantly affects the results of surfacing welding in almost all parameters. For an example, partially described in [10], Fig. 1 shows microsections of cross-sections of rollers made on alloy steels at different frequencies of the electrode wire feed.

The analysis of microsections shows that with a pulse feed, the growth of crystals sharply decreases, their disorientation increases, which leads to an increase in the strength and wear resistance of the product being deposited or welded [11].

From the results of the cycle of conducted studies, it is obvious that the wire feed mechanism should have a wide range of wire feed frequencies.

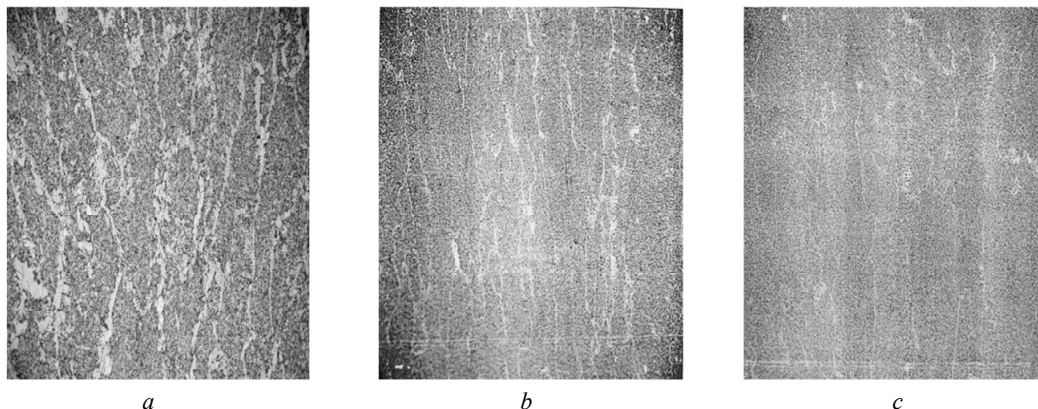


Fig. 1. Microstructures of deposited rollers (X200) at pulse feed frequencies: *a* – 0; *b* – 28 Hz; *c* – 45 Hz

The goal of the work is improving the quality of the wire feed mechanism to improve the characteristics of the arc process by developing a method for adjusting the controller to increase the speed of the speed loop of the electric feed drive.

Application of standard settings of VED of mechanized and automatic welding equipment provides the frequency of undistorted electrode wire feed in a pulse mode of operation up to 60 Hz. An increase in the frequency of wire feeding makes it possible to increase the quality indicators of welded products – the formation of a welded joint, a decrease in electrode metal losses, an increase in the mechanical properties of a welded joint.

Mathematical model of the VED control system.

In the study of the automatic control system (ACS) of feeding the electrode wire, the valve electric motor is described by the mathematical model of a DC machine with independent excitation [15, 16]. A standard ACS has a dual-loop structure of a slave control system, consisting

of an internal current control loop with a relay PPT controller and an external speed control loop with a P-controller, shown in Fig. 2. Dynamic processes in ACS are described by the following system of equations:

$$\begin{cases} M - M_{st} = J \cdot p \cdot \omega; \\ I = \frac{(U - E)}{R_f \cdot (T_f \cdot p + 1)}; \\ U = \frac{(I^* - K_1 \cdot I) \cdot K_{dr}}{R_f \cdot (T_\mu \cdot p + 1)}; \\ E = cF \cdot \omega; \\ M = cF \cdot I; \\ I^* = (\omega^* - K_2 \cdot \omega) \cdot K_g, \end{cases}$$

where ω^* , ω are the speed setting and motor rotation speed; I^* , I are the current loop setting and motor current; M is the electromagnetic torque of the electric motor; M_{st} is the moment of resistance on the motor shaft;

U is the output voltage of the power converter; E is the EMF of the electric motor; K_g is the gain of the speed P-controller; K_{dr} is the transmission coefficient of the power converter; T_μ is the time constant of the converter; K_1 , K_2 are the current and speed feedback coefficients;

R_f is the linear active resistance of the electric motor in a heated state; T_f is the time constant of the motor phase; cF is the coefficient of excitation of the electric motor; J is the total moment of inertia, reduced to the motor shaft; p is the Laplace operator.

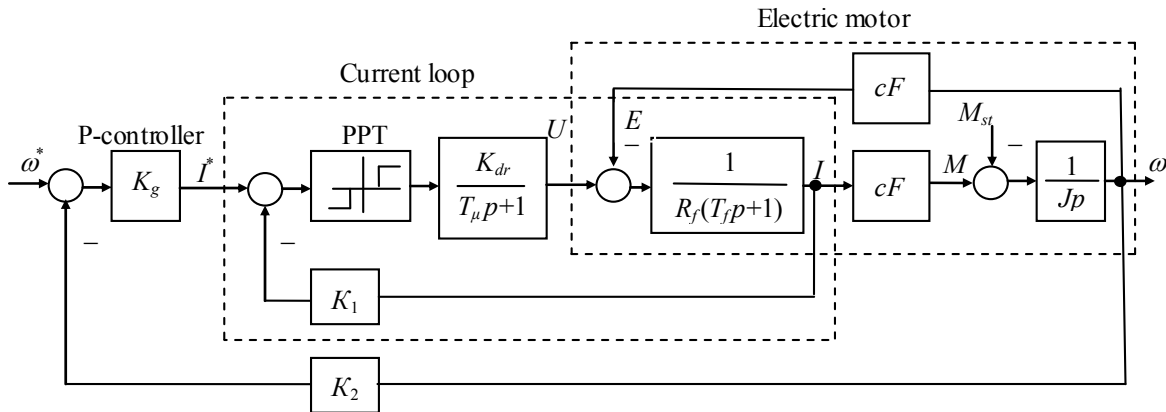


Fig. 2. Block diagram of the automatic speed control system of the valve electric drive of wire feed

Synthesis of the law of VED speed control by the method of inverse problems of dynamics. Analysis of synthesis methods for closed-loop control systems has shown that the use of a non-standard control algorithm synthesized on the CIPD in combination with minimization of local functionals of instantaneous energy values makes it possible to improve the quality of control and the frequency of wire feed. Control laws based on CIPD also provide weak sensitivity to parametric and coordinate disturbances, carry out a dynamic decomposition of an interconnected system and are simple to implement, since they do not contain differentiation operations [12-14]. The advantage of the synthesis method is the definition of control laws without the traditional solution of the optimization problem. The control laws are determined by the type of the differential equation of the object and the type of the differential equation, with the help of which the desired quality of the transient of the closed control loop is set.

According to Fig. 2, the speed loop consists of an optimized internal current loop and an integrating element representing the electromechanical part of the drive. The input of the loop receives the signal of the speed reference ω^* . When developing the control law of the speed controller, the inertia of the optimized current loop in the form of a first-order aperiodic link model with a small time constant T_1 is not taken into account. However, after the synthesis is completed, an analysis is made of its influence on the control quality indicators. After such assumptions, the control object of the speed controller is described by the following first-order differential equation

$$\dot{\omega} = \frac{cF}{J} I^* \quad (1)$$

For a first-order object (1), the order of the equation of the desired quality of speed control is also taken to be equal to one

$$\dot{z} + \alpha_0 z = \alpha_0 \omega^* \quad (2)$$

with the provision of first-order astatism and a given quality factor in speed equal to

$$D_{\omega}^* = \alpha_0 \quad (3)$$

The required duration t_{mn} of the aperiodic transient of the speed is given using a single coefficient of equation (2)

$$t_{mn} \approx 3 / \alpha_0$$

It is necessary to find the control function of the speed controller I^* so that the quality of speed control ω approaches the desired one, given by equation (2). The degree of approximation of the real process to the desired one is estimated by the functional, which characterizes the energy of the first derivative of the kinetic energy normalized to the moment of inertia

$$G(I^*) = \frac{1}{2} [\dot{z}(t) - \dot{\omega}(t, I^*)]^2 \quad (4)$$

The functional is minimized according to the first-order gradient law

$$\frac{dI^*(t)}{dt} = -\lambda_{\omega} \cdot \frac{dG(I^*)}{dI^*}, \quad (5)$$

where $\lambda_{\omega} > 0$ is the constant.

The derivative of the functional taking into account (1) and (2) is equal to

$$\frac{dG(I^*)}{dI^*} = \frac{cF}{J} \cdot (z - \dot{\omega}) \quad (6)$$

After substituting (6) into (5), the speed control law is found

$$\dot{I}^*(t) = k_{\omega} (z - \dot{\omega}), \quad (7)$$

where $k_{\omega} = cF \cdot \lambda_{\omega} / J$ is the speed controller gain.

The variable z in (7) plays the role of the required acceleration, which is determined in real time from the equation of the desired quality (2) by closing the speed feedback $z = \omega$

$$z = \alpha_0 \cdot (\omega^* - \omega) \quad (8)$$

The speed control law takes its final form after integrating both sides of equation (7) taking into account (8)

$$I^*(t) = k_{\omega} \cdot (z - \omega); \quad (9)$$

$$z = \alpha_0 \int (\omega^* - \omega) dt$$

The block diagram of the speed controller built on the basis of (9) is shown in Fig. 3.

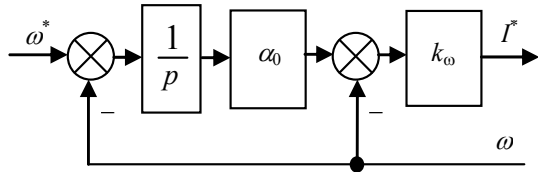


Fig. 3. Block diagram of the speed controller

The speed controller contains only the parameter α_0 of the desired control law and does not contain the parameters of the control object, which is typical for classical control laws.

Closed loop speed equation

$$\ddot{\omega} + \frac{cF}{J} \cdot k_{\omega} \cdot \dot{\omega} + \frac{cF}{J} \cdot k_{\omega} \cdot \alpha_0 \cdot \omega = \frac{cF}{J} \cdot k_{\omega} \cdot \alpha_0 \cdot \omega^*, (10)$$

obtained after substituting control law (9) into the object equation (1), shows that closed-loop system (10) is stable even with an unlimited increase in the gain of the speed controller $k_{\omega} \rightarrow \infty$. According to the Hurwitz stability criterion, the coefficients of equation (10) are positive

$$\frac{cF}{J} \cdot k_{\omega} > 0; \quad \frac{cF}{J} \cdot k_{\omega} \cdot \alpha_0 > 0.$$

An important task is to determine the properties of the speed loop at finite values of the controller gain. According to the transfer function of the speed open loop obtained on the basis of (10)

$$W(p) = \frac{cF \cdot k_{\omega} \cdot \alpha_0 / J}{p \cdot (p + cF \cdot k_{\omega} / J)}, (11)$$

the speed loop has a given first-order astatism, as well as a speed quality factor equal to the given one (3)

$$D_{\omega} = D_{\omega}^* = \alpha_0. (12)$$

This ensures the degree of approximation of the real transient of the speed to the desired process specified by (2), with moderate gain of the speed controller k_{ω} .

The estimation of the influence of the unaccounted inertia of the current loop with a small time constant T_1 on the dynamic properties of the speed loop is carried out using the characteristic equation of the closed-loop system obtained similarly to (10)

$$T_1 \cdot T_0 \cdot p^3 + T_0 \cdot p^2 + k_{\omega} \cdot p + k_{\omega} \cdot \alpha_0 = 0, (13)$$

where $T_0 = J / cF$ is the time constant of the controlled object.

For the stability of the speed loop according to (13), the condition $\alpha_0 < (1 / T_1)$ must be satisfied. Thus, the inertia of the current loop limits the desired speed of the speed loop.

Investigation of the VED control system. The research was carried out by modeling in the MATLAB/Simulink software package. To assess the efficiency of the speed control system of the valve electric drive of the wire feeder, a comparative analysis of the simulation results of the proposed system with a controller (9) and an ACS with a speed P-controller was carried out. The value of the P-controller gain $K_g = 8.75$ was obtained when the speed loop was tuned to an aperiodic process. When simulating a two-circuit ACS, the following values of the parameters of the structural diagram were taken: $T_f = 0.5 \mu s$; $R_f = 0.9 \Omega$; $cF = 1 \text{ V}\cdot\text{s}$; $J = 0.001 \text{ kg}\cdot\text{m}^2$; $K_1 = 1.94$; $K_2 = 0.25$. The current loop of each of the systems under consideration contains a PPT with a dead zone of 0.5 V. The voltage at the output of the power converter is $U = 24 \text{ V}$.

The simulation results of the current loop with a sinusoidal reference signal with a frequency of 100 Hz for the adopted settings are shown in Fig. 4. Analysis of the simulation results of the current loop for the reference signal I^* shows the satisfactory dynamics of its development.

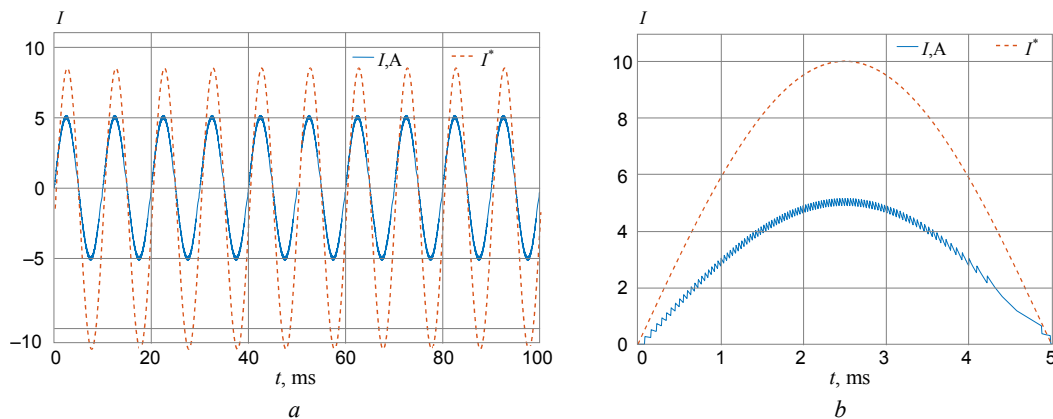


Fig. 4. Results of simulation of transients of the system current loop

The results of modeling the transients of both systems with a stepwise reference signal are shown in Fig. 5. Curves ω_1 correspond to a system with a controller (9), and ω_2 – to a system with a P-controller. Comparative analysis of the graphs of transients of the speed of systems (Fig. 5,a at $\alpha_0 = 500$; Fig. 5,b at $\alpha_0 = 1700$) confirms the dependence of the time of the transient on

the value of the parameter α_0 . Increasing this parameter at a constant value $k_{\omega} = 100$ shortens the transient time. Based on the simulation results, the maximum value of the parameter $\alpha_0 = 1700$ was determined for the aperiodic adjustment of the speed loop. With an increase in the value of this parameter, at a jump in the speed reference, overshoot appears in the system.

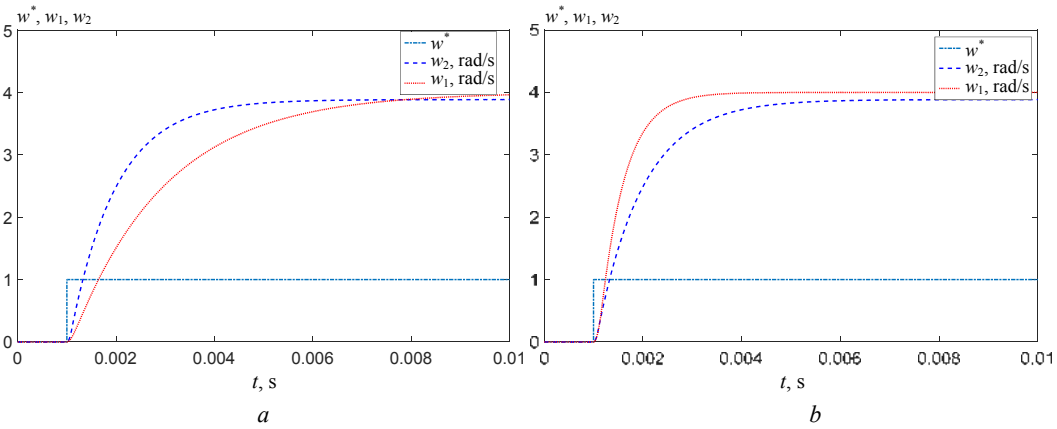


Fig. 5. Results of simulation of transients of systems with a jump in the reference signal

The results of modeling the transients of systems when generating a reference signal in the form of rectangular pulses with a duration of $t_{imp} = 5$ ms with a pulse repetition rate of 100 Hz are shown in Fig. 6. Formation of the speed reference signal ω^* in the form of rectangular pulses for the simulation conditions shown in Fig. 6,a, provides a movement L_1 of the wire (Fig. 6,b) by 3 mm with aperiodic adjustment of the loop using the CIPD. In the system with the P-controller of the speed loop, the movement L_2 of the wire (Fig. 6,b) was only 1.8 mm. The simulation results showed that with a load surge from 0 to 5 Nm for a 4 ms pulse and a pulse

repetition rate of 100 Hz, the wire displacement L_1 per pulse varied from 2.64 mm to 2.35 mm. The movement L_2 of the wire in the automatic control system with a speed P-controller for the same conditions of changing the load was less than 1.4 mm. When increase in the pulse time in the system with the speed P-controller up to 8 ms, the wire movement L_2 per pulse was changed from 2.2 mm to 2.8 mm with a decrease in the load in the range from 5 Nm to zero. Reducing the value of the moment of inertia J by 2 times allows with a load of 5 Nm and duration of pulse of 5 ms to ensure the wire movement L_1 by 2.4 mm.

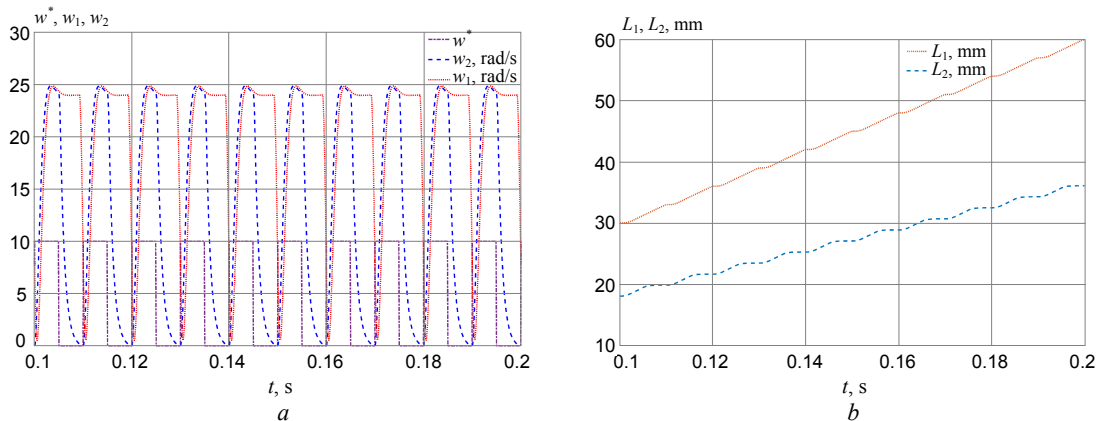


Fig. 6. Results of simulation of transients of systems with a reference signal in the form of rectangular pulses

Conclusions.

1. The results of the study of the system with the proposed speed controller shown that the electrode wire feed mechanism provides the required linear movement with a reference signal in the form of rectangular pulses at a repetition rate of 100 Hz. The recommended pulse width of the speed reference should not exceed 5 ms.

2. Studies of the system have also shown that at certain ratios of parameters, the speed P-controller can ensure the development of the required movements at a pulse repetition rate of 100 Hz, but with inferior quality indicators. Taking into account the possible range of variation of the system parameters, the final choice of the type of controller and the method of its adjustment should be determined by the technological requirements for the quality indicators of the ACS.

REFERENCES

1. Paton B.E. Modern directions of research and development in the field of welding and structural strength. *Automatic welding*, 2003, no. 10, 11 (607), pp. 7-13. (Rus).
2. Makovetskaya O.K. Main trends in the welding equipment market in 2008-2011 and forecast of its development (Review). *Automatic welding*, 2012, no. 6, pp. 44-50. (Rus).
3. Pal K., Pal S.K. Effect of Pulse Parameters on Weld Quality in Pulsed Gas Metal Arc Welding: A Review. *Journal of Materials Engineering and Performance*, 2010, vol. 20, no. 6, pp. 918-931. doi: 10.1007/s11665-010-9717-y.
4. Harris I. Transfer of heat and mass to the base metal in gas metal arc welding. *Welding, Brazing, and Soldering*, 2011, vol. 6, pp. 82-88.
5. Paton B.E., Lebedev V.A., Pichak V.H., Poloskov S.I., Shchavalev L.N. Analysis of technical and technological possibilities of the pulsed feed of electrode wire in arc welding and surfacing processes. *Welding International*, 2002, vol. 16, no. 7, pp. 575-581. doi: 10.1080/09507110209549580.

6. Krampit N.Y. Methods of controlling melting and transfer of electrode metal (review). *Welding International*, 2010, vol. 24, no. 10, pp. 808-812. doi: **10.1080/09507116.2010.486194**.
7. Paton B.E., Lebedev V.A., Zhuk G.V., Dragan S.V. Mechanical impulse and vibration effects in equipment and technologies of mechanized welding and surfacing. *16th International Science and Technology Conference «Vibrations in technology and technology»*. Collection of theses. Vinnytsia, Ukraine, 26-27 October 2017, pp. 10-16. (Rus).
8. Lebedev V., Reisgen U., Lendiel I. Study of technological opportunities of GMA welding and surfacing with pulse electrode wire feed. *Welding in the World*, 2016, vol. 60, no. 3, pp. 525-533. doi: **10.1007/s40194-016-0321-0**.
9. Lebedev V.A., Rymsha V.V., Radimov I.N. Modern valve electric drives in systems of mechanized welding equipment. *Electrical machine-building and electrical equipment*, 2009, no. 74, pp. 22-24. (Rus).
10. Lebedev V.A., Dragan S.V., Zhuk G.V., Novikov S.V., Simutenkov I.V. Application of pulsed impact in consumable electrode gas-shielded arc welding (Review). *The Paton Welding Journal*, 2019, no. 8, pp. 18-26. doi: **10.15407/tpwj2019.08.04**.
11. Gill J.S., Kalyan Reddy T. Effect of weld pool vibration on fatigue strength and tensile strength of stainless-steel butt-welded joints by GTAW process. *Proceedings of the World Congress on Engineering*, 2018, vol. II WCE 2018, July 4-6, 2018, London, U.K.
12. Kuznetsov B.I., Nikitina T.B., Bovdui I.V., Kobilyanskiy B.B. Improving of electromechanical stabilization systems accuracy. *Electrical engineering & electromechanics*, 2019, no. 2, pp. 21-27. doi: **10.20998/2074-272X.2019.2.04**.
13. Kuznetsov B.I., Nikitina T.B., Kolomiets V.V., Bovdui I.V. Improving of electromechanical servo systems accuracy. *Electrical engineering & electromechanics*, 2018, no. 6, pp. 33-37. doi: **10.20998/2074-272X.2018.6.04**.
14. Ostroverkhov M., Pyzhov V., Korol S. Control of the electric drive under conditions of parametric uncertainty and coordinates' interrelation. *2017 International Conference on Modern Electrical and Energy Systems (MEES)*, Kremenchuk, 2017, pp. 64-67. doi: **10.1109/MEES.2017.8248953**.
15. Terekhov V.M., Osipov O.I. *Sistemy upravleniia elektroprivodov. Uchebnik dlia studentov vysshikh uchebnykh zavedenii* [Control systems of electric drives. Textbook for students of higher educational institutions]. Moscow, Akademiia Publ., 2006. 304 p. (Rus).
16. Lebedev V.A., Guly M.V. The high-speed valve electric drive for the equipment of the mechanized arc welding. *Mechatronics, automation, control*, 2014, no. 6. pp. 47-51. (Rus).

Received 09.09.2020

Accepted 16.10.2020

Published 24.12.2020

V.A. Lebedev¹, Doctor of Technical Science, Professor,
G.V. Zhuk¹,

N.J. Ostroverkhov², Doctor of Technical Science, Professor,
A.M. Khalimovskyy², Candidate of Technical Science, Associate
Professor,

¹ SF «Experimental Design-Technological Office
of the E.O. Paton Electric Welding Institute
of the National Academy of Sciences of Ukraine»,
7, Bogenko Str., Kiev, 03150, Ukraine,

e-mail: valpaton@ukr.net, oktb-paton@i.ua

² National Technical University of Ukraine «Igor Sikorsky Kyiv
Polytechnic Institute»,

37, Prospect Peremohy, Kyiv-56, 03056, Ukraine,

e-mail: n.ostroverkhov@hotmail.com, o.khalimovskyy@ukr.net

How to cite this article:

Lebedev V.A., Zhuk G.V., Ostroverkhov N.J., Khalimovskyy A.M. Control of valve electric drive coordinates of automated welding equipment feed mechanisms. *Electrical engineering & electromechanics*, 2020, no. 6, pp. 24-29. doi: **10.20998/2074-272X.2020.6.04**.

O.O. Palchykov

BREAKDOWN VOLTAGE OF MICRON RANGE AIR INCLUSIONS IN CAPACITOR PAPER

Purpose. To substantiate the breakdown mechanism of capacitor paper on the basis of numerical-field models with segmented cross-sections of cylindrical volumes of air and water, and also use the proposed models to determine the breakdown strength of air in micron-sized gaps under normal conditions. *Methodology.* The model bases on a finite element solution to an electrostatic problem in a volume of capacitor paper consisting of cellulose and pores with air and water. First, the possible scenarios for the growth of breakdown in capacitor paper are analyzed and to the conclusion is made, that complete breakdown developed from a partial breakdown in the air cavity. A brand of capacitor paper is chosen in such a way that when its thickness changed, the breakdown strength of the electric field changed over a wide range. Then, for the paper with the lowest average electric field intensity the possibility of explaining the complete breakdown by the breakdown of air segments on the basis of the Paschen dependence is checked. Further points of the obtained dependence by constructing models of papers of the same brand and a different thickness under the assumption of the similarity of electrostatic fields are determined. As such a criterion, the constancy of the equivalent effective permittivity are taken. *Results.* The dependence of the breakdown strength of the air in the range of 1.36...5.54 μm under normal conditions is determined. The obtained relationship is between the Paschen and Taev curves. *Originality.* For the first time, the possibility of indirectly estimation the breakdown strength of an insulating material using an electrostatic field model is indicated. *Practical value.* The proposed method for the numerical calculation of the breakdown voltage of air inclusions in the presence of water inclusions in the thickness of solid insulation can be applied to other types of solid thin-layer insulation. References 11, tables 3, figures 5.

Key words: electrical breakdown, model of capacitor paper, micron gap, electrostatic field, finite element method.

Отримана в роботі залежність напруженості електричного поля повітря від довжини розрядного проміжку задовільно пояснює значення пробивних напруг зразків конденсаторного паперу при зміні їх марок і товщини. Побудована залежність пробивної напруженості повітря при нормальних умовах в діапазоні 1,36...5,54 мкм на підставі розрахунку електростатичних полів в моделях конденсаторного паперу з сегментними поперечними перетинами циліндричних об'ємів повітря і води. Проведено зіставлення отриманої залежності з відомими експериментальними даними. Отримані дані в діапазоні 2...5,54 мкм найбільш близькі експериментальним даним Пешо. Бібл. 11, табл. 3, рис. 5.

Ключові слова: електричний пробій, модель конденсаторного паперу, мікронний проміжок, електростатичне поле, метод скінченних елементів.

Полученная в работе зависимость напряженности электрического поля воздуха от длины разрядного промежутка удовлетворительно объясняет значения пробивных напряжений образцов конденсаторной бумаги при изменении их марок и толщины. Построена зависимость пробивной напряженности воздуха при нормальных условиях в диапазоне 1,36...5,54 мкм на основании расчета электростатических полей в моделях конденсаторной бумаги с сегментными поперечными сечениями цилиндрических объемов воздуха и воды. Проведено сопоставление полученной зависимости с известными экспериментальными данными. Полученные данные в диапазоне 2...5,54 мкм наиболее близки экспериментальным данным Пешо. Библ. 11, табл. 3, рис. 5.

Ключевые слова: электрический пробой, модель конденсаторной бумаги, микронный промежуток, электростатическое поле, метод конечных элементов.

Introduction. If the technological mode of impregnation is violated (insufficient pressure during impregnation), air inclusions remain in the thickness of the capacitor paper, in which discharges occur during operation under high voltage. Therefore, it becomes necessary to evaluate the breakdown voltage of air inclusions of capacitor paper.

In this paper, it is proposed to determine the breakdown voltage of the power frequency of air in the micron range based on indirect estimates of the calculated values made on the basis of numerical modelling of the electrostatic field in capacitor paper with air inclusions. Capacitor paper is a three-component dielectric made up of cellulose, air and water. The choice of such a dielectric is based on the assumption that a change in the breakdown voltage with a change in thickness is explained by the development of a complete dielectric breakdown from a partial one in the air region. When the test voltage is applied, the electric field is distributed irregularly according to the dielectric permittivity and the

arrangement of the components. For example, for the considered insulating material in water, the modulus of the electric field strength (EFS) is the smallest, and in air it is the largest. Then, the possibility of a breakdown is checked for a section with an almost uniform EFS vector both in absolute value and in direction. If the check is satisfied, then this area is replaced with a perfectly conductive one. And everything is repeated until the discharge spreads over the entire thickness of the dielectric.

Literature review. In 1889 Friedrich Paschen established that the breakdown voltage in gases depends on the product of the gas pressure and the distance between the electrodes. Further studies have shown deviations from this law of similarity of gas discharges. Reviews of experimental studies of air breakdown at normal atmospheric pressure and micron gaps are given in [1-3], and the latest data in [4]. As a result, it was found that at normal pressure the left branch of the Paschen

© O.O. Palchykov

dependence falls with a decrease in the product of pressure and the distance between the electrodes, and the dependence of the breakdown voltage on the material of the electrodes is also determined. However, the experimental data of various authors differ greatly and sometimes even contradict each other.

It was also found that for air the breakdown voltage does not depend on the frequency at $f = 0...50$ Hz in discharge gaps up to 600 cm. For water and solid dielectrics, an increase in dielectric strength is observed at voltage exposure time commensurate with the germination time of the discharge channel (for liquids – 0.01 μ s at a thickness of 10...100 μ m, for solid dielectrics – 0.1 μ s at a thickness of 1 mm) [5].

The influence of air cavities on the development of a discharge in a polymer, taking into account the distribution of the electrostatic field and mechanical stresses, was analyzed in [6]; however, the Paschen dependence is taken as the breakdown condition.

The goal of the work is the determination of the breakdown voltage of micron range air inclusions in capacitor paper on the basis of numerical-field models of the electric field with segmental cross-sections of cylindrical volumes of air and water in cellulose.

A mathematical model. The volume ratio of the components of the capacitor paper is determined based on the equations:

$$\begin{cases} V_p \rho_p (1 - y) = V_c \rho_c + V_a \rho_a; \\ V_w \rho_w = V_p \rho_p y; \\ V_p = V_c + V_a + V_w, \end{cases}$$

where V_p , V_c , V_a and V_w are the volumes of paper, cellulose, air and water, respectively; ρ_p , ρ_c , ρ_a and ρ_w are the densities of paper, cellulose, air and water, respectively; y is the relative mass content of water in insulating paper.

Then the radius of pores containing air and water, of the length l and the amount N in the cellulose volume is

$$r = [(V_a + V_w)/(\pi \cdot l \cdot N)]^{0.5}.$$

An example of the location of the volumes of air and water in a pore is shown in Fig. 1. The cross-sections of the cylindrical volumes of pore materials are divided by the central curved trapezoids into three regions. The bases of such trapeziums occupy 20 % of the length of the line of separation of air and water media. This was done in order to distinguish subregions with practically uniform EFS in the air and water regions.

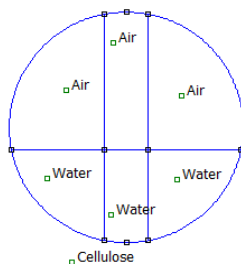


Fig. 1. Fragment of the calculation area

The calculation of the electric field in the cross-section with respect to the length l of the capacitor paper

with the width b and the thickness h is based on the following differential equations [7], compiled for each isotropic region with relative dielectric permittivity ε :

$$\begin{cases} \nabla^2 \varphi = 0; \\ \mathbf{E} = -\nabla \varphi; \\ \mathbf{D} = \varepsilon_0 \varepsilon \mathbf{E}, \end{cases}$$

where φ is the electrostatic scalar potential; \mathbf{E} is the EFS vector; \mathbf{D} is the electric induction vector; ε_0 is the electrical constant, $\varepsilon_0 = 8.854 \cdot 10^{-12}$ F/m.

At the interface between the two media, the condition of constancy of the electrostatic scalar potential and the condition of equality of the normal components of the vectors of the electric induction of these media are satisfied, which takes the following form for two dielectrics or a dielectric and a conductor, respectively [7]:

$$\varepsilon_1 \frac{\partial \varphi_1}{\partial \mathbf{n}_{12}} - \varepsilon_2 \frac{\partial \varphi_2}{\partial \mathbf{n}_{12}} = 0; \quad \varepsilon_1 \frac{\partial \varphi_1}{\partial \mathbf{n}_{12}} = \sigma,$$

where ε_1 and ε_2 are the relative dielectric permittivities of the first and second media, respectively; \mathbf{n}_{12} is the normal from the first to the second medium; σ is the surface charge at the interface between two media.

On the upper and lower planes perpendicular to the thickness of the considered volume, scalar electrostatic potentials are set equal in magnitude to half of the amplitude of the breakdown voltage of the capacitor paper indicated in [8], but with different signs. The solution area is limited by a cylindrical surface with radius of 200 μ m, length of 100 μ m and a zero potential on its surface.

To implement the connection between the value of the breakdown EFS of the material and its geometry, the area occupied by the material is divided into a number of subregions of a rectangular or curvilinear trapezoidal shape so that the vectors of the EFS of their individual elements are parallel to the direction vectors of the two sides of the subregions (hereinafter called lateral) with a given accuracy, and the values of the moduli of the EFS vectors changed insignificantly. Further, the EFS vector is averaged over the area of the subregion S :

$$\mathbf{E}_A = \frac{1}{S} \int_S \mathbf{E} dS.$$

Then the modulus of the resulting vector will be equal to its normal component defined for the base of the subregion. Consequently, with this approach, the modulus of the EFS vector determines the onset of breakdown in the discharge gap equal to the length of the side L of the subregion under consideration.

The basic assumptions of the model: dielectric materials do not possess conductivity; there are no charges at their interfaces; there are no space charges in dielectric materials, and their volumes do not change under the influence of an electrostatic field; ideal conductors with infinitesimal thickness are sources of an electrostatic field; the time of breakdown development in the volume of the samples under study is less than 1 μ s.

Numerical calculation of the electrostatic field by the finite element method is implemented in the FEMM computer code.

The theory of point defects can explain an increase in the breakdown voltage of paper with a decrease in thickness and an increase in density due to the fact that structural defects of the cellulose itself decrease [9]. An alternative explanation can be the well-known effect of increasing the breakdown voltage of thin samples of one-component insulating materials. In our case, the hypothesis is that with a decrease in the thickness of the capacitor paper, the areas occupied by cellulose also decrease, and their breakdown voltage will correspondingly increase. Consider samples of capacitor paper of various brands and the same thickness given in Table 1 [8]. If, in this case, the air volumes do not determine the breakdown voltage of the insulating material, then it turns out that the breakdown voltage should be higher for papers with a lower average density than for papers with a higher density, since their areas occupied by cellulose will be smaller. However, this is contrary to experience. Consequently, this hypothesis about the explanation of the change in the breakdown voltage of a series of capacitor paper of different thickness cannot be consistent. The influence of water volumes on the resulting breakdown voltage of the sample is insignificant, as shown by modelling. This is due to an insignificant voltage drop in the specified region, and upon its breakdown, the distribution of the electrostatic field in the paper will change negligibly little.

Table 1

Paper brand	Breakdown voltage amplitude U , V
MKOH 0,8-10	495
CKOH 1-10	594
KOH 2-10	537
KOH 3-10	594

In the reference literature for cellulose, the values of the breakdown EFS are in the range of 120...320 MV/m [10]. The dependence of the breakdown EFS of water on the length of the discharge gap is shown in Fig. 2. The points were obtained in [11] at a pulse voltage with amplitude of 800 V and front steepness of 0.5 μ s. It is proposed to approximate the law shown in Fig. 2 by the dependence

$$E_w = 6,9 - 0,017 \cdot L. \quad (1)$$

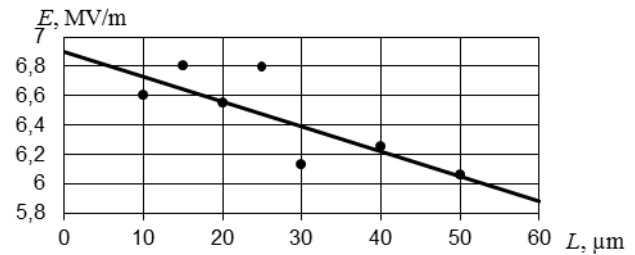


Fig. 2. Dependence of the breakdown strength of the electric field of the water gap on its length

The unambiguity of determining the breakdown ES of air is provided by information on the pore size, but such information is absent in [8]. Therefore, to explain the difference in the breakdown voltage of capacitor paper brands with a change in their thickness, a hypothesis was proposed that the electric fields in the samples under consideration are similar, and their quantitative characteristics – the potential and strength from point differ only by the proportionality coefficient. That is, for capacitor paper samples of different thicknesses, the equivalent dielectric permittivity must be constant.

Strongly ionized regions arising during partial or complete breakdown were modelled by a material with relative dielectric permittivity $\epsilon = 16000$. This value was chosen for the practical implementation of the model of an ideal conductor with $\epsilon \rightarrow \infty$, which is several times higher than the value of the maximum dielectric permittivity of the model materials. The rest of the physical parameters used in the model are given in Table 2.

Table 2

Name	Density at 20 °C, kg/m^3	ϵ_{20}
Cellulose	1530	6,5
Air	1,205	1,00058
Water	998	80,2

Research results. The dependencies of the breakdown EFS and voltage for air, obtained on the basis of the proposed model for a series of capacitor paper of the KOH 2 brand of various thicknesses, are shown in Fig. 3, and additional information is presented in Table 3.

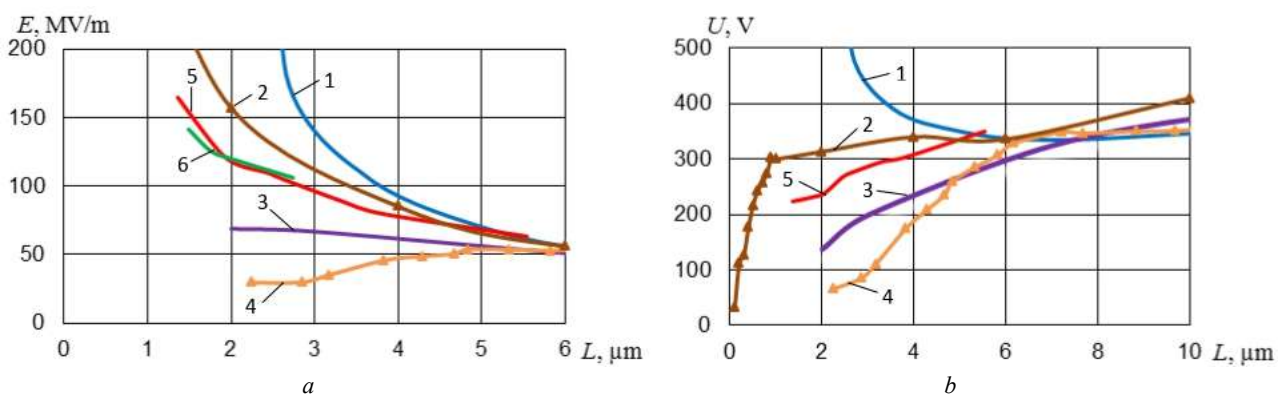


Fig. 3. Dependences of the breakdown strength (a) and breakdown voltage (b) of the air gap on its length, determined from the curves of Paschen (1), Peschot (2), Taev (3), Slade (4), and calculated according to the proposed model for a series of papers KOH 2 (5), KOH 3 (6)

Model parameters of capacitor paper KOH 2

Paper brand	Dimensions $h \times b \times l$, μm	Voltage amplitude U , V	Number of pores N	Air subregion length L_a , μm	Water subregion length L_w , μm	Relative equivalent dielectric permittivity ε	Water electric field strength module $E_w \cdot 10^{-6}$, V/m	
							maximum by model	by dependence (1)
KOH 2-30	$30 \times 190,08 \times 100$	975,80	24	5,54	3,76	5,241	2,41	6,836
KOH 2-18	$18 \times 202,36 \times 100$	721,24	33	3,78	2,56	5,241	3,44	6,856
KOH 2-15	$15 \times 184,72 \times 100$	664,68	33	3,31	2,23	5,234	3,73	6,862
KOH 2-12	$12 \times 165,44 \times 100$	622,26	37	2,63	1,79	5,217	4,30	6,870
KOH 2-10	$10 \times 150,84 \times 100$	537,40	33	2,43	1,65	5,217	4,40	6,872
KOH 2-8	$8 \times 134,92 \times 100$	494,98	33	2,07	1,39	5,238	4,34	6,876
KOH 2-6	$6 \times 116,80 \times 100$	395,98	27	1,84	1,24	5,264	5,34	6,879
KOH 2-4	$4 \times 95,40 \times 100$	339,42	27	1,36	0,92	5,232	6,60	6,884

Figure 3 also shows the dependencies obtained on the basis of the experimental Paschen curve [5] recalculated to normal atmospheric pressure, the Taev curve for electrodes made of a metal composition of silver and cadmium oxide [1], the Slade curve [2] and the Peschot curve determined in the high precision electrode positioning system with a breakdown criterion of 50 nA [4]. The construction of dependencies based on the numerical calculation of the electrostatic field began with the creation of a paper KOH 2-30 model. The value of the lateral side of the curvilinear trapezoid in the air segment of this model corresponds to the discharge gap of the Paschen curve with EFS equal to the modulus of the EFS vector averaged over the area of the indicated trapezoid. It should be noted that the distribution of the EFS in different air sectors is not the same. Therefore, the maximum value of the modulus of the averaged ES vector is taken as the breakdown one among the subregions located in the central part of the sample under consideration. Then, the equivalent dielectric permittivity was calculated using the energy method similar to [7]. The geometry of the next model of paper was selected so that its equivalent dielectric permittivity (within the error) was equal to the initial one determined for KOH 2-30.

Based on the values of the lateral side of the curved trapezoid and the maximum modulus of the averaged EFS

vector among all air segments in the central region of the sample, all subsequent points of the proposed dependencies were plotted. The obtained dependencies were verified by matching these curves and the known experimental point with coordinates 70 MV/m and 5 μm . The correctness of the obtained data is confirmed by the values of the moduli of the averaged EFS vectors over the areas of curvilinear trapezoids in the water segments of the pores of each model, which are less than the breakdown voltages for these gaps, determined by (1). However, after the breakdown of the air segment in water, the required value of the breakdown EFS is reached.

To confirm the obtained dependencies, a dependence was constructed in a similar way based on a series of capacitor paper of the KOH 3 brand of various thicknesses, shown in Fig. 3, a. The discrepancy between the values obtained for this section does not exceed 9 %.

On the basis of the proposed model, the minimum EFS value was determined at which a breakdown begins to develop in cellulose. For paper brand MKOH 0.8-15, the radius and the number of pores were calculated in accordance with the proposed EFS curve. A fragment of the region of the sample under study is shown in Fig. 4. For the subregion of cellulose with a lateral side of 0.34 μm , the EFS modulus was 141.5 MV/m, which is within the above range of values.

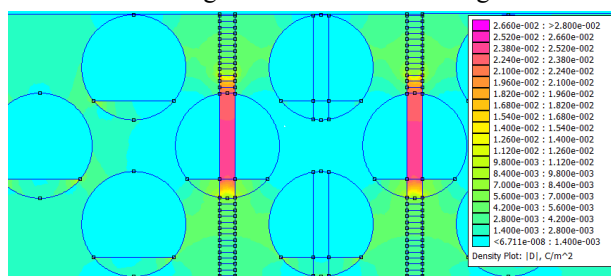


Fig. 4. Fragment of the distribution of the electrostatic field in MKOH 08-15 at partial breakdown

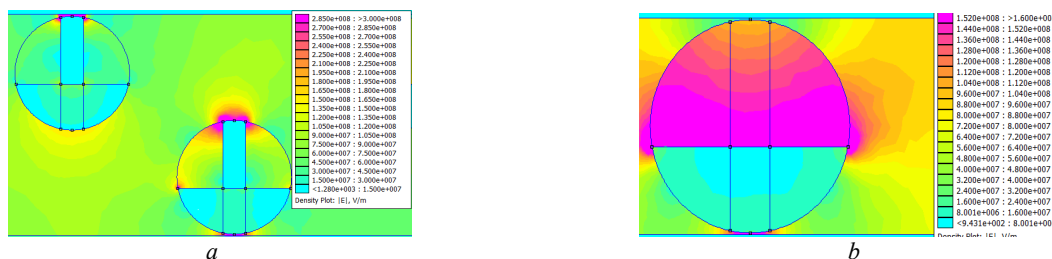


Fig. 5. Distribution of the electrostatic field during the development of breakdown according to Taev scenario for paper KOH 2-6 (a) and according to the Peschot scenario for paper KOH 2-4 (b)

The possibility of using the Taev curve to explain the breakdown mechanism of capacitor paper was verified using the example of a 1.84 μm discharge gap. The corresponding distribution of the electrostatic field is shown in Fig. 5,a. In this case, the breakdown EFS of cellulose is 1.6 times exceeded, which leads to the identity of the breakdown voltage for papers of different thicknesses. When using the Peschot curve, the question of the mechanical shear strength of paper KOH 2 samples with a thickness of 4...6 μs arises. It is also impossible to explain the value of the breakdown voltage of KOH 2-4. As seen from Fig. 5,b, the pore diameter is practically equal to the thickness of the paper KOH 2-4 sample, and the average EFS is 5.6 % less than the predicted value of the Peschot curve. In the range of 2.09...3.28 μm , the values of the EFS of the Peschot curve should be less by 1.6...7.1 % to explain the regularity of the breakdown voltage of the capacitor paper.

Conclusions. The dependence of the electric field strength of the air on the length of the discharge gap obtained in the work satisfactorily explains the values of the breakdown voltages of the samples of capacitor paper with a change in their brands and thickness. The best agreement of the obtained data is observed with the experimental Peschot dependence. The maximum divergence of the curves was 32 % in the range of discharge gaps 2.00...5.54 μm . The proposed method for numerical calculation of the breakdown voltage of air inclusions in the presence of water inclusions in the thickness of solid insulation can be applied to other types of solid thin-layer insulation.

REFERENCES

1. Gitlevich A.E., Mikhailov V.V., Parkanskii N.Ia., Revutskii V.M. *Elektroiskrovoe legirovanie metallicheskih poverkhnostei* [Electrospark alloying of metal surfaces]. Kishinev, Shtiintsa Publ., 1985. 198 p. (Rus).
2. Fu Y., Zhang P., Verboncoeur J.P., Wang X. Electrical breakdown from macro to micro/nano scales: a tutorial and a review of the state of the art. *Plasma Research Express*, Feb. 2020, vol. 2, no. 1, p. 013001. doi: 10.1088/2516-1067/ab6c84.

How to cite this article:

Palchykov O.O. Breakdown voltage of micron range air inclusions in capacitor paper. *Electrical engineering & electromechanics*, 2020, no. 6, pp. 30-34. doi: 10.20998/2074-272X.2020.6.05.

3. Babrauskas V. Arc breakdown in air over very small gap distances. *Conference: Interflam 2013*, vol. 2, pp. 1489-1498.
4. Peschot A., Bonifaci N., Lesaint O., Valadares C., Poulain C. Deviations from the Paschen's law at short gap distances from 100 nm to 10 μm in air and nitrogen. *Applied Physics Letters*, 2014, vol. 105, iss. 12, p. 123109. doi: 10.1063/1.4895630.
5. Bortnik I.M., Beloglovskii A.A., Vereshchagin I.P., Vershinin Iu.N. *Elektrofizicheskie osnovy tekhniki vysokikh napriazhenii* [Electrophysical basics of high voltage engineering]. Moscow, MEI Publ., 2016. 704 p. (Rus).
6. El-Zein A., El Bahy M. M., Talaat M. A prediction methodology of electrical tree propagation in solid dielectrics. *Journal of Electrical Engineering*, 2009, vol. 9 (2), pp. 87-93.
7. Palchykov O.O. Determination of the effective permittivity of a heterogeneous material. *Electrical engineering & electromechanics*, 2020, no. 2, pp. 59-63. doi: 10.20998/2074-272X.2020.2.09.
8. DSTU 3467-96. *Papir kondensatornyj. Zagal'ni tehnicni umovy* [State Standard 3467-96. Capacitor paper. General technical conditions]. Kyiv, Derzhstandart Ukraine Publ., 1996. 34 p. (Ukr).
9. Zhang T., Du J., Lei Y., Cheng Y., Liu W., Yi X., Yin J., Yu P. Effect of pores on dielectric breakdown strength of alumina ceramics via surface and volume effects. *Journal of the European Ceramic Society*, Jul. 2020, vol. 40, no. 8, pp. 3019-3026, doi: 10.1016/j.jeurceramsoc.2020.03.024.
10. *Entsiklopediia polimerov. T.1. Pod red. V. A. Kargina* [Encyclopedia of polymers. Vol. 1. Edited by V.A. Kargin]. Moscow, Sov. Ents. Publ., 1972. 1224 p. (Rus).
11. Osipenko V.I., Stupak D.O., Pozdeev S.V. Break-down of liquid by a number of impulses in wire electrodischarge machining. *Metal and casting of Ukraine*, 2009, no. 11-12, pp. 60-64. (Rus).

Received 29.09.2020

Accepted 16.10.2020

Published 24.12.2020

O.O. Palchykov, Candidate of Technical Science,
Admiral Makarov National University of Shipbuilding,
9, Heroyiv Ukraine Ave, Mykolaiv, Ukraine, 54025,
e-mail: ole2012hulk@gmail.com

B. Bourouis, H. Djeghloud, H. Benalla

AN INNOVATIVE ALGORITHM FOR A HYBRID FC/BATTERY SYSTEM ENERGY MANAGEMENT

Purpose. This paper targets to manage the energy of a hybrid fuel-cell (FC)/battery power system using an innovative algorithm. The hybrid FC/Battery power system is based on four stacks PEM FCs and a NiMH battery, boost and buck DC choppers for controlling the FC and the battery input currents respectively and a developed algorithm both for managing the power system energies and for delivering the FC and the battery reference output voltages compulsory for the DC/DC converters control circuits. The study is verified by means of computer simulations using MATLAB/Simulink where several cases of the battery SOC and the power demand levels were taken into account. The results demonstrate a good functioning of the proposed hybrid FC/Battery power system managing algorithm. References 25, tables 4, figures 17.

Key words: hybrid FC/battery system, PEM FC, NiMH battery, boosts and bucks DC/DC converters, innovative management algorithm.

Мета. Стаття спрямована на управління енергією гібридної системи живлення від паливного елемента/акумулятора за допомогою інноваційного алгоритму. Гібридна система живлення паливний елемент/акумулятор заснована на чотирьох батареях паливних елементів з протонообмінними мембранами та NiMH акумуляторі, підсилювачах і послаблювачах постійного струму для управління паливним елементом та вхідними струмами батареї відповідно та розробленому алгоритмі як для управління енергією енергосистеми, так і для подачі на паливний елемент і акумулятор вихідної напруги, обов'язкової для схем управління перетворювачами постійного струму. Дослідження перевірено за допомогою комп'ютерного моделювання з використанням MATLAB/Simulink, де було враховано кілька випадків рівня заряду акумулятора та рівнів споживання енергії. Результати демонструють добре функціонування запропонованого гібридного алгоритму управління системою живлення від паливного елемента/акумулятора. Бібл. 25, табл. 4, рис. 17.

Ключові слова: гібридна система паливний елемент/акумулятор, паливний елемент з протонообмінними мембранами, NiMH акумулятор, підсилювачі та перетворювачі постійного струму, інноваційний алгоритм управління.

Introduction. Fuel cell (FC) technology is known as the most cleaned converter of hydrogen into electrical energy which constitutes an advantageous alternative to polluting fossil fuel sources of electrical energy [1-4]. Moreover, FCs are highly efficient, modular and low cost with less weight and volume if compared to conventional power generation sources [5, 6]. Various technologies of FCs are commercialized but the low temperature proton exchange membrane (PEM) fuel cell is the most popular [7, 8].

However the PEMFCs response time is considerable which involves assistance of energy storage equipment to convey the energy to the loads which power demand varies rapidly [7], [9]. The hybridization of FCs is generally performed with batteries or super-capacitors or both of them [10, 11].

Particularly, when it is question of a hybrid FC/battery system, an energy management unit is primordial for achieving the optimal performances since both FCs and batteries face many challenges during the operational mode which influences on their lifetime and reliability [12].

Hybrid FC/battery systems can be found in diverse applications including but not limited to portable power generation, power transportation and stationary power generation [13].

In this paper, an innovative algorithm is presented for managing the energy of a hybrid FC/battery power system. The adopted FC is a PEM type whereas the battery is from NiMH technology. The energy management is based on controlling the FC and the battery input currents through DC/DC boost and buck

converters. Simulation tests on a resistive load were performed on a wide range of voltages.

System description. The considered system is depicted in Fig. 1. The system contains four stacks fuel-cell system, a battery, a unidirectional boost DC/DC converter, a bidirectional boost/buck DC/DC converter, and an energy management algorithm. Further details are reported in the following sections.

Model of the hybrid fuel-cell/battery system. FCs have the benefits of high efficiency since they transform fuel energy directly into electrical energy without any internal combustion. Nevertheless, they are heavy and bulky systems with long start-up and response times [14]. Hybridization of the FC with a battery, which is a peaking power source is an effective way to overcome the FC drawbacks. This is why the hybrid FC/battery system is considered in this contribution. The model of the fuel-cell/battery hybrid system is based on fuel cell and battery blocs available in the SimPowerSystem (SPS) library browser of MATLAB/Simulink.

1. Fuel cell model. Fuel cells are electrochemical devices organized in stacks that transform chemical energy from an electrolytic reaction to electrical energy, evacuating heat and water. Nevertheless, FCs remain incapable to supply a regulated DC voltage although they are a spotless source of energy. FCs found their utility in many applications such as power generation and co-generation plants, main power sources in remote locations (spacecrafts, weather station and so on), automotive appliances (cars, buses, motorcycles, bicycles, airplanes, forklifts, submarines and so on), and others (distributed generation, emergency

power systems, UPS's, notebook computers, small heating systems and so on). Many kinds of FCs exist namely: alkaline (AFC), proton exchanges membrane (PEMFC), phosphoric acid (PAFC), molten carbonates (MCFC), and

solid oxides (SOFC) [15]. PEMFCs are the most widespread fuel cells because of their low operating temperature compared to the other kinds (60-100 °C) [16].

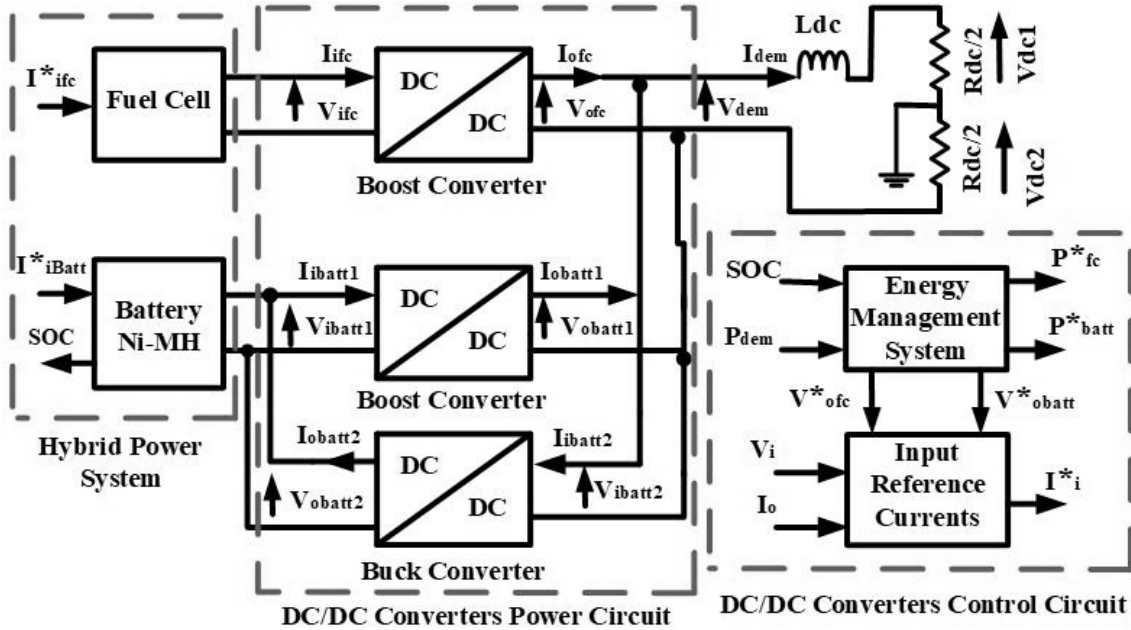


Fig. 1. Description of system

1.1. Modeling of the PEMFC. The SPS FC model is the approach proposed in [17]. The model of the FC stack implemented in SPS is shown in Fig. 2.

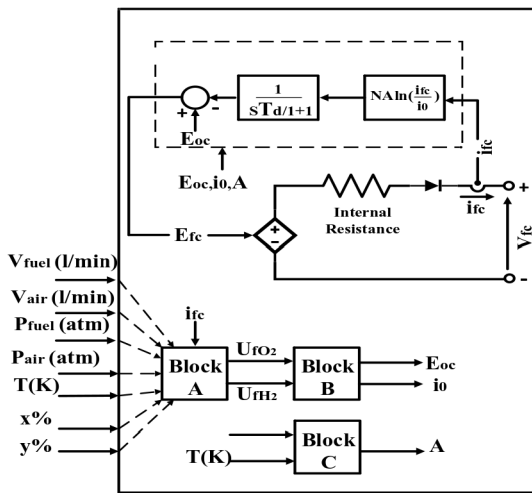


Fig. 2. Fuel cell stack model

• **Transient state.** This model is selected for this paper and the main equations are as follows [17]. The controlled voltage source (E_{fc}) is expressed as:

$$E_{fc} = E_{oc} - N \cdot A \cdot \ln\left(\frac{i_{fc}}{i_0}\right) \cdot \frac{1}{\frac{s \cdot T_d}{1} + 1}, \quad (1)$$

where E_{oc} – open circuit voltage, V; N – number of cells; A – Tafel slope, V; i_0 – exchange current, A; T_d – the response time, s; i_{fc} – fuel cell current, A.

The first order transfer function appearing in (1) represents the FC activation losses due to slowness in chemical reactions occurring in the electrodes surfaces.

These losses can be electrically modeled by a parallel RC circuit. Then T_d can be taken as 3 times the time constant $\tau = RC$. Thus the FC voltage considering both electrodes and electrolyte losses is determined from (2) :

$$V_{fc} = E_{fc} - R_{fc} \cdot i_{fc}, \quad (2)$$

where R_{fc} – internal resistance of the FC, Ω ; V_{fc} – fuel cell voltage, V; E_{oc} , i_0 , A are as follows:

$$E_{oc} = N_c \cdot E_n; \quad (3)$$

$$i_0 = \frac{z \cdot F \cdot k (P_{H_2} + P_{O_2})}{R \cdot h} \cdot e^{-\frac{\Delta G}{R \cdot T}}; \quad (4)$$

$$A = \frac{R \cdot T}{z \cdot a \cdot F}, \quad (5)$$

where $R = 8.3145$ J/(mol·K); $F = 96485$ A·s/mol; z – number of moving electrons ($z = 2$); E_n – Nernst voltage, V; a – charge transfer coefficient; P_{H_2} – partial pressure of hydrogen inside the stack, atm; P_{O_2} – partial pressure of oxygen inside the stack, atm; P_{H_2O} – partial pressure of water vapor, atm; w – percentage of water vapor in the oxidant, %; k – Boltzmann's constant ($1.38 \cdot 10^{-23}$ J/K); h – Planck's constant ($6.626 \cdot 10^{-34}$ J·s); ΔG – activation energy barrier, J; T – temperature of operation, K; K_c – voltage constant at nominal condition of operation.

$$E_n = \begin{cases} 1.229 + (T + 298) \cdot \frac{-44.43}{z \cdot F} + \frac{R \cdot T}{z \cdot F} \ln(P_{H_2} \cdot P_{O_2}^{1/2}) & T \leq 100^\circ C; \\ 1.229 + (T + 298) \cdot \frac{-44.43}{z \cdot F} + \frac{R \cdot T}{z \cdot F} \ln\left(\frac{P_{H_2} \cdot P_{O_2}^{1/2}}{P_{H_2O}}\right) & T > 100^\circ C; \end{cases} \quad (6)$$

$$P_{H_2} = (1 - U_{fH_2}) \cdot x \cdot P_{fuel}; \quad (7)$$

$$P_{O_2} = (1 - U_{fO_2}) \cdot y \cdot P_{air}; \quad (8)$$

$$P_{H_2O} = (w + 2 \cdot y \cdot U_{fO_2}) \cdot P_{air}; \quad (9)$$

$$U_{fH_2} = \frac{60000 \cdot R \cdot T \cdot N \cdot i_{fc}}{z \cdot F \cdot P_{fuel} \cdot V_{fuel} \cdot x}; \quad (10)$$

$$U_{fO_2} = \frac{60000 \cdot R \cdot T \cdot N \cdot i_{fc}}{2 \cdot z \cdot F \cdot P_{air} \cdot V_{air} \cdot y}, \quad (11)$$

where P_{fuel} – absolute supply pressure of fuel, atm; P_{air} – absolute supply pressure of air, atm; V_{fuel} – fuel flow rate, l/min; V_{air} – air flow rate, l/min; x – percentage of hydrogen in the fuel, %; y – percentage of oxygen in the oxidant, %.

The air compressor has a delay that results in a lack of oxygen inside the fuel cell. Consequently the utilization of the cell exceeds the nominal values which influence the Nernst voltage. This influence can be expressed as [17]:

$$E_{n(\text{modified})} = E_n - K_{fc} (U_{fO_2} - U_{fO_2(\text{nom})}); \quad (12)$$

where K_{fc} – voltage undershoots constant; $U_{fO_2(\text{nom})}$ – nominal oxygen utilization, %.

• **Steady state.** The modeling of the steady state consists of considering the previous equations with their given values (nominal values) and to suppress the transfer function.

$$V_1 = E_{oc} - N \cdot A \cdot \ln(i_0) - R_{fc}; \quad (13)$$

$$V_{\text{nom}} = E_{oc} - N \cdot A \cdot \ln\left(\frac{I_{\text{nom}}}{i_0}\right) - R_{fc} \cdot I_{\text{nom}}; \quad (14)$$

$$V_{\text{min}} = E_{oc} - N \cdot A \cdot \ln\left(\frac{I_{\text{max}}}{i_0}\right) - R_{fc} \cdot I_{\text{max}}, \quad (15)$$

where V_1 , V_{nom} and V_{min} are voltages corresponding to currents 1 A, I_{nom} and I_{max} respectively.

$$a = \frac{N \cdot R \cdot T_{\text{nom}}}{z \cdot F \cdot N \cdot A}; \quad (16)$$

$$\Delta G = -R \cdot T_{\text{nom}} \cdot \ln\left(\frac{i_0}{K_1}\right); \quad (17)$$

$$K_1 = \frac{2 \cdot F \cdot k \cdot (P_{H_2(\text{nom})} + P_{O_2(\text{nom})})}{h \cdot R}; \quad (18)$$

$$P_{H_2(\text{nom})} = x_{\text{nom}} \cdot (1 - U_{fH_2(\text{nom})}) \cdot P_{fuel(\text{nom})}; \quad (19)$$

$$P_{O_2(\text{nom})} = y_{\text{nom}} \cdot (1 - U_{fO_2(\text{nom})}) \cdot P_{air(\text{nom})}; \quad (20)$$

$$U_{fH_2(\text{nom})} = \frac{\eta_{\text{nom}} \cdot \Delta h \cdot (H_2O(\text{gas})) \cdot N}{2 \cdot F \cdot V_{\text{nom}}}; \quad (21)$$

$$U_{fO_2(\text{nom})} = \frac{60000 \cdot R \cdot T_{\text{nom}} \cdot N \cdot I_{\text{nom}}}{2 \cdot z \cdot F \cdot P_{air(\text{nom})} \cdot V_{air(\text{nom})} \cdot y_{\text{nom}}}; \quad (22)$$

$$K_c = \frac{E_{oc}}{E_{n(\text{nom})}}; \quad (23)$$

$$E_{n(\text{nom})} = E_n \left|_{U_{fH_2} = U_{fH_2(\text{nom})}, U_{fO_2} = U_{fO_2(\text{nom})}\right}; \quad (24)$$

$$K_{fc} = \frac{V_u}{K_c (U_{fO_2(\text{max})} - U_{fO_2(\text{nom})})}; \quad (25)$$

$$N \cdot A = \frac{(V_1 - V_{\text{nom}}) \cdot (I_{\text{max}} - 1) - (V_1 - V_{\text{min}}) \cdot (I_{\text{nom}} - 1)}{\ln(I_{\text{nom}}) \cdot (I_{\text{max}} - 1) - \ln(I_{\text{max}}) \cdot (I_{\text{nom}} - 1)}; \quad (26)$$

$$R_{fc} = \frac{V_1 - V_{\text{nom}} - N \cdot A \cdot \ln(I_{\text{nom}})}{I_{\text{nom}} - 1}; \quad (27)$$

$$i_0 = \exp\left(\frac{V_1 - E_{oc} + R_{fc}}{N \cdot A}\right). \quad (28)$$

Equations (16), (17), (23) and (25) determine the FC parameters.

1.2. Polarization curve of the considered (PEMFC). The polarization curves are V-I and P-I characteristics specified by two distinguished regions: the activation region and the ohmic region. In the V-I polarization curve, four particular voltages are shown: the open circuit voltage E_{oc} , the voltage V_1 corresponding to 1 A, V_{nom} and V_{min} corresponding to i_{max} . In the P-I polarization curve, three main powers can be observed: P_{idle} which is the power relating to 1 A, P_{nom} and P_{max} . A typical polarization curves is depicted in Fig. 3.

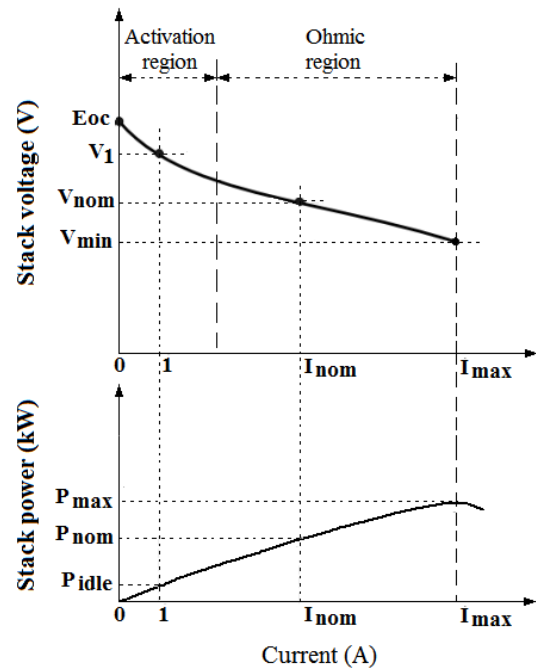


Fig. 3. Typical polarization curves

1.3. Validation of the Detailed Model. The dialog box of the FC SPS block allows to plot the ideal characteristics of one stack voltage and power vs. the stack current as shown in Fig. 4. These characteristics describe specific points corresponding to the nominal and the maximum currents which values are respectively 45 V, 37 V (which corresponds to the values mentioned in Table 1), 5.9985 kW, 8.325 kW. In this contribution, four stacks of PEMFCs are considered and which specifications are reported in Table 1 [17].

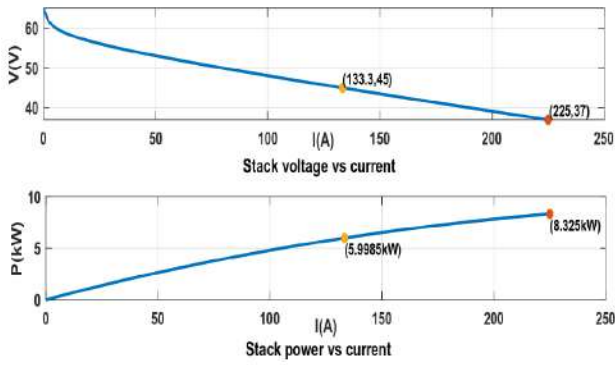


Fig. 4. Polarization curves of the considered stack

Table 1
Parameters of the preset 6 kW/45 V_{dc} fuel cell stack model

Parameter	Value
$[E_{oc}, V_1], V$	[65, 63]
$[I_{nom}, V_{nom}], A, V$	[133.3, 45]
$[I_{max}, V_{min}], A, V$	[225, 37]
N	65
$\eta_{nom}, \%$	55
$T_{nom}, ^\circ C$	65
$V_{airnom}, l/min$	300
$[P_{fuelnom}, P_{airnom}], bar$	[1.5, 1]
z	2
$[x_{nom}, y_{nom}, w_{nom}], \%$	[99.95, 21, 1]
T_d, s	1

2. Battery model. A battery is a device composed of one or more electrochemical cells that convert electrical energy into chemical energy during charging and the inverse during discharging where the electrolytes are able to move as ions within allowing the chemical reactions to be completed. Batteries have virtues of fast response speed, high ramp rates, easily sited, modular and good energy efficiency [18]. There are three main sorts of batteries: lead acid, nickel-based, and lithium-based [19]. The battery considered in this paper is of type Nickel-Metal-Hydride (Ni-MH) as they have proven to exhibit high energy density and efficiency, low prices and safety [20].

2.1. Modeling of the Ni-MH battery. The SPS battery model is the approach proposed in [21] and which is shown in Fig. 5. This model is selected for this paper and the main equations are as follows [22, 23]. The battery voltage either in charge or discharge modes is expressed by:

$$V_{batt} = E_{batt} - R_{batt} \cdot i, \quad (29)$$

where

$$E_{batt} = \begin{cases} E_0 - K_{batt} \frac{Q}{Q - i \cdot t} \cdot (i \cdot t + i^*) + Exp(t) \\ \text{- in discharge mode;} \\ E_0 - K_{batt} \frac{Q}{Q - i \cdot t} \cdot i \cdot t - K_{batt} \frac{Q}{|i \cdot t| - 0.1 \cdot Q} \cdot i^* + Exp(t) \\ \text{- in charge mode;} \end{cases} \quad (30)$$

$$\dot{Exp}(t) = V_{batt} |i \cdot t| \cdot (-Exp(t) + A_{batt} \cdot u(t)), \quad (31)$$

where V_{batt} – battery voltage, V; E_0 – battery constant

voltage, V; K_{batt} – polarization constant, V/A·h; Q – battery capacity, A·h; $i \cdot t = \int idt$ – actual battery charge, A·h; A_{batt} – exponential zone amplitude, V; B_{batt} – exponential zone time constant inverse (A·h) $^{-1}$; R_{batt} – internal resistance of the battery, Ω ; i – battery current, A; i^* – filtered current, A; $Exp(t)$ – exponential zone voltage, V; $i(t)$ – battery current, A; $u(t)$ – charge or discharge mode

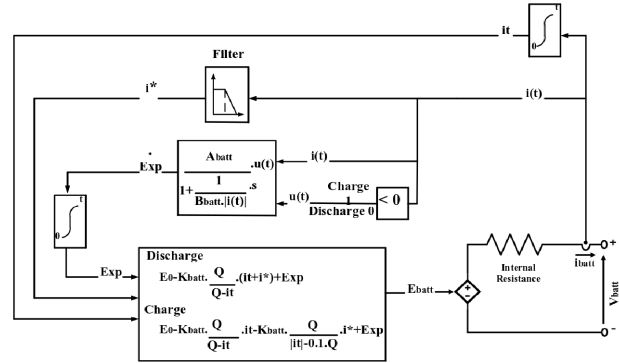


Fig. 5. Ni-MH battery model

2.2. Discharge and charge curves. Typical discharge and charge characteristics are illustrated in Fig. 6.

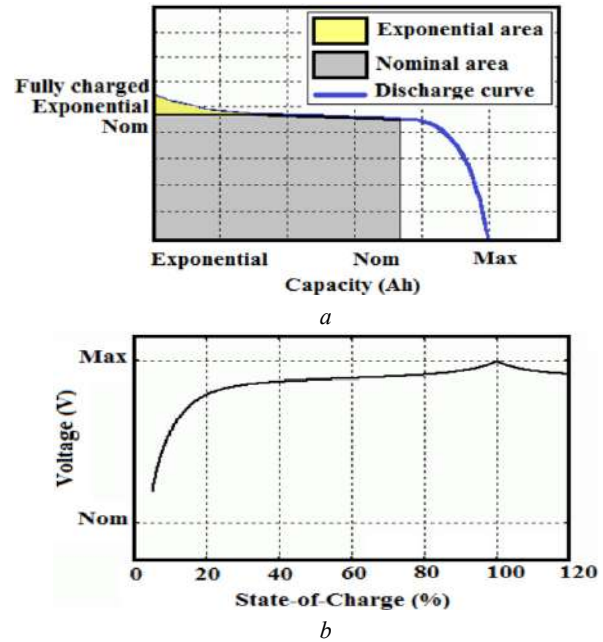


Fig. 6. Typical discharge and charge characteristics: discharge curve (a) and charge curve (b)

The discharge curve of battery voltage vs. capacity contains three zones (Fig. 6,a): the first zone (exponential area) where the voltage drops exponentially when the battery is charged; the second zone (nominal area) illustrating the charge that can be extracted from the battery until the voltage drops below the nominal value; the third part (discharge) which shows the total discharge of the battery when the voltage diminishes rapidly.

The charge curve of battery voltage vs. the State-Of-Charge (SOC) is depicted in Fig. 7. It describes four zones:

- zone I: $5\% < SOC < 20\%$, where the voltage increases rapidly;
- zone II: $20\% < SOC < 80\%$, where the voltage increases very slowly;
- zone III: $80\% < SOC < 100\%$, where the voltage starts to increase exponentially;
- zone IV: $SOC > 100\%$, a new cycle of exponential discharge begins.

2.3. Validation of the model. The parameters required by the model are illustrated in Table 2 extracted from Panasonic NiMH-HHR650D battery data sheet. The simulated discharge curves of the considered battery are shown in Fig. 7. The upper curve concerns the discharge for the nominal current where the three zones are clearly highlighted. The lower curves display the discharge characteristic for different currents (70 A, 90 A, 117 A). It is obvious that more the current is bigger more the discharge is faster.

Table 2

Battery model input parameters	
Parameter	Value
V_{batnom} , V	180
Q_{nom} , A·h	585
Q_{max} , A·h	630
V_{batmax} , V	212
I_{disnom} , A	117
R , Ω	0.0030769
$[V_{batexp}, Q_{exp}]$, V, A·h	[195.25 117]
Initial SOC, %	85
t_r , s	30

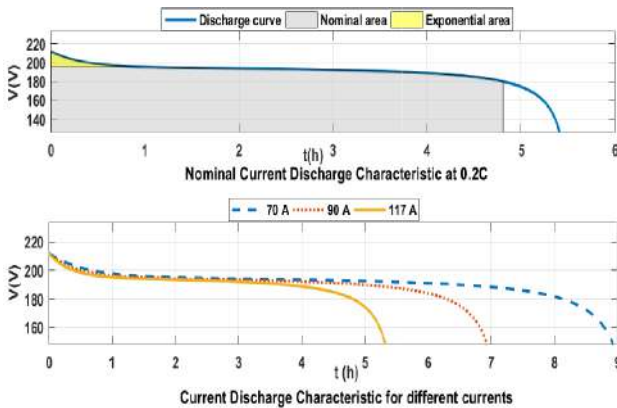


Fig. 7. Discharge curves of the considered battery

DC/DC converters models and control circuits. In this section models and control circuits of DC/DC converters used as interface between the hybrid FC/battery and the active power filter DC buses are presented. The considered DC/DC converters are operating in unidirectional boost mode for the FC and in bidirectional boost/buck modes for the battery (boost mode for discharging and buck mode for charging).

1. Models of DC/DC converters power circuits. In this part the average model is adopted since it is less time-consuming as the switches are substituted by controlled voltage and current sources [24].

Figure 8 shows the average models of the DC/DC converters. Figure 8,a concerns the buck mode whereas

Fig. 8,b illustrates the boost mode, where α_{boost} , α_{buck} are duty cycles of boost and buck modes respectively; η – efficiency, %; V_i , V_o are input and output measured voltages, V; I_i , I_o are input and output measured currents, A; L – smoothing inductance, H; C – filtering capacity, F.

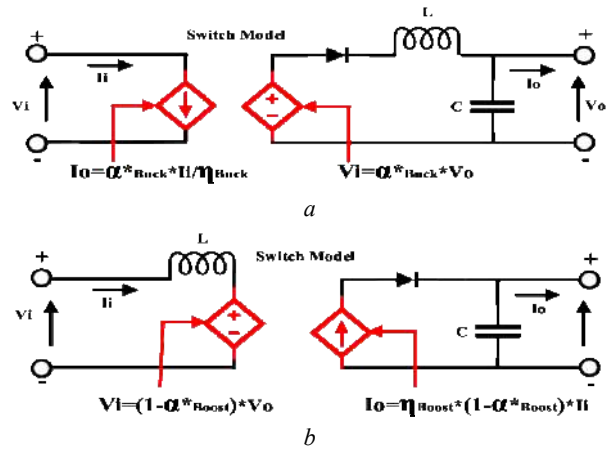


Fig. 8. DC/DC Power circuit buck mode (a) and boost mode (b)

2. Control circuits. The principle of the control circuit is to provide both the FC and the battery with their respective input reference currents (I_{fc}^* , I_{batt}^*) as mentioned in Fig. 1. For that, the control approach is organized in two steps: generating at first the output reference voltages (V_{ofc}^* , V_{oBat}^*) and then the input reference currents (I_{ifc}^* , I_{iBat}^*). The first step is carried-out from the algorithm of energy management. The second step is performed in the block of input reference current on-line identification.

2.1. Energy management algorithm. The idea of this algorithm was inspired from [19] related to hybrid electric vehicle system. The algorithm receives data about the demand power measured at the DC/DC converters terminals (P_{dem}) and the battery state of charge (SOC), then it realizes energy management in such a way to express reference FC and battery powers (P_{fc}^* , P_{batt}^*) depending on the SOC rate. The algorithm inputs also values of FC idle, low and high powers ($P_{fc\ idle}$, $P_{fc\ low}$, and $P_{fc\ high}$) and battery maximum power ($P_{batt\ max}$). As resumed in Fig. 9, different situations can be considered according to the demand power rate (high, medium, low) and the state of charge of battery (*discharged* – $SOC < 40\%$, *little charged* – $SOC > 40\%$, *high charged* – $SOC < 80\%$, and *completely charged* – $SOC > 80\%$).

High demand power $P_{fc\ high} < P_{dem} < P_{fc\ high} + P_{bat\ max}$.

- If $SOC < 40\%$. The battery can't provide power to satisfy the high demand. Then, the FC can just feed the DC bus and can't ensure power to charge the battery:

$$P_{fc}^* = P_{dem}, P_{batt}^* = 0.$$

- If $SOC > 40\%$. The battery can contribute to satisfy P_{dem} .

- If P_{dem} is very high $P_{dem} > P_{fc\ high} + P_{bat\ max}$. The battery and the FC work together for feeding the DC bus (hybrid powering): $P_{fc}^* = P_{dem} - P_{batt}$, $P_{batt}^* = P_{bat\ max}$.

- If P_{dem} is high $P_{fc\ high} < P_{dem} < P_{fc\ high} + P_{bat\ max}$. The battery continues to help the FC to feed the DC bus (hybrid powering): $P_{fc}^* = P_{fc\ high}$, $P_{batt}^* = P_{fc}^* - P_{dem}$.

Medium demand power $P_{low} < P_{dem} < P_{fc\ high}$.

- If SOC < 80 %. Since the demand power is less high and the battery is not completely charged. Thus, the FC power can simultaneously satisfy P_{dem} and charge the battery: $P_{fc}^* = P_{fc\ high}$, $P_{batt}^* = P_{fc}^* - P_{dem}$.
- If SOC > 80%. In this case, the battery is completely charged. So, there is no need to share the FC power between the DC bus and the battery: $P_{fc}^* = P_{dem}$, $P_{batt}^* = 0$.

Low demand power $P_{idle} < P_{dem} < P_{low}$.

- If SOC < 80 %. The battery lacks of little amount of charge. Then it needs to be charged from the FC even P_{fc}^* is low. Accordingly P_{fc}^* will be shared between P_{dem} and P_{batt}^* : $P_{fc}^* = P_{fc\ low}$, $P_{batt}^* = P_{fc}^* - P_{dem}$.
- If SOC > 80 %. The major amount of power needed from the DC bus comes from the completely charged battery, the FC being at its weakest power $P_{fc\ idle}$: $P_{fc}^* = P_{fc\ idle}$, $P_{batt}^* = P_{dem} - P_{fc}^*$.

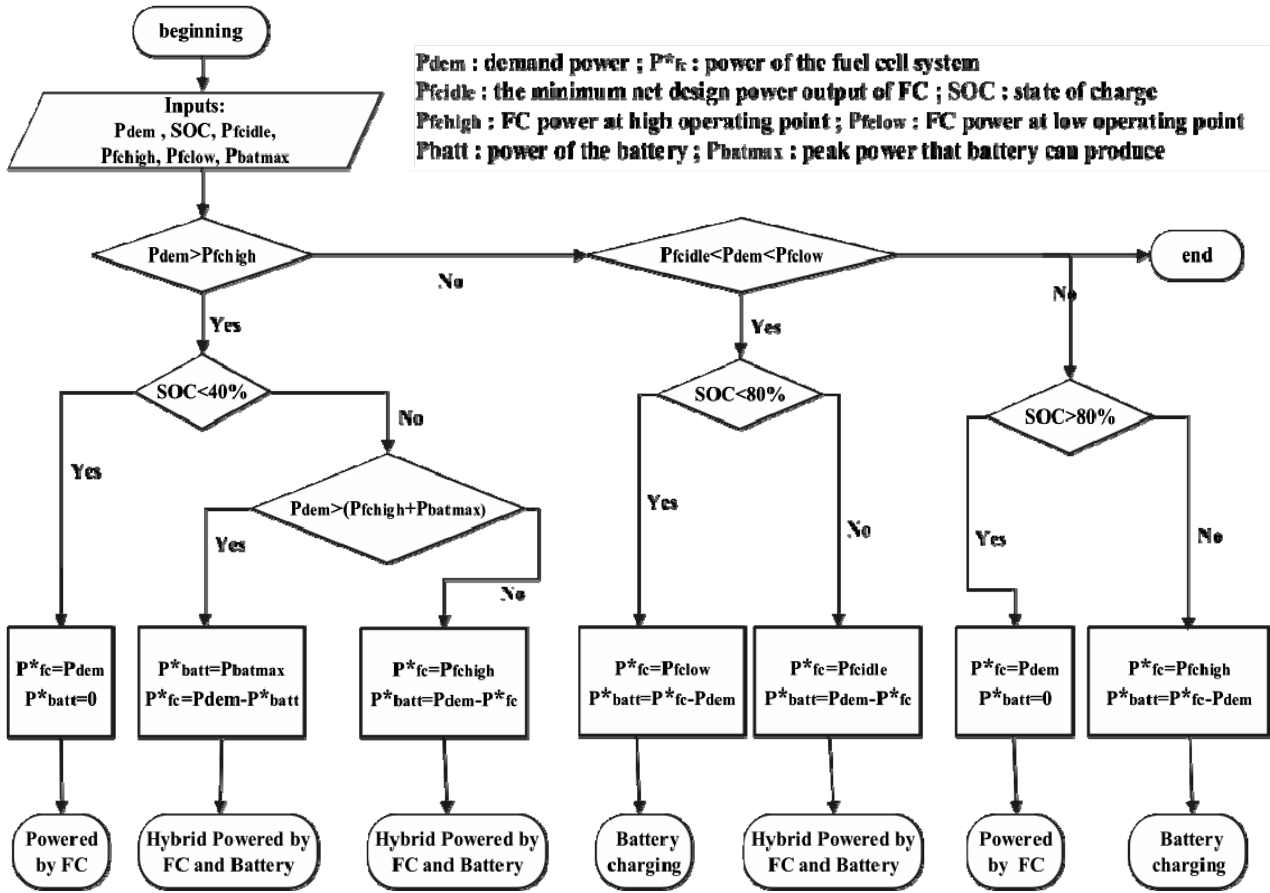


Fig. 9. Energy management algorithm

Once the FC and battery reference powers are carried-out from algorithm. Reference voltage can be easily deduced from:

$$V_{ofc}^* = \frac{P_{fc}^*}{I_{ofc}}; \quad (32)$$

$$V_{obatt}^* = \frac{P_{batt}^*}{I_{obatt}}. \quad (33)$$

To determine $P_{fc\ idle}$, $P_{fc\ low}$, and $P_{fc\ high}$, one can use the characteristics showed in Fig. 10 representing one cell voltage, one stack net power density and one stack efficiency vs. one cell current. $P_{fc\ idle}$ is the power corresponding to 1 A. $P_{fc\ low}$ and $P_{fc\ high}$ are the powers around 50 % of the efficiency curve (in it rising and falling regions respectively) obtained at 50 % of the nominal current.

Considering a 24 FC of 4 series connected stacks kW (each stack is rated at 6 kW, 45 V). Then, $P_{fc\ idle}$, $P_{fc\ low}$, and $P_{fc\ high}$ can be deduced by multiplying the stack specific powers extracted from Fig. 11 by 4.

To obtain $P_{batt\ max}$, one can use the following formula:

$$P_{batt\ max} = V_{batt\ max} \cdot I_{disnom}, \quad (34)$$

where $V_{batt\ max}$ – fully charged voltage, V; I_{disnom} – nominal discharge current, A.

2.2. Input reference current on-line identification.

The DC/DC converter input current can be subtracted from the efficiency formula given by:

$$\eta = \frac{P_o}{P_i} = \frac{I_o \cdot V_o}{I_i \cdot V_i}. \quad (35)$$

For the reference input current, one can substitute I_i by I_i^* and V_o by V_o^* , this latter is provided by the algorithm which justifies the on-line aspect in this identification:

$$I_i^* = \frac{I_o \cdot V_o^*}{V_i \cdot \eta_{boost}}, \text{ boost mode}; \quad (36)$$

$$I_i^* = \frac{I_o \cdot V_o^* \cdot \eta_{buck}}{V_i}, \text{ buck mode}. \quad (37)$$

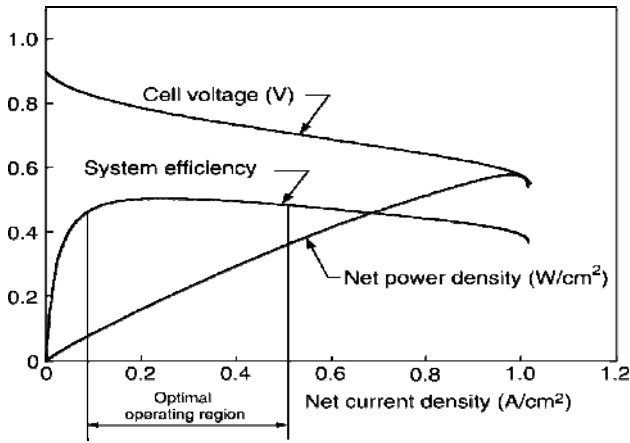


Fig. 10. Typical operating characteristics of a fuel cell system

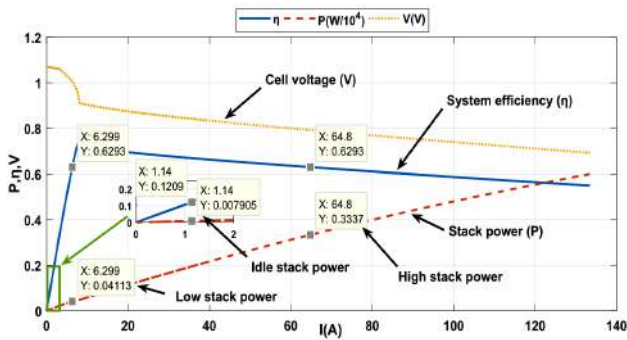


Fig. 11. Operating characteristics of the considered stack

To obtain the efficiency (η), a two dimensional mapping data (Fig. 12) provided by the manufacturer BRUSA BDC546 DC/DC converter is adopted [25]. The data was implemented in 2-D look-up tables having in their entries the duty cycle α of the considered mode and the output current I_o . The duty cycles of boost and buck modes are respectively given by:

$$\alpha_{boost} = 1 - \frac{V_o}{V_i}; \quad (38)$$

$$\alpha_{buck} = \frac{V_o}{V_i}. \quad (39)$$

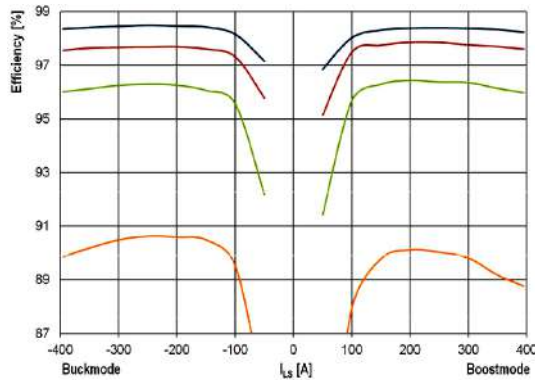


Fig. 12. Power DC/DC efficiency map [25]

The block schemes of the on-line reference input current identification in both modes boost and buck are depicted in Fig. 13.

The unidirectional DC/DC converter operates only in the boost mode during powering mode for delivering

the power required by the load while the bidirectional DC/DC converter operates both in boost and buck modes during powering and charging modes.

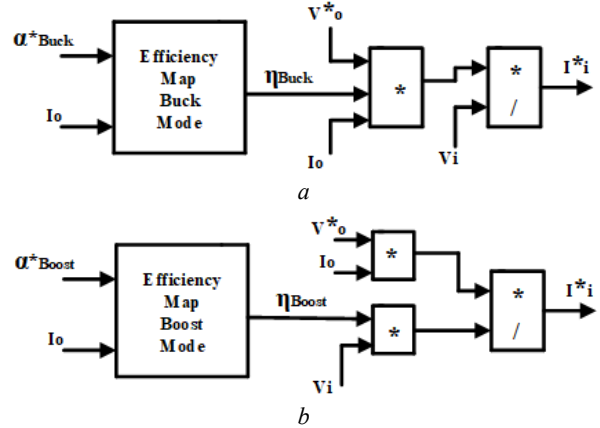


Fig. 13. DC/DC control circuit buck mode (a) and boost mode (b)

Simulation results discussion. In this section simulation works about the previous study are presented. They were carried out using MATLAB/Simulink software and considering the parameters reported in Table 3.

Table 3

Simulation parameters

Parameter	Value
P_{fcnom}	24 kW
P_{batmax}	21 kW
$P_{fc idle}$	316.2 W
P_{fclow}	1.6452 kW
P_{fchigh}	13.348 kW
$\alpha_{fcboost}$	[0.45, 0.51, 0.81, 0.81, 0.9, 0.7, 0.58]
$\alpha_{battboost}$	[0.5, 0, 0.83, 0, 0.88, 0, 0]
$\alpha_{battbuck}$	[0, 0.38, 0, 0, 0, 0.29, 0]
SOC	[85, 70, 50, 35, 50, 70, 85] (%)

The principle of the simulations studies consists to impose time varying duty cycles ($\alpha_{fcboost}$, $\alpha_{battboost}$ and $\alpha_{battbuck}$) and SOC then to extract the corresponding input and output DC/DC converters voltages, reference powers (P_{dem}^* , P_{fc}^* , P_{batt}^*) and measured powers (P_{dem} , P_{fc} , P_{batt}). Finally, the measured powers are compared to the reference powers.

Figure 14 represents the imposed duty cycles and SOCs. In some time intervals one can observe that $\alpha_{battboost}$ takes the value 0, this occurs when the battery is incapable to help the FC to satisfy P_{dem} (case of SOC < 40 % and $P_{dem} > P_{fchigh}$) or when P_{dem} is not high, then the FC has no need to the battery help (case of SOC > 80 % and $P_{dem} < P_{fclow}$), or when P_{dem} is very low and the battery SOC is little inferior to 80 % (case of SOC < 80 % and $P_{dem} < P_{fclow}$), or when P_{dem} is quite low and SOC is also little inferior to 80 % (case of SOC < 80 % and $P_{dem} > P_{fclow}$). The same observation can be pointed out with $\alpha_{battbuck}$ which values are different to 0 only when the battery is charging from the FC (case SOC < 80 % and $P_{dem} < P_{fclow}$ or SOC < 80 % and $P_{dem} > P_{fclow}$), otherwise, it takes the value 0. Consequently, the battery

converters do not work all time. They work only when the battery power is required to help the FC to satisfy P_{dem} provided that the SOC is comprised between 40 % and 80 % or when the battery is in charging mode (the SOC is little inferior to 80 % and $P_{dem} < P_{fc}$).

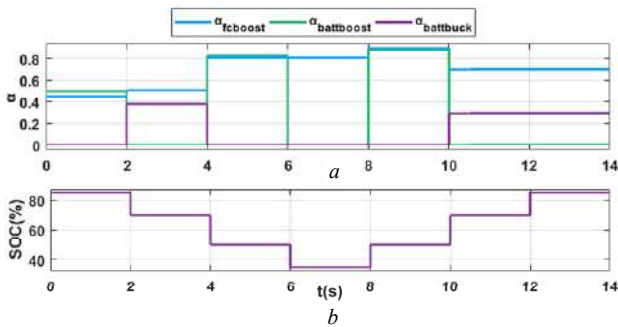


Fig. 14. Duty cycles of DC/DC FC and battery converters (a) and state of charge (SOC) (b)

Figure 15 shows the obtained output voltages of DC/DC FC and battery boost converters and DC/DC battery buck converter. It is obvious that the FC boost converter works all time since its output voltage V_{ofc} is continuously greater than its input voltage V_{ifc} as illustrated in Fig. 15,a. However, the battery DC/DC boost converter operates only when the FC is incapable to fulfill P_{dem} alone and when SOC is greater than 40 % or 80 %. As shown in Fig. 15,b, from the beginning to 5 s, the FC power is very low ($P_{fc} = P_{fcidle}$) whereas $P_{fcidle} < P_{dem} < P_{fcflow}$ then, the battery is switched on to compensate the lack of power. Similarly, it is switched on once again between 10 s and 15 s when P_{dem} is high ($P_{dem} > P_{fchigh}$), then the FC can not feed the DC bus alone which involves the help of the battery in order to satisfy P_{dem} . Finally, the battery is once more switched on when P_{dem} is very high ($P_{dem} > P_{fchigh} + P_{batmax}$) from 20 to 25 s. All these situations result in the battery boost voltage presented in Fig. 15,c where V_{obatt1} is sometimes equal to V_{ibatt1} when the battery is switched off ($\alpha_{battboost} = 0$), otherwise it is always greater than V_{ibatt1} when the battery is switched on ($\alpha_{battboost} \neq 0$). Now, when P_{dem} is low ($P_{fcidle} < P_{dem} < P_{fcflow}$) and quite low ($P_{fcflow} < P_{dem} < P_{fchigh}$) and SOC is little inferior to 80 %, the DC/DC buck converter is operational to charge the battery; this occurs between 5 s and 10 s and between 25 s and 30 s as depicted in Fig. 15,c. Finally, Fig. 15,d shows the obtained demand voltage V_{dem} which is all time equal to V_{ofc} , V_{obatt1} and V_{ibatt2} since the outputs of the FC and the battery boost converters are connected in parallel with the input of the battery DC/DC buck converter.

In Fig. 16, the currents curves are presented. In each one of parts (a, b and c) of this Fig. 16 is plotted the measured input current and its reference and the measured output current of each converter. The most important observation is the perfect agreement between the input current and its reference. Figure 16,d represents the demand current which max value is 30 A corresponding the max $V_{dcm_{max}}$ 1550 V giving an apparent power of 48.6 kVA.

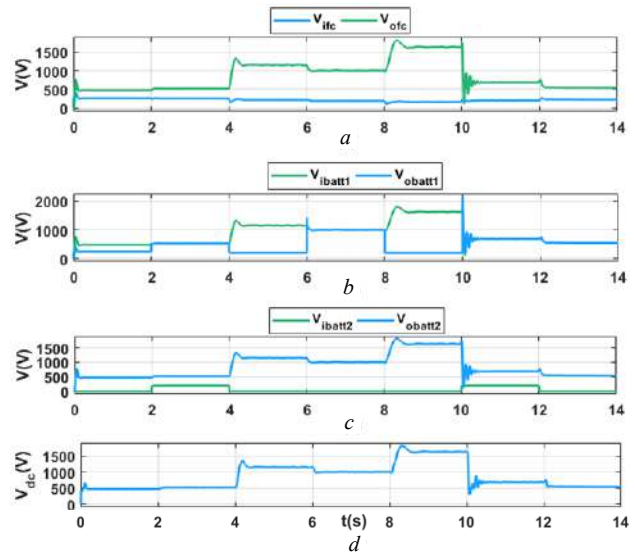


Fig. 15. Input and output voltages of DC/DC converters DC/DC FC boost converter (a), DC/DC battery boost converter (b), DC/DC battery buck converter (c), and demand voltage (d)

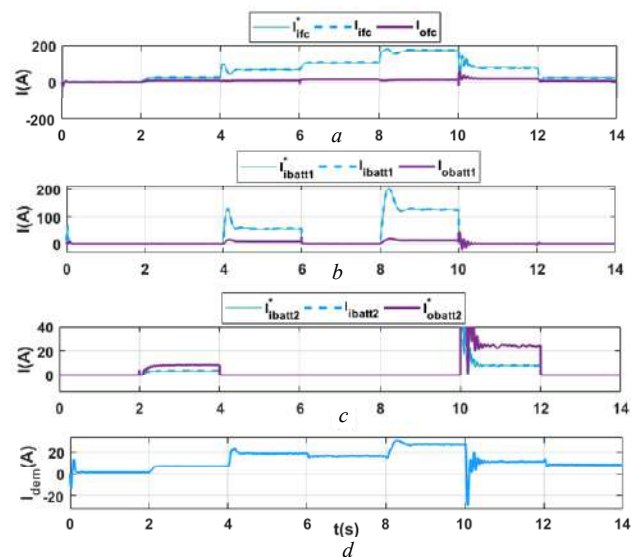


Fig. 16. Input and output currents of DC/DC converters DC/DC FC boost converter (a), DC/DC battery boost converter (b), DC/DC battery buck converter (c), and demand current (d)

The last set of figures (Fig. 17) concerns the measured powers curves of the FC (Fig. 17,a), the battery (Fig. 17,b) and the demand (Fig. 17,c) and their respective reference powers.

As first statement measured powers and their corresponding references are almost tight most of the time. Indeed, one can see a good settlement between FC and battery powers and their references P_{fc}^* , P_{batt}^* (Fig. 17,a, Fig. 17,b) especially when P_{dem} is low ($P_{fcidle} < P_{dem} < P_{fcflow}$) and medium ($P_{fcflow} < P_{dem} < P_{fchigh}$), however, P_{dem} and its reference P_{dem}^* are perfectly tight all time (Fig. 17,c).

Recall that reference powers are delivered from energy management algorithm developed in previous section.

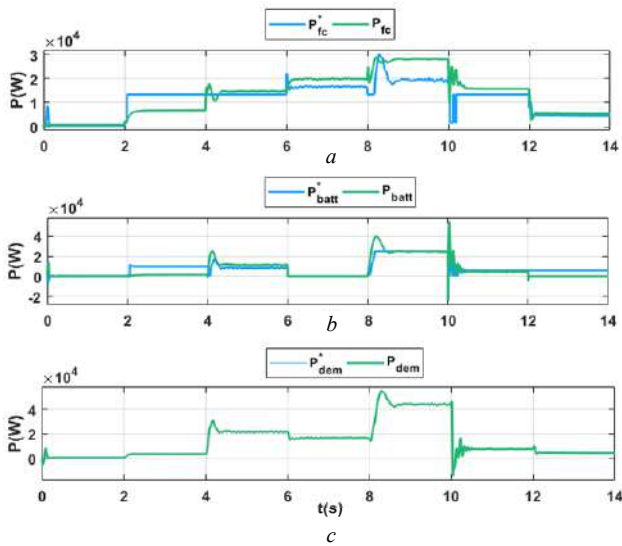


Fig. 17. Reference and measured powers of fuel cell (a), battery (b), and demand (c)

Conclusion.

The work, presented in this paper, concerns a hybrid FC/battery DC power system.

Firstly, theoretical studies about FC and battery systems are stated.

Secondly, the adopted average models of boost and buck FC and battery DC/DC converters and their control strategies are exposed where a big focus is given to the innovated energy management algorithm and the input DC/DC converters reference currents on-line identification using the efficiency map-based method.

Finally, the presented works are numerically verified through computer MATLAB/Simulink simulations. The studies are based on an adequate choice of the DC/DC converters duty cycles and the battery SOC, as well as the FC/battery specific powers ($P_{fc\text{high}}$, $P_{fc\text{low}}$, $P_{fc\text{idle}}$, $P_{bat\text{max}}$). The battery converters are functional only when the battery is needed to help the FC to satisfy P_{dem} provided that (SOC > 80 % or SOC > 40 %) or when the battery SOC is little inferior to 80 % and the FC power is greater than P_{dem} .

All these situations are summarized in Table 4.

The obtained results demonstrate the algorithm satisfactory operation.

Table 4
Conditions of battery DC/DC converters working

	$\alpha_{fc\text{boost}}$	$\alpha_{fc\text{boost}}$
$P_{fc\text{idle}} < P_{dem} < P_{fc\text{low}}, P_{fc} = P_{fc\text{idle}}, \text{SOC} > 80 \%$	$\neq 0$	$= 0$
$P_{fc\text{high}} < P_{dem} < P_{fc\text{high}} + P_{bat\text{max}}, P_{fc} = P_{fc\text{high}}, \text{SOC} > 40 \%$	$\neq 0$	$= 0$
$P_{dem} > P_{fc\text{high}} + P_{bat\text{max}}, P_{fc} = P_{fc\text{high}}, \text{SOC} > 40 \%$	$\neq 0$	$= 0$
$P_{fc\text{idle}} < P_{dem} < P_{fc\text{low}}, P_{fc} = P_{fc\text{low}}, \text{SOC} < 80 \%$	$= 0$	$\neq 0$
$P_{fc\text{low}} < P_{dem} < P_{fc\text{high}}, P_{fc} = P_{fc\text{high}}, \text{SOC} < 80 \%$	$= 0$	$\neq 0$
$P_{fc\text{high}} < P_{dem} < P_{fc\text{high}} + P_{bat\text{max}}, P_{fc} = P_{fc\text{high}}, \text{SOC} < 40 \%$	$= 0$	$= 0$
$P_{fc\text{low}} < P_{dem} < P_{fc\text{high}}, P_{fc} = P_{fc\text{high}}, \text{SOC} > 80 \%$	$= 0$	$= 0$

The continuation of the contribution concerns the use of the managed P_{dem} to feed a three-level shunt active power filter (3L-SAPF) and to study the impact on the power quality. Moreover, development of a regulation loops to carry out the DC/DC converters duty cycles automatically is envisaged. Also, energy efficiency study of the whole system is being considered.

REFERENCES

- Odeim F., Roes J., Heinzl A. Power management optimization of a fuel cell/battery/supercapacitor hybrid system for transit bus applications. *IEEE Transactions on Vehicular Technology*, 2016, vol. 65, no. 7, pp. 5783-5788. doi: 10.1109/TVT.2015.2456232.
- Matthey J. *Fuel cell today. The leading authority on fuel cells*. Available at: <http://www.fuelcelltoday.com> (accessed 08 March 2020).
- Sun L., Wu G., Xue Y., Shen J., Li D., Lee K.Y. Coordinated control strategies for fuel cell power plant in a microgrid. *IEEE Transactions on Energy Conversion*, 2018, vol. 33, no. 1, pp. 1-9. doi: 10.1109/TEC.2017.2729881.
- Thounthong P., Rael S., Davat B. Control algorithm of fuel cell and batteries for distributed generation system. *IEEE Transactions on Energy Conversion*, 2008, vol. 23, no. 1, pp. 148-155. doi: 10.1109/TEC.2006.888028.
- Boscaino V., Collura R., Capponi G., Marino F. A fuel cell-battery hybrid power supply for portable applications. *SPEEDAM 2010*, Pisa, 2010, pp. 580-585. doi: 10.1109/SPEEDAM.2010.5542091.
- Lai J.-S., Ellis M.W. Fuel cell power systems and applications. *Proceedings of the IEEE*, 2017, vol. 105, no. 11, pp. 2166-2190. doi: 10.1109/JPROC.2017.2723561.
- Hong Z., Zhu Y., Shang W., Li Q., Chen W. Research of energy management strategy for fuel cell/battery hybrid locomotive. *2017 IEEE Transportation Electrification Conference and Expo, Asia-Pacific (ITEC Asia-Pacific)*, 2017, pp. 1-5. doi: 10.1109/ITEC-AP.2017.8080852
- Li Y.H., Rajakaruna S., Choi S.S. Control of a solid oxide fuel cell power plant in a grid-connected system. *IEEE Transactions on Energy Conversion*, 2007, vol. 22, no. 2, pp. 405-413. doi: 10.1109/TEC.2005.853756.
- Vural B., Dusmez S., Uzunoglu M., Ugur E., Akin B. Fuel consumption comparison of different battery/ultra capacitor hybridization topologies for fuel-cell vehicles on a test bench. *IEEE Journal of Emerging and Selected Topics in Power Electronics*, 2014, vol. 2, no. 3, pp. 552-561. doi: 10.1109/JESTPE.2013.2297702.
- Vural B., Boynuegri A.R., Nakir I., Erdinc O., Balikli A., Uzunoglu M., Gorgun H., Dusmez S. Fuel cell and ultra-capacitor hybridization: A prototype test bench based analysis of different energy management strategies for vehicular applications. *International Journal of Hydrogen Energy*, 2010, vol. 35, no. 20, pp. 11161-11171. doi: 10.1016/j.ijhydene.2010.07.063.
- Gao W. Performance comparison of a fuel cell-battery hybrid powertrain and a fuel cell-ultracapacitor hybrid powertrain. *IEEE Transactions on Vehicular Technology*, 2005, vol. 54, no. 3, pp. 846-855. doi: 10.1109/TVT.2005.847229.
- Reddy N.P., Padeloup D., Zadeh M.K., Skjetne R. An intelligent power and energy management system for fuel cell/battery hybrid electric vehicle using reinforcement learning. *IEEE Transportation Electrification Conference*, 2019, pp. 1-6. doi: 10.1109/ITEC.2019.8790451.
- Yu S., Fernando T., Chau T.K., Iu H. H.-C. Voltage control strategies for solid oxide fuel cell energy system connected to complex power grids using dynamic state estimation and STATCOM. *IEEE Transactions on Power Systems*, 2017, vol. 32, no. 4, pp. 3136-3145. doi: 10.1109/TPWRS.2016.2615075.

14. Ehsani M. *Modern electric, hybrid electric, and fuel cell vehicles: fundamentals, theory, and design*. Power electronics and applications series. Boca Raton, CRC Press, 2005.
15. Saïssset R. Contribution à l'étude systématique de dispositifs énergétiques à composants électrochimiques. Formalisme Bond Graph appliqué aux piles à combustible, accumulateurs Lithium-Ion, *Véhicule Solaire (PhD)*, 2004.
16. *Fuel Cell Technologies Program: Glossary*. Department of Energy efficiency and Renewable Energy Fuel Cell Technologies Program, 2011.
17. Motapon S.N., Tremblay O., Dessaint L.A. A generic fuel cell model for the simulation of fuel cell vehicles. *IEEE Vehicle Power and Propulsion Conference*, 2009, pp. 1722-1729. doi: **10.1109/VPPC.2009.5289692**.
18. Price A. Electrical energy storage – a review of technology options. *Proceedings of the Institution of Civil Engineers – Civil Engineering*, 2005, vol. 158, no. 6, pp. 52-58. doi: **10.1680/cien.2005.158.6.52**.
19. Tangsiripaisan M.P. *Modeling of fuel cell vehicle based on physical model of different components in MATLAB/Simulink*. 2007.
20. Kawachi S., Baba J., Kikuchi T., Shimoda E., Numata S., Masada E., Nitta T. Energy capacity reduction of energy storage system in microgrid stabilized by cascade control system. *13th European Conference on Power Electronics and Applications*, 2009, pp. 1-10.
21. Tremblay O., Dessaint L., Dekkiche A. A generic battery model for the dynamic simulation of hybrid electric vehicles. *IEEE Vehicle Power and Propulsion Conference*, 2007, pp. 284-289. doi: **10.1109/VPPC.2007.4544139**.
22. Shepherd C.M. Design of primary and secondary cells – Part 2. An equation describing battery discharge. *Journal of Electrochemical Society*, 1965, Vol. 112, pp. 657-664.
23. Tremblay O., Dessaint L.-A. Experimental validation of a battery dynamic model for EV applications. *World Electric Vehicle Journal*, 2009, vol. 3, no. 2, pp. 289-298. doi: **10.3390/wevj3020289**.
24. Njoya Motapon S., Dessaint L.-A., Al-Haddad K. A comparative study of energy management schemes for a fuel-cell hybrid emergency power system of more-electric aircraft. *IEEE Transactions on Industrial Electronics*, 2014, vol. 61, no. 3, pp. 1320-1334. doi: **10.1109/TIE.2013.2257152**.
25. Available at: <http://www.brusa.biz/en/products/dc-dc-converter/hvhv-800-v/bdc546.html> (accessed 12 March 2020).

Received 26.04.2020

Accepted 03.10.2020

Published 24.12.2020

Billel Bourouis¹, PhD Student

Hind Djeghloud², Lecturer

Hocine Benalla¹, Professor

¹ Laboratory of Electrotechnics of Constantine (LEC),

Mentouri Brothers University, Constantine 1,

Campus Ahmed Hamani Zerzara,

Route d'Ain el Bey, Constantine, 25000, Algeria.

² Laboratory of Electrical Engineering of Constantine (LGEC),

Mentouri Brothers University, Constantine 1,

Campus Ahmed Hamani Zerzara,

Route d'Ain el Bey, Constantine, 25000, Algeria.

e-mail: billelbourouis1@outlook.com,

hind.djeghloud@umc.edu.dz,

hocine.benalla@umc.edu.dz

How to cite this article:

Bourouis B., Djeghloud H., Benalla H. An innovative algorithm for a hybrid FC/battery system energy management. *Electrical engineering & electromechanics*, 2020, no. 6, pp. 35-44. doi: **10.20998/2074-272X.2020.6.06**.

R. Kouadri, L. Slimani, T. Bouktir

SLIME MOULD ALGORITHM FOR PRACTICAL OPTIMAL POWER FLOW SOLUTIONS INCORPORATING STOCHASTIC WIND POWER AND STATIC VAR COMPENSATOR DEVICE

Purpose. This paper proposes the application procedure of a new metaheuristic technique in a practical electrical power system to solve optimal power flow problems, this technique namely the slime mould algorithm (SMA) which is inspired by the swarming behavior and morphology of slime mould in nature. This study aims to test and verify the effectiveness of the proposed algorithm to get good solutions for optimal power flow problems by incorporating stochastic wind power generation and static VAR compensators devices. In this context, different cases are considered in order to minimize the total generation cost, reduction of active power losses as well as improving voltage profile. *Methodology.* The objective function of our problem is considered to be the minimum the total costs of conventional power generation and stochastic wind power generation with satisfying the power system constraints. The stochastic wind power function considers the penalty cost due to the underestimation and the reserve cost due to the overestimation of available wind power. In this work, the function of Weibull probability density is used to model and characterize the distributions of wind speed. The proposed algorithm was examined on the IEEE-30 bus system and a large Algerian electrical test system with 114 buses. In the cases with the objective is to minimize the conventional power generation, the achieved results in both of the testing power systems showed that the slime mould algorithm performs better than other existing optimization techniques. Additionally, the achieved results with incorporating the wind power and static VAR compensator devices illustrate the effectiveness and performances of the proposed algorithm compared to the ant lion optimizer algorithm in terms of convergence to the global optimal solution. References 38, tables 6, figures 9.

Key words: optimal power flow, slime mould algorithm, stochastic wind power generation, static VAR compensators.

Мета. У статті пропонується процедура застосування нового метаевристического методу в реальній електроенергетичній системі для розв'язання задач оптимального потоку енергії, а саме алгоритму слизової цвєлі, який заснований на поведінці рою і морфології слизової цвєлі в природі. Дане дослідження спрямоване на тестування і перевірку ефективності запропонованого алгоритму для отримання хороших рішень для проблем оптимального потоку потужності шляхом включення пристроїв стохастичною вітровою генерації і статичних компенсаторів VAR. У зв'язку з цим, розглядаються різні випадки, щоб мінімізувати загальну вартість генерації, знизити втрати активної потужності і поліпшити профіль напруги. *Методологія.* В якості цільової функції завдання розглядається мінімальна сукупна вартість традиційної генерації електроенергії і стохастичної вітровою генерації при задоволенні обмежень енергосистеми. Стохастична функція енергії вітру враховує величини штрафів через недооцінку і резервні витрати через завищену оцінку доступної вітровою енергії. У даній роботі функція щільності ймовірності Вейбулла використовується для моделювання і характеристики розподілів швидкості вітру. *Практична цінність.* Запропонований алгоритм був перевірений на системі шин IEEE-30 і великій алжирській тестовій енергосистемі зі 114 шинами. У випадках, коли мета полягає в тому, щоб звести до мінімуму традиційне вироблення електроенергії, досягнуті результати в обох тестових енергосистемах показали, що алгоритм слизової цвєлі функціонує краще, ніж інші існуючі методи оптимізації. Крім того, досягнуті результати з використанням вітровою енергії і статичного компенсатора VAR ілюструють ефективність і продуктивність запропонованого алгоритму в порівнянні з алгоритмом оптимізатора мурашиних левів з точки зору збіжності до глобального оптимального рішення. Бібл. 38, табл. 6, рис. 9.

Ключові слова: оптимальний потік енергії, алгоритм слизової цвєлі, стохастична генерація енергії вітру, статичні VAR компенсатори.

Introduction. In the last decade, energy consumption has been increased significantly especially in developing countries. Renewable energy can be known as green energy or clean energy is one of the best solutions to the increasing demand problem, and it is inexhaustible energy that comes from natural resources or processes that are constantly replenished [1], even if their availability depends on weather and weather conditions, and whose exploitation causes the least possible ecological damage, does not cause toxic waste and does not cause damage to the environment. They are cleaner, more environmentally friendly than fossil fuels and fissile energies, environmentally friendly, available in large quantities around the world.

Nowadays, the integration of renewable energy sources – RESs (i.e., solar, wind, hydropower, etc.) into the electrical grid is experiencing a rapid increase. Among the various RESs, wind energy considered is one of the most desirable sources in recent years that keeps

developing thanks to the technological advances made in the field of wind generators to reduce the cost of system installations. In addition, the application of flexible AC transmission systems (FACTS) controllers such as static VAR compensators (SVC) devices that considered one of the most controllers used in the case of the high demand for energy to maintain the magnitude of bus voltage at the desired level, improve voltage security and minimize the total power losses.

With the growing penetration of RESs in the power system, the study of optimal power flow (OPF) becomes necessary to solve power system problems or improve the performance of this system. The OPF for the system that includes RESs such as wind power generators is the subject of ongoing research models nowadays. It is necessary to confront the stochastic nature of this source for analysis of the planning and operation of modern power systems, in order to obtain much more precise

results [2]. In general, the problem with wind power is the stochastic nature of wind speed. Therefore the model which considers the probability of the available wind power can represent the cost of overestimating and underestimating this power at a certain period.

Recently, OPF with stochastic wind power has extensively been studied by more researchers. In [3] authors proposed a Gbest-guided artificial bee colony algorithm (GABC) to solve the OPF problem in the IEEE 30 bus system incorporating stochastic wind power. In attempting the same problem in [4] author proposed a modified moth swarm algorithm (MMSA) to solve the OPF problem incorporating stochastic wind power. In this work, three different objective functions are considered, which are the minimize the total operating cost, reduce the transmission power loss, and improve the voltage profile enhancement. In another study [5] authors applied the success history-based adaptation technique of differential evolution algorithm to solve the OPF problem comprises of stochastic wind-solar power with conventional thermal generators under various cases. The OPF incorporation with wind power and static synchronous compensator STATCOM was studied in [6] by using a modified bacteria foraging algorithm (MBFA). The results obtained proved that MBFA efficiency and better than the ACO algorithm for solving OPF problems in power systems. Bird Swarm Algorithm (BSA) for solving an OPF problem with incorporating stochastic wind and solar PV power in the power system is studied in [7]. The proposed approach applied in the modified IEEE 30-bus system with objective function is to minimize the total energy generation cost, which is the cost of thermal-wind-solar. In [8] authors applied a modified hybrid PSO-GSA with a chaotic maps approach to improve OPF results by incorporating stochastic wind power and two controllers in the FACTS family such as TCSCs and TCPSSs. The proposed method is applied in the power systems to minimize the thermal generators' fuel cost and the wind power generating cost.

Several metaheuristic optimization algorithms were developed and applied for the OPF solution. Some of them are: salp swarm optimizer [9], moth swarm algorithm [10], differential evolution [11], glowworm swarm optimization [12], differential search algorithm [12], moth-flame optimizer [14], stud krill herd algorithm [15], artificial bee colony algorithm [16], symbiotic organisms search algorithm [17], improved colliding bodies optimization algorithm [18], firefly algorithm [19], black-hole-based optimization approach [20], the league championship algorithm [21, 22], multi-verse optimizer [23], harmony search algorithm [24], earthworm optimization algorithm [25]. Among several numbers of the available metaheuristic algorithm, a new flexible and efficient stochastic optimization algorithm has been proposed to solve our problem and satisfy our imposed conditions, this technique namely a slime mould algorithm (SMA). SMA is based upon the oscillation mode in nature and simulates the swarming behavior and morphology of slime mould in foraging.

In this paper, a new flexible and efficient stochastic optimization algorithm called slime mould algorithm (SMA) has been proposed with the aim is solving the

OPF problem in power systems incorporating stochastic wind power and SVC devices.

Modeling of SVC. The static VAR compensator (SVC) device is an important member of the FACTS controllers' family. The importance of SVC is to maintain the bus voltage magnitude at the desired level by providing or absorbing reactive energy. In the power system, SVC is modeled by shunt variable admittance. SVC's admittance only has its imaginary part since the SVC device's power loss is assumed to be negligible and is given as follows:

$$y_{SVC} = jb_{SVC}. \quad (1)$$

The b_{SVC} susceptance can be capacitive or inductive to provide or absorb reactive power, respectively. In this study, SVC is installed in the power system as a PV bus with the objective is to regulate the voltage magnitude V_k by injecting reactive power to a bus where it is connected. The current I_{SVC} and reactive power Q_{SVC} absorbed or injected by the SVC device is calculated as follow:

$$I_{SVC} = jb_{SVC}V_k; \quad (2)$$

$$Q_{SVC} = -V_k^2 b_{SVC}. \quad (3)$$

Optimal power flow problem formulation. The optimal power flow problem solution aims to give the optimum value of the objective function by adjusting the settings of control variables. Generally, the mathematical expression of the optimization problem with satisfying various equality and inequality constraints may be represented as follows:

$$\min F(\mathbf{x}, \mathbf{u}); \quad (4)$$

$$\text{Subjected to } g(\mathbf{x}, \mathbf{u}) = 0; \quad (5)$$

$$h(\mathbf{x}, \mathbf{u}) \leq 0; \quad (6)$$

where $F(x, u)$ denotes the objective function that to be optimized, \mathbf{x} and \mathbf{u} represents the vectors of the state variables (dependent variables) and control variables (independent variables), respectively.

Control variables. In the OPF the control variables should be adjusted to satisfy the load flow equations. The set of control variables can be represented by vector \mathbf{u} as follows:

$$\mathbf{u} = \left[P_{G_2} \dots P_{G_{NG}}, P_{WS_1} \dots P_{WS_{NW}}, V_{G_1} \dots V_{G_{NG}}, Q_{C_1} \dots Q_{C_{NC}}, T_1 \dots T_{NT}, SVC_1 \dots SVC_{NSVC} \right], \quad (7)$$

where P_G is the thermal generator active power; P_{WS} is the wind active power; V_G is the generator voltage; Q_C is the reactive power injected by the shunts compensator; T is the tap setting of transformers; SVC is the static VAR compensator; NG is the number of generators; NW is the number of wind farms; NC is the number of shunts compensators units; NT is the number of regulating transformers; $NSVC$ is the number of SVC devices.

State variables. The set of variables which describe the electrical power state can be represented by vector \mathbf{x} as follows:

$$\mathbf{x} = [P_{Gslack}, Q_{G_1} \dots Q_{G_{NG}}, Q_{WS_1} \dots Q_{WS_{NW}}, V_{L_1} \dots V_{L_{NL}}, S_{l_1} \dots S_{l_m}], \quad (8)$$

where P_{Gslack} is the active power generation at the slack bus; Q_G is the reactive power outputs of the generators; Q_{WS} is the reactive power outputs of the wind farms; V_L is the voltage magnitude at load bus; S_l is the apparent power flow; N_G is the total number of generators buses;

N_L is the total number of load buses or PQ buses; N_l is the total number of transmission lines.

Equality constraints. The equality constraints represent in the power system the load flow equations of the balanced powers and reflect the physics of the power system. The equality constraints can be represented as follows:

$$P_{G_i} + P_{WS_i} - P_{d_i} = V_i \sum_{j=1}^N V_j (g_{ij} \cos \delta_{ij} + z_{ij} \sin \delta_{ij}), \quad (9)$$

$$Q_{G_i} + Q_{WS_i} - Q_{d_i} = V_i \sum_{j=1}^N V_j (g_{ij} \sin \delta_{ij} + z_{ij} \cos \delta_{ij}). \quad (10)$$

Inequality constraints. The inequality constraints reflect the limiting of the power system operation. These inequality constraints can be represented as follows:

$$\begin{cases} P_{G_i}^{\min} \leq P_{G_i} \leq P_{G_i}^{\max}; \\ P_{WS_i}^{\min} \leq P_{WS_i} \leq P_{WS_i}^{\max}; \\ Q_{G_i}^{\min} \leq Q_{G_i} \leq Q_{G_i}^{\max}; \\ Q_{WS_i}^{\min} \leq Q_{WS_i} \leq Q_{WS_i}^{\max}; \\ V_{G_i}^{\min} \leq V_{G_i} \leq V_{G_i}^{\max}; \\ T_{NT_i}^{\min} \leq T_{NT_i} \leq T_{NT_i}^{\max}; \\ Q_{SVC_i}^{\min} \leq Q_{SVC_i} \leq Q_{SVC_i}^{\max}; \\ |S_{L_i}| \leq S_{L_i}^{\max}. \end{cases} \quad (11)$$

Objective function. In this study, the objective function is to minimize the total generation cost (TGC) subject to operating constraints. The objective function is formulated as:

$$F_{tot} = \sum_{i=1}^N F_i(P_i) + \sum_{i=1}^{NW} C_{wr}(P_{wr}) + \sum_{i=1}^{NW} C_{p.wr}(P_{wr.av} - P_{wr}) + \sum_{i=1}^{NW} C_{r.wr}(P_{wr} - P_{wr.av}), \quad (12)$$

In the expression of the objective function formulated in the (12), the first term denotes thermal power generation cost, second, third and last term of the objective function shows the costs of wind power, respectively. Details of all terms are explained below.

Fuel cost of the conventional generator. The cost function of the thermal generators as follows:

$$F_i(P_i) = \left(\sum_{i=1}^N a_i + b_i P_{G_i} + c_i P_{G_i}^2 \right), \quad (13)$$

where P_{G_i} is the active power generated from the available thermal generators; a_i , b_i and c_i are the cost coefficients of i -th generator.

The direct cost function for wind power. The grid operators pay the cost of purchasing wind power from a wind power producer based on the power purchase agreement. This cost is termed as the direct cost and is defined as follows [5]:

$$C_{wr}(P_{wr}) = d_r \cdot P_{wr}, \quad (14)$$

where d_r is the direct cost coefficient for the j -th wind generator and P_{wr} is the scheduled power output.

Cost function due to the underestimation. The underestimation situation is due when the actual wind power is higher than the estimated value. So, the utility operator needs to pay a penalty cost for not using the surplus amount of available wind power [4, 5]. The penalty cost functions due to the underestimation of available wind power represented by (15), it can be given as [26]:

$$C_{p.wr}(P_{wr.av} - P_{wr}) = k_p (P_{wr.av} - P_{wr}) = k_p \int_{P_{wr}}^{P_{r,0}} (W - P_{wr}) \cdot f_w(P_w), \quad (15)$$

where $C_{p.wr}$ is the cost associated with wind power shortage (underestimation); $P_{p.wr}$ is the actual available power output; k_p is the penalty cost coefficient due to underestimation and $f_w(P_w)$ represents the probability density function (PDF).

Cost function due to the overestimation. On contrary to the underestimation situation, the overestimation situation is due when the actual wind power is less than the estimated value. So, a spinning reserve is needed for grid operators [5]. The penalty cost function due to the overestimation of available wind power represented by (16) as follows [27]:

$$C_{r.wr}(P_{wr} - P_{wr.av}) = k_r (P_{wr} - P_{wr.av}) = k_r \int_0^{P_{wr}} (P_{wr} - W) \cdot f_w(P_w), \quad (16)$$

where $C_{r.wr}$ the cost associated with wind power surplus (overestimation) and k_r is the reserve cost coefficient due to overestimation.

Wind power model. The distribution function was used in this work to model and characterize the distributions of wind speed known as Weibull probability density function (PDF) [28], and can be represented as:

$$f_V(V) = \frac{k}{c} \left(\frac{v}{c} \right)^{k-1} e^{-\left(\frac{v}{c} \right)^k}, \quad (17)$$

here v is the wind speed; k and c respectively the shape factor and scale factor (m/s).

The probability density function for the continuous portion of wind energy conversion systems (WECS) power output random variable becomes as follows:

$$f_w(P_w) = \frac{k \cdot l \cdot v_{cut-in}}{c} \left(\frac{(1 + \rho \cdot 1) v_{cut-in}}{c} \right)^{k-1} \times \exp \left(- \left(\frac{(1 + \rho \cdot 1) v_{cut-in}}{c} \right)^k \right), \quad (18)$$

where $l = (v_{rated} - v_{cut-in}) / v_{cut-in}$ is the ration of linear range wind speed to cut-in wind speed; v_{cut-in} is the wind speed at which wind turbine starts to generate power; $v_{cut-off}$ is the wind speed at which the wind turbine is disconnected; v_{rated} is the wind speed at which the mechanical power output will be the rated power; $\rho = P_w / P_{wr}$ is the ratio of wind power output to rated wind power.

The probability for the discrete portion of the WECS power output is expressed by (19) and (20), respectively as follows [5, 29]:

$$f_w(P_w) = \{P_w = 0\} = 1 - \exp\left(-\left(\frac{v_{cut-in}}{c}\right)^k\right) + \exp\left(-\left(\frac{v_{cut-off}}{c}\right)^k\right); \quad (19)$$

$$f_w(P_w) = \{P_w = P_{wr}\} = \exp\left(-\left(\frac{v_{rated}}{c}\right)^k\right) - \exp\left(-\left(\frac{v_{cut-off}}{c}\right)^k\right); \quad (20)$$

Slime mould algorithm. A slime mould algorithm (SMA) is a new stochastic optimizer technique nature-inspired proposed in 2020 in [30]. This technique based on the oscillation mode of slime mould in nature and simulates the swarming behavior and morphology of slime mould in foraging. The SMA algorithm features a special mathematical model that uses the adaptive weight to simulates the combination of positive and negative feedback from the bio-oscillator-based propagation wave that was inspired by slime mould to form the optimal pathway to connect food. Some of the most interesting characters in the slime mould are the unique pattern based on the various food sources to create a venous network connecting them at the same time. This scheme gives the high capability of escaping from local optima solutions. The algorithm is aroused by slime mold diffusion and foraging behavior. In SMA, slime mould can approach food, depending on the smell in the air. The slime mold morphology varies, with three different forms of contraction. The following section will explain in detail the mathematical model for simulating the behavior of slime mould during the foraging [30].

Approach food. The following formulas for imitating the contraction mode is proposed to model the behavior of slime mould to approaching food according to the odor in the air as follow:

$$\vec{X}(t+1) = \begin{cases} \vec{X}_B(t) + \vec{vb} \cdot (\vec{W} \cdot \vec{X}_A(t) - \vec{X}_B(t)), & r < p; \\ \vec{vc} \cdot \vec{X}(t), & r \geq p, \end{cases} \quad (21)$$

where X denotes the slime mould location; X_b is the individual emplacement with the highest odor concentration currently found; X_A and X_B are indicated two randomly selected individuals from the swarm; vb is a parameter distributed in the range of $[-a, a]$; vc decreases linearly from 1 to 0; t shows the current iteration; W represents the slime mould weight and given below by (24); p is the parameter given as follows:

$$p = \tanh|S(i) - DF|, \quad (22)$$

where $S(i)$ shows the fitness of \vec{X} ; $i \in 1, 2, \dots, n$; DF is the optimum fitness obtained in all iterations.

The parameter of a is given as follows:

$$a = \arctan h\left(-\left(\frac{t}{\max_t}\right) + 1\right). \quad (23)$$

The expression of \vec{W} define the location of slime mould and is given as follows:

$$\vec{W}(\text{SmellIndex}(i)) = \begin{cases} 1 + r \cdot \log\left(\frac{bF - S(i)}{bF - wF} + 1\right), & \text{condition;} \\ 1 - r \cdot \log\left(\frac{bF - S(i)}{bF - wF} + 1\right), & \text{others,} \end{cases} \quad (24)$$

where *condition* denotes that $S(i)$ is ranked first half of the population; r represents the random value distributed in the range of $[0, 1]$; bF and wF are represented the optimal and worst fitness value obtained in the current iterative process, respectively; *SmellIndex* represents the sequence of fitness values sorted as:

$$\text{SmellIndex} = \text{Sort}(S). \quad (25)$$

Wrap food. This portion mathematically simulates the contraction mode in the slime mould venous tissue structure while searching. In this context, the higher the food concentration reached by the vein, the stronger the bio-oscillator-generated wave, the quicker the cytoplasm flows and the thicker the vein. The following mathematical formula represents updating the emplacement of slime mould:

$$\vec{X}^* = \begin{cases} \text{rand} \cdot (ub - lb) + lb, & \text{rand} < z; \\ \vec{X}_B(t) + \vec{vb} \cdot (\vec{W} \cdot \vec{X}_A(t) - \vec{X}_B(t)), & r < p; \\ \vec{vc} \cdot \vec{X}(t), & r \geq p, \end{cases} \quad (26)$$

where lb and ub denote the lower and upper limits of the search range, respectively; *rand* denotes the random value distributed in the range of in $[0, 1]$.

Grabble food. Slime mould is primarily dependent on the propagation wave to change the cytoplasmic flow in the veins, so they appear to be in a better concentration of food. Slime mould can approach food faster when the concentration and quality of food are high, while if the food concentration is lower, approach it more slowly, thus increasing the efficiency of slime mould in selecting the optimal source of food.

In the SMA process, the value of the parameter \vec{vb} oscillates randomly in the interval between $[-a, a]$ and progressively approaches zero as the iterations increase. The value of \vec{vc} oscillates randomly in the interval between $[-1, 1]$ and finally tends to be zero.

The pseudo-code of the SMA to solve the OPF problem is shown in Algorithm 1.

Algorithm 1 Pseudo-code SMA algorithm

Read the system data (bus data, line data, and generator data);
Initialize the parameters of search agents, size of the population, the maximum number of iterations, the number and position of the control variables;
Initialize the position of the slime mould X_i using (21);
While *iteration* \leq *Max_iteration*,
 Calculate the fitness of all slime mould using (26);
 Update the best fitness, X_B
 Calculate the W by using (24);
 For each search space
 Update the parameters of SMA which are: p , vb and vc ;
 Update the best positions of the slime mould;
 Calculate the best value of the objective function (12);
 End For *iter* = *iter* + 1;
End while
Return *best Fitness* found so far, X_B .

Simulations and results. To demonstrate the performance and efficiency of the SMA algorithm to solve the OPF problem by incorporating stochastic wind power and FACTS devices such as SVC, the present work aims to apply the SMA on IEEE 30-bus and Algerian 114-bus systems with different test cases study. In this context, the minimization of total fuel cost and wind power cost is considered as objective functions. The description of all these test cases can be found in the following section. All the simulations are carried out by using MATLAB 2009b and computed with specification Intel® Core™ i5 CPU@1.80 GHz with 8 GB of RAM. For establishing the robustness of the SMA algorithm, 30 independent trial runs are performed for all the test cases. In this work, the population size is 40 and the number of iterations maximal is 500.

IEEE 30-bus test system. The first test is dedicated to the standard IEEE 30-bus power system in order to verify the performance and efficiency of the SMA for the small scale power system. This system includes 6 generators unit, 41 transmission lines, 4 transformers located at lines 6-9, 4-12, 9-12, and 27-28. Nine reactive compensators are located at buses 10, 12, 15, 17, 20, 21, 23, 24, and 29. The total load is $(2.834 + j0.735)$ p.u.

The upper limit and lower limit variables are shown in Table 1. In this section, two different parts are considered, the first part is solving the OPF problem under normal conditions and the second part is solving the OPF problem under the contingency state.

OPF solution under normal condition. In this part, the SMA is applied to solve the OPF problem under the normal condition with active power loading is 283.4 MW. Three different cases are examined via SMA as follows.

Case 1: Minimization of total fuel cost. The objective function used in the first case under normal condition is to minimize the total fuel cost according to the optimal power distribution of the production units and is described by (13). Table 3 tabulates the results obtained by the SMA algorithm for Case 1. It can be seen that the optimal settings of control variables are all within their acceptable limits. Furthermore, we can also see that the fuel cost obtained by SMA is 798.9709 \$/h, this value is lower and better compared to those obtained by MSA, GSO, MFO, BHBO, ALO, MSCA which are mentioned in Table 1.

Table 1

Comparison of solutions achieved using SMA and different methods for Case 1

Method	Fuel cost (\$/h)
Slime mould algorithm	798.9709
Moth swarm algorithm [10]	800.5099
Glowworm Swarm Optimization [12]	799.06
Moth-Flame Optimizer [14]	799.072
Black-hole-based optimization [20]	799.921
Ant lion optimizer [31]	799.0133
Modified Sine-Cosine algorithm [32]	799.31

The convergence characteristics of the proposed method and the ALO algorithm are shown in Fig. 1. It can be seen that the SMA algorithm outperforms the ALO algorithm in terms of convergence rate towards the global optimum solution. So, the results achieved showed the SMA superior and robust compared to the ALO algorithm in order to get the best solution to solve the OPF problem.

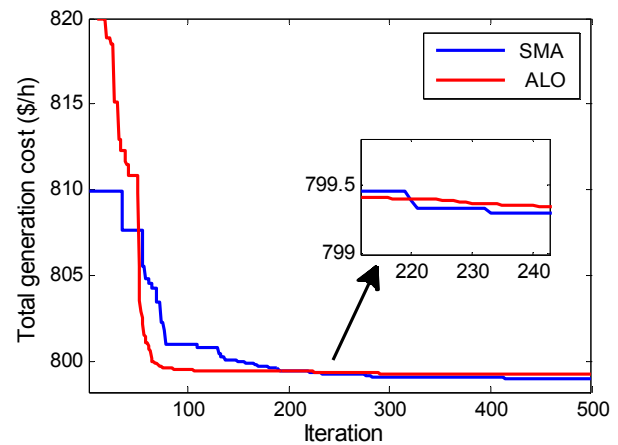


Fig. 1. Convergence characteristics of the SMA & ALO: Case 1

Case 2: Minimization of total fuel cost and wind power cost. In this test case, SMA is applied to solve the OPF problem by incorporating stochastic wind power. Thus, the objective function is minimizing the total generation cost that includes fuel cost and wind power cost. The cumulative cost, described by (13). In this case, the standard IEEE 30-bus system is considered by including two wind farms located at bus numbers 10 and 24. Moreover, the two wind farms (WFs) consist of 30 units of wind turbine generation (WTG) with a nominal power rating of each WTG is 2 MW. Thus, each WF having a total capacity of 30 MW.

Table 2 details the specification of wind turbine characteristics used in all optimization cases in this study concern with incorporating wind power for the IEEE 30-bus system [33].

Table 2

The characteristics of this wind turbine

Parameters	Value
k	2
c	3
d_r	1.3
P_{wr}	2000 kW
v_{cut-in}	4 m/s
v_{rated}	12 m/s
$v_{cut-off}$	25 m/s
$K_{p,j}$ (penalty factor)	1 \$/MWh
$K_{r,j}$ (rserve factor)	4 \$/MWh

Table 3 presents for case 2 the results obtained by SMA to minimize the total generation costs, which are the total fuel and wind costs. The sizing of the two wind farms can be referred to in the same table. For this case, SMA exhibit bus 10 and 24 as the optimal locations of the wind farm. At active power loading of 283.4 MW, It can be seen that the TGC produced by SMA is reduced from 798.9709 \$/h to 725.7113 \$/h. Moreover, the active power losses have also increased from 8.5752 MW to 6.2413 MW which is lowered by 27.21 %. Thus, SMA provides the best values to minimize the TGC and reduce the active power losses in the IEEE 30-bus test system by incorporating wind power compared to the case without the implementation of wind farms. In general, the implementation of wind farm installation to the system has significantly reduced the values of the total generation cost and the active power losses.

Table 3

Best control variable settings obtained via SMA for IEEE 30-bus system including WPG and SVC devices

Control Variables	Limits		Active power loading 283.4 MW			Active power loading 410.93 MW		
	Min	Max	Case 1	Case 2	Case 3	Case 4	Case 5	Case 6
P_{G1} (MW)	50	200	177.5784	139.3865	139.6782	199.9977	195.2207	195.2576
P_{G2} (MW)	20	80	48.6770	39.6216	39.4803	78.8218	57.6992	57.8394
P_{G5} (MW)	15	50	21.2668	18.6332	18.5144	42.4211	32.9495	32.7988
P_{G2} (MW)	10	35	21.2316	10.0000	10.0292	34.9915	34.9999	34.9896
P_{G11} (MW)	10	30	12.0890	10.0000	10.0025	29.9997	21.9266	23.1781
P_{G13} (MW)	12	40	12.0000	12.0000	12.0042	38.2946	20.3897	19.1394
P_{WS1} (MW)	0	40	–	30.0000	30.0000	–	30.0000	30.0000
P_{WS2} (MW)	0	40	–	30.0000	30.0000	–	30.0000	30.0000
V_{G1} (p.u.)	0.95	1.1	1.1000	1.1000	1.1000	1.1000	1.1000	1.1000
V_{G2} (p.u.)	0.9	1.1	1.0879	1.0894	1.0873	1.0843	1.0804	1.0818
V_{G5} (p.u.)	0.9	1.1	1.0618	1.0644	1.0597	1.0286	1.0264	1.0263
V_{G8} (p.u.)	0.9	1.1	1.0701	1.0760	1.0719	1.0616	1.0669	1.0694
V_{G11} (p.u.)	0.9	1.1	1.1000	1.0539	1.0233	1.1000	1.1000	1.0964
V_{G13} (p.u.)	0.9	1.1	1.1000	1.0183	1.0150	1.1000	1.0516	1.0371
T_{11} (p.u.)	0.9	1.1	1.0259	1.0903	1.0989	1.0189	1.0896	1.1000
T_{12} (p.u.)	0.9	1.1	0.9010	1.0286	1.0887	1.0211	1.0991	1.0993
T_{15} (p.u.)	0.9	1.1	0.9803	1.0980	1.0786	1.0511	1.0997	1.0974
T_{36} (p.u.)	0.9	1.1	0.9568	1.0594	1.0429	0.9609	1.0272	1.0455
Q_{C10} (Mvar)	0	5	4.3806	0.0139	1.7150	4.8813	4.1783	3.8886
Q_{C12} (Mvar)	0	5	4.7790	2.8581	0	1.9164	4.8901	0.8560
Q_{C15} (Mvar)	0	5	4.8272	0	4.7098	3.1109	3.1556	1.6088
Q_{C17} (Mvar)	0	5	4.9942	2.2721	1.4631	4.9727	4.9617	5.0000
Q_{C20} (Mvar)	0	5	2.5651	2.7844	1.0131	1.3915	1.1554	4.1684
Q_{C21} (Mvar)	0	5	2.8396	5.0000	4.8532	4.9937	0.0066	4.9944
Q_{C23} (Mvar)	0	5	3.4609	4.8785	0.5928	2.9808	2.7736	4.7325
Q_{C24} (Mvar)	0	5	4.9957	0.2167	1.8172	4.6307	1.3769	0.0423
Q_{C29} (Mvar)	0	5	1.1562	0.9389	0.4900	1.1981	1.2900	4.8493
Q_{WS1} (Mvar)	-15	40	–	-3.9319	39.4803	–	4.7442	57.8394
Q_{WS2} (Mvar)	-15	40	–	3.3754	0.8719	–	10.3240	32.7988
Q_{SVC30} (Mvar)	-25	25	–	–	5.6479	–	–	6.6716
Total generation cost (\$/h)			798.9709	725.7113	725.8855	1339.4776	1198.1826	1198.2092
Power losses (MW)			8.5752	6.2413	6.3087	13.5964	12.2555	12.2729
Voltage deviation (p.u.)			1.4494	0.6285	0.5195	0.7413	0.6066	0.5465
Reserved real power			–	53.5074	53.5074	–	53.5074	53.5074

The convergence curves of the SMA and ALO for case 2 are shown in Fig. 2, which allows us to note, in the first place, that the SMA converges towards the global optimum value at iteration 120 compared to the ALO, that the convergence towards the optimal solution is reached at iteration 270.

Case 3: Minimization of fuel cost and wind power cost by considering the SVC device. In this case study, SMA is applied for solving the OPF problem by incorporating wind power and SVC devices. The optimal location of the SVC device for the IEEE 30-bus system found by SMA is bus N°30. The objective function used is to minimize the TGC as described by (13). From this case, It can be seen that the voltage deviation is reduced from 1.4494 p.u (case 1) and 0.6285 (case 2) to 0.5428 p.u. The voltage profile obtained by the SMA algorithm for cases 2 and 3 is shown in Fig. 3. It is seen that the effect of the SVC device to improve the profile voltage, especially in

the busses far from generators units such as bus N°25 until bus N°30.

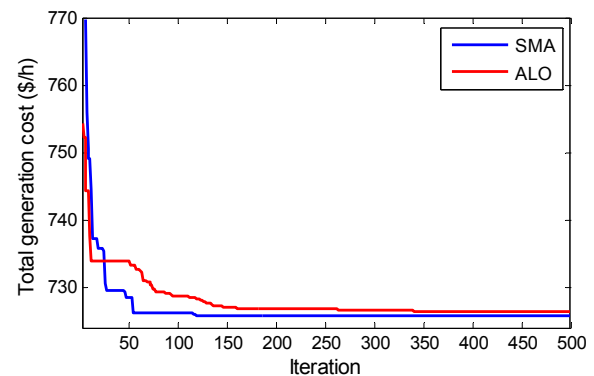


Fig. 2. Convergence characteristics of the SMA & ALO: Case 2

OPF solution under the contingency state. In this part, the SMA is applied to solve the OPF problem under

the contingency state, which is increased loading at 45 %. Thus, the active power loading is 410.93 MW. Three different cases are considered for this part.

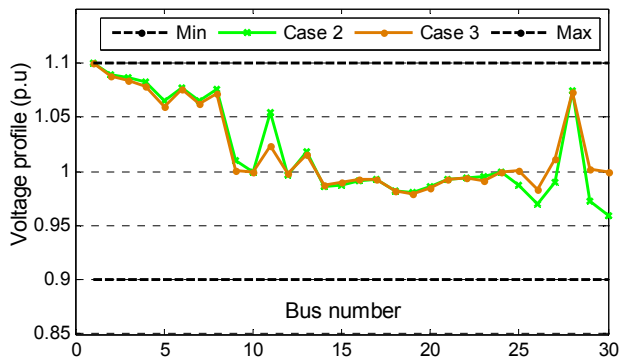


Fig. 3. Profile Voltage magnitudes for case 2 and case 3

Case 4: Minimization of total fuel cost. In this case, the objective function is to optimize the total fuel cost in the IEEE 30-bus system with increased loading at 45 % and is described by (16) addition to the penalty of line power. From the results given by the SMA algorithm for the case N°5, It can be seen that most generators work near their maximum limits, due to the increased load compared to the results given in case 1 without increased load. Moreover, we can also see that the fuel cost, active power losses, and voltage deviation are increased as presented in Table 3. The convergence characteristics of the SMA and ALO for case 4 are shown in Fig. 4.

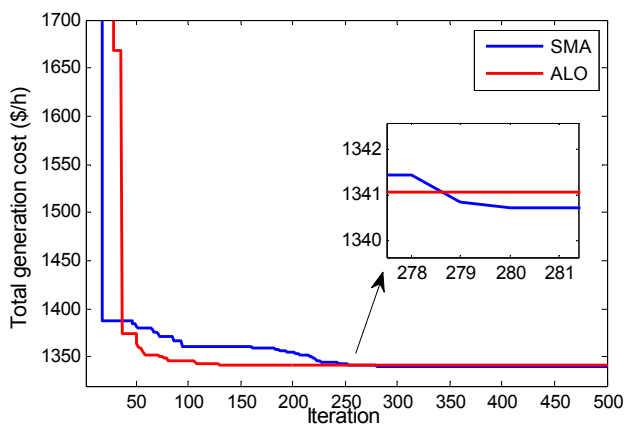


Fig. 4. Convergence characteristics of the SMA & ALO: Case 4

Case 5: Minimization of total fuel cost and wind power cost. The minimization of total fuel cost and wind power cost, in this case, is formulated as the objective function, which is described by (13). At higher active power loading of 410.90 MW, SMA provides 1198.1826 \$/h for the TGC, this value better than a value obtained in a case without incorporating wind power. On the other hand, the implementation of wind farms has reduced the active power losses and the deviation voltage in the system.

The convergence characteristics of the SMA and ALO for case 5 are shown in Fig. 5. From this figure, it demonstrates that the SMA algorithm can converge to the global optimum at iteration 170, while ALO towards the optimal solution is reached at iteration 230.

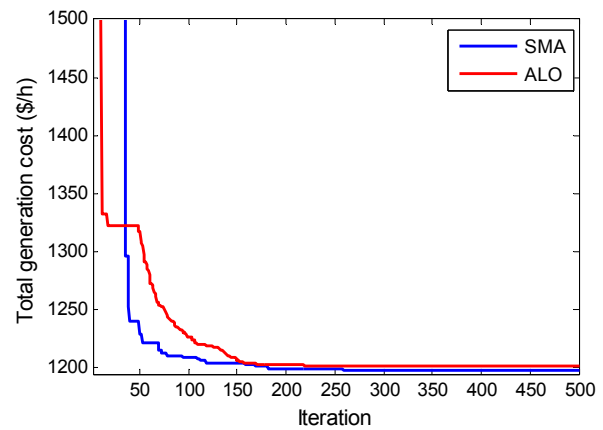


Fig. 5. Convergence characteristics of the SMA & ALO: Case 5

Case 6: Minimization of total fuel cost and wind power cost by considering the SVC device. In this case, we have study the influence of SVC devices on a power system to improve the voltage profile. The voltage profile for case 5 and case 6 are shown in Fig. 6. Unlike case 5 where profile voltage decreases after overloading, adding the SVC to the power system, in this case, improves the voltage as seen in Fig. 6. Through the given results, we note that the effect of SVC is significant in the case of increased load.

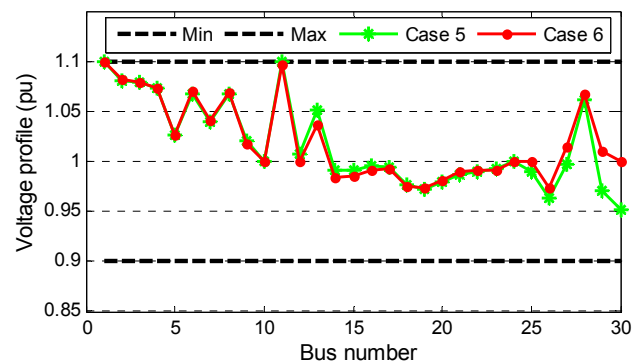


Fig. 6. Profile voltage magnitudes for case 5 and case 6

Algerian electrical network system. In order to verify the performance and efficiency of the ALO to solve nonlinear problems in larger-scale dimensions, OPF is performed on the Algerian electrical network system. This system includes 15 generators, 175 transmission lines, and 16 located from line 160 to line 175. The technical and economic parameters of generator units of the Algerian electrical network system are presented in [34].

Case 7: Minimization of total fuel cost. In this case, SMA is tested to identify the optimal fuel cost on the large-scale Algerian electrical network system with 114 buses. Table 4 presents the optimal settings of control variables reached by SMA with three different cases taking into consideration the vector of control variables contains the active powers generated and the generator voltages. The best value of fuel cost obtained by SMA for the vector of control variables contains the active powers generated is 18914.105 \$/h and better than other methods as well as previously reported methods in Table 5.

The convergence characteristics of the proposed algorithm and ALO algorithm for case 7 are shown in Fig. 7. It can be seen that the SMA algorithm outperforms the ALO algorithm in terms of convergence rate towards the global optimum solution.

Table 4

Best control variable settings obtained via SMA for ALG 114-bus system including WPG and SVC devices

Control Variables	Case 7	Case 8	Case 9	Control Variables	Case 7	Case 8	Case 3
P_{G4} (MW)	451.3078	444.8246	446.5335	V_{G4} (p.u)	1.0997	1.1000	1.0999
P_{G5} (MW)	451.1405	446.1754	443.8411	V_{G5} (p.u)	1.1000	1.1000	1.1000
P_{G11} (MW)	99.9998	99.9992	99.9993	V_{G11} (p.u)	1.0954	1.0990	1.0993
P_{G15} (MW)	193.3981	190.5629	188.6959	V_{G15} (p.u)	1.1000	1.1000	1.0993
P_{G17} (MW)	446.9078	439.3309	441.6877	V_{G17} (p.u)	1.1000	1.1000	1.1000
P_{G19} (MW)	194.8571	190.8661	189.4341	V_{G19} (p.u)	1.0599	1.0523	1.0590
P_{G22} (MW)	191.8038	190.0866	186.7558	V_{G22} (p.u)	1.0620	1.0589	1.0683
P_{G52} (MW)	188.5324	186.9000	185.9111	V_{G52} (p.u)	1.0661	1.0622	1.0668
P_{G80} (MW)	190.4592	184.5212	186.0970	V_{G80} (p.u)	1.1000	1.1000	1.0998
P_{G83} (MW)	187.8661	181.9296	183.6420	V_{G83} (p.u)	1.1000	1.1000	1.1000
P_{G98} (MW)	188.6026	183.2775	184.3464	V_{G98} (p.u)	1.1000	1.1000	1.1000
P_{G100} (MW)	600.0000	599.9998	600.0000	V_{G100} (p.u)	1.1000	1.1000	1.1000
P_{G101} (MW)	200.0000	200.0000	200.0000	V_{G101} (p.u)	1.1000	1.1000	1.1000
P_{G109} (MW)	100.0000	99.9995	99.9985	V_{G109} (p.u)	1.1000	1.1000	1.0998
P_{G111} (MW)	99.9976	100.0000	100.0000	V_{G111} (p.u)	1.0701	1.0650	1.0792
P_{WS1} (MW)	–	15.0000	15.0000	Q_{SVC68} (Mvar)	–	–	22.000
P_{WS2} (MW)	–	30.0000	29.9999	Q_{SVC89} (Mvar)	–	–	32.800
		Case 1		Case 2		Case 3	
Fuel cost (\$/h)		18914.105		18624.9978		18610.7234	
Power losses (MW)		57.8726		56.4733		54.9422	
Voltage deviation (p.u.)		4.9714		4.8197		4.5968	
Reserved real power		–		41.0227		41.0227	

Table 5
Comparison of solutions achieved using SMA and different methods for Case 7

Method	Fuel cost (\$/h)
Slime mould algorithm	18914.105
Differential evolution [34]	19203.340
Grey wolf optimizer [35]	19171.958
Hybrid GA-DE-PS [36]	19199.444
M-objective ant lion algorithm [37]	19355.859

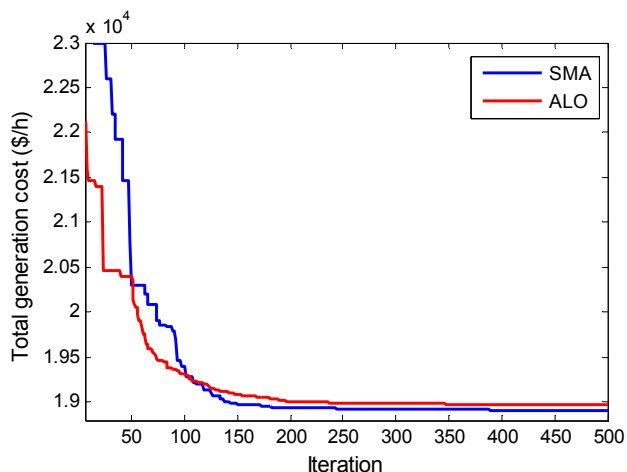


Fig. 7. Convergence characteristics of the SMA & ALO: Case 7

Case 8: Minimization of total fuel cost and wind power cost. In this case, SMA is applied to solve the OPF problem on the large-scale power system by incorporating stochastic wind power. The Algerian power system ALG 114-bus is considered by including two wind generators

Table 5

located at busses 99 (Setif) and 107 (Djelfa). Moreover, the two wind farms (WF) consist of 40 units of wind turbine generation (WTG) are connected to the system at busses 10 and 24 with a nominal power rating of each WTG is 1.5 MW. Weibull settings for the sites that have been chosen are taken from [38]. The choice of the turbine has been set for General Electric GE 1,5-77 machines. The characteristics of this wind turbine are shown in Table 6.

Table 6

The characteristics of this wind turbine

Parameters	Wind turbine1	Wind turbine
k	1.425	2.008
c	4.083	5.178
d_r	1.75	2
P_{wr}	15 MW	30 MW
v_{cut-in}	3.5 m/s	3.5 m/s
v_{rated}	12 m/s	12 m/s
$v_{cut-off}$	25 m/s	25 m/s
$K_{p,i}$ (penalty factor)	1.5 \$/MWh	1.5 \$/MWh
$K_{r,j}$ (reserve factor)	3 \$/MWh	3 \$/MWh

Table 4 summarizes the best results reached by SMA to minimize total generation cost, reduce active power losses and improve the voltage profile by incorporating two wind farms. Based on the results achieved by the SMA in case 7 compared to case 8, the incorporation of wind farms into the system in the ALG 114 system gave more significant profit in TGC and reducing active power losses. The convergence characteristics of the SMA for case 8 are shown in Fig. 8. The convergence of the SMA is reached in the first 170 iterations, while the convergence of the ALO towards the optimal solution is reached at iteration 230.

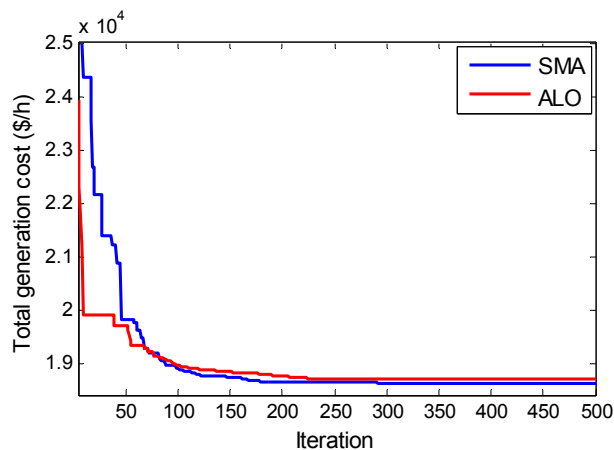


Fig. 8. Convergence characteristics of the SMA & ALO: Case 8

Case 9: Minimization of total fuel cost and wind power cost by considering the SVC device. In order to illustrate the effectiveness of the SMA in presence of SVC devices on the power system, the ALG 114-bus is considered by including two SVC devices at busses N°68 (Sedjerara) and bus N°89 (Souk Ahras). These locations of SVC devices are considered the optimal placement in the Algerian 114-bus system found by the SMA algorithm. After the results of the simulation, the installation of the SVC improved considerably the total generation cost, the active power loss. Figure 9 represents that the effect of SVC devices is significant in the Algerian 114-bus system to maintain the voltages within the acceptable limits.

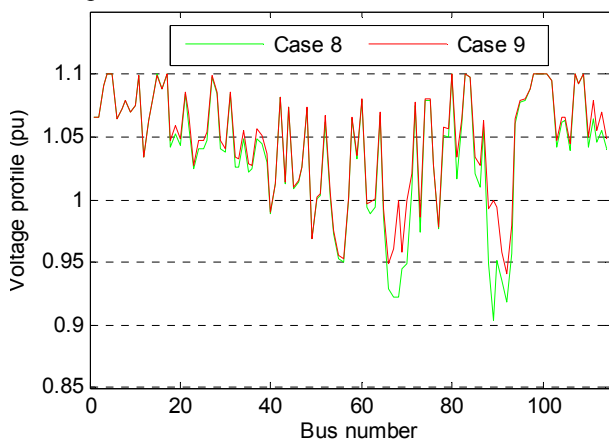


Fig. 9. Profile voltage magnitudes for case 8 and case 9

Conclusion. This paper proposed a recent metaheuristic technique called a slime mould algorithm to solve the optimal power flow problem incorporating stochastic wind power and static VAR compensator devices. In this study, nine cases have been considered and examined via the proposed algorithm on the IEEE 30-bus system and practical Algerian power system ALG 114-bus. The objective function solved is a minimization of the total generation cost that includes fuel cost and wind power cost. Also, the nature of the wind output function used is based on the Weibull probability distribution model. For the case without considering wind power and static VAR compensator devices, it is worth mentioning that the proposed algorithm is capable of achieving and getting the best global optimal solution for

both of the testing systems compared to the other methods in the literature mentioned in this paper. With considering wind power and SVC devices, the numerical results obtained show a better performance of the proposed algorithm to solve the optimal power flow problem compared to the ant lion optimizer algorithm. Additionally, incorporating the wind power and static VAR compensator device has a high influence on the power system through minimize the total generation cost, reduce the active power loss as well as improve the voltage profile. Thus, the results obtained prove the merits and efficiency of the proposed algorithm to solve the stochastic optimal power flow problem.

REFERENCES

1. Bhatia S.C. Energy resources and their utilization. *Advanced Renewable Energy Systems*, pp. 1–31, 2014. doi: [10.1016/B978-1-78242-269-3.50001-2](https://doi.org/10.1016/B978-1-78242-269-3.50001-2).
2. Talari S., Shafie-khah M., Osório G.J., Aghaei J., Catalão J.P.S. Stochastic modelling of renewable energy sources from operators' point-of-view: A survey. *Renewable and Sustainable Energy Reviews*, 2018, vol. 81, part 2, pp. 1953-1965. doi: [10.1016/j.rser.2017.06.006](https://doi.org/10.1016/j.rser.2017.06.006).
3. Roy R., Jadhav H.T. Optimal power flow solution of power system incorporating stochastic wind power using Gbest guided artificial bee colony algorithm. *International Journal of Electrical Power & Energy Systems*, 2015, vol. 64, pp. 562-578. doi: [10.1016/j.ijepes.2014.07.010](https://doi.org/10.1016/j.ijepes.2014.07.010).
4. Elattar E.E. Optimal Power Flow of a Power System Incorporating Stochastic Wind Power Based on Modified Moth Swarm Algorithm. *IEEE Access*, 2019, vol. 7, pp. 89581-89593. doi: [10.1109/ACCESS.2019.2927193](https://doi.org/10.1109/ACCESS.2019.2927193).
5. Biswas P.P., Suganthan P.N., Amaratunga G.A.J. Optimal power flow solutions incorporating stochastic wind and solar power. *Energy Conversion and Management*, 2017, vol. 148, pp. 1194-1207. doi: [10.1016/j.enconman.2017.06.071](https://doi.org/10.1016/j.enconman.2017.06.071).
6. Panda A., Tripathy M. Security constrained optimal power flow solution of wind-thermal generation system using modified bacteria foraging algorithm. *Energy*, 2015, vol. 93, pp. 816-827. doi: [10.1016/j.energy.2015.09.083](https://doi.org/10.1016/j.energy.2015.09.083).
7. Ahmad M., Javaid N., Niaz I.A., Shafiq S., Rehman O.U., Hussain H.M. Application of bird swarm algorithm for solution of optimal power flow problems. *12-th International Conference on Complex, Intelligent, and Software Intensive Systems (CISIS-2018). Advances in Intelligent Systems and Computing*, vol 772, pp. 280-291. Springer, Cham. doi: [10.1007/978-3-319-93659-8_25](https://doi.org/10.1007/978-3-319-93659-8_25).
8. Duman S., Li J., Wu L., Guvenc U. Optimal power flow with stochastic wind power and FACTS devices: a modified hybrid PSO-GSA with chaotic maps approach. *Neural Computing and Applications*, 2019, vol. 32, no. 12, pp. 8463-8492. doi: [10.1007/s00521-019-04338-y](https://doi.org/10.1007/s00521-019-04338-y).
9. El-Fergany A.A., Hasanien H.M. Salp swarm optimizer to solve optimal power flow comprising voltage stability analysis. *Neural Computing and Applications*, 2019, vol. 32, no. 9, pp. 5267-5283. doi: [10.1007/s00521-019-04029-8](https://doi.org/10.1007/s00521-019-04029-8).
10. Mohamed A.-A.A., Mohamed Y.S., El-Gaafary A.A., Hemeida A.M. Optimal power flow using moth swarm algorithm. *Electric Power Systems Research*, 2017, vol. 142, pp. 190-206. doi: [10.1016/j.epsr.2016.09.025](https://doi.org/10.1016/j.epsr.2016.09.025).
11. Biswas P.P., Suganthan P.N., Mallipeddi R., Amaratunga G.A.J. Optimal power flow solutions using differential evolution algorithm integrated with effective constraint handling techniques. *Engineering Applications of Artificial Intelligence*, 2018, vol. 68, pp. 81-100. doi: [10.1016/j.engappai.2017.10.019](https://doi.org/10.1016/j.engappai.2017.10.019).
12. Surender Reddy S., Srinivasa Rathnam C. Optimal Power Flow using Glowworm Swarm Optimization. *International Journal of Electrical Power & Energy Systems*, 2016, vol. 80, pp. 128-139. doi: [10.1016/j.ijepes.2016.01.036](https://doi.org/10.1016/j.ijepes.2016.01.036).

13. Abaci K., Yamacli V. Differential search algorithm for solving multi-objective optimal power flow problem. *International Journal of Electrical Power & Energy Systems*, 2016, vol. 79, pp. 1-10. doi: **10.1016/j.ijepes.2015.12.021**.
14. Trivedi I.N., Jangir P., Parmar S.A., Jangir N. Optimal power flow with voltage stability improvement and loss reduction in power system using Moth-Flame Optimizer. *Neural Computing and Applications*, 2016, vol. 30, no. 6, pp. 1889-1904. doi: **10.1007/s00521-016-2794-6**.
15. Pulluri H., Naresh R., Sharma V. A solution network based on stud krill herd algorithm for optimal power flow problems. *Soft Computing*, 2016, vol. 22, no. 1, pp. 159-176. doi: **10.1007/s00500-016-2319-3**.
16. Jadon S.S., Bansal J.C., Tiwari R., Sharma H. Artificial bee colony algorithm with global and local neighborhoods. *International Journal of System Assurance Engineering and Management*, 2014, vol. 9, no. 3, pp. 589-601. doi: **10.1007/s13198-014-0286-6**.
17. Duman S. Symbiotic organisms search algorithm for optimal power flow problem based on valve-point effect and prohibited zones. *Neural Computing and Applications*, 2016, vol. 28, no. 11, pp. 3571-3585. doi: **10.1007/s00521-016-2265-0**.
18. Bouchekara H.R.E.H., Chaib A.E., Abido M.A., El-Sehiemy R.A. Optimal power flow using an Improved Colliding Bodies Optimization algorithm. *Applied Soft Computing*, 2016, vol. 42, pp. 119-131. doi: **10.1016/j.asoc.2016.01.041**.
19. Hariharan T., Sundaram K.M. Optimal Power Flow Using Firefly Algorithm with Unified Power Flow Controller. *Circuits and Systems*, 2016, vol. 07, no. 08, pp. 1934-1942. doi: **10.4236/cs.2016.78168**.
20. Bouchekara H.R.E.H. Optimal power flow using black-hole-based optimization approach. *Applied Soft Computing*, 2014, vol. 24, pp. 879-888. doi: **10.1016/j.asoc.2014.08.056**.
21. Bouchekara H.R.E.H., Abido M.A., Chaib A.E., Mehasni R. Optimal power flow using the league championship algorithm: A case study of the Algerian power system. *Energy Conversion and Management*, 2014, vol. 87, pp. 58-70. doi: **10.1016/j.enconman.2014.06.088**.
22. Mohan T.M., Nireekshana T. A Genetic algorithm for solving optimal power flow problem. *Proceedings 2019 3rd International conference on Electronics, Communication and Aerospace Technology (ICECA)*, 2019, pp. 1438-1440. doi: **10.1109/ICECA.2019.8822090**.
23. Bentouati B., Chettih S., Jangir P., Trivedi I.N. A solution to the optimal power flow using multi-verse optimizer. *Journal of Electrical Systems*, 2016, vol. 12, no. 4, pp. 716-733.
24. Ren P., Li N. Optimal power flow solution using the Harmony search algorithm. *Applied Mechanics and Materials*, 2014, vol. 599-601, pp. 1938-1941. doi: **10.4028/www.scientific.net/AMM.599-601.1938**.
25. Ghosh I., Roy P.K. Application of earthworm optimization algorithm for solution of optimal power flow. *2019 International Conference on Opto-Electronics and Applied Optics (Optronix)*, 2019, vol. 1, no. 1, pp. 1-6. doi: **10.1109/OPTRONIX.2019.8862335**.
26. Hetzer J., Yu D.C., Bhattarai K. An Economic Dispatch Model Incorporating Wind Power. *IEEE Transactions on Energy Conversion*, 2008, vol. 23, no. 2, pp. 603-611. doi: **10.1109/tec.2007.914171**.
27. Makhloufi S., Mekhaldi A., Tegar M. Three powerful nature-inspired algorithms to optimize power flow in Algeria's Adrar power system. *Energy*, 2016, vol. 116, pp. 1117-1130. doi: **10.1016/j.energy.2016.10.064**.
28. Panda A., Tripathy M. Optimal power flow solution of wind integrated power system using modified bacteria foraging algorithm. *International Journal of Electrical Power & Energy Systems*, 2014, vol. 54, pp. 306-314. doi: **10.1016/j.ijepes.2013.07.018**.
29. Teeparthi K., Vinod Kumar D.M. Multi-objective hybrid PSO-APO algorithm based security constrained optimal power flow with wind and thermal generators. *Engineering Science and Technology, an International Journal*, 2017, vol. 20, no. 2, pp. 411-426. doi: **10.1016/j.jestech.2017.03.002**.
30. Li S., Chen H., Wang M., Heidari A.A., Mirjalili S. Slime mould algorithm: A new method for stochastic optimization. *Future Generation Computer Systems*, 2020, vol. 111, pp. 300-323. doi: **10.1016/j.future.2020.03.055**.
31. Kouadri R., Slimani L., Bouktir T., Musirin I. Optimal Power Flow Solution for Wind Integrated Power in presence of VSC-HVDC Using Ant Lion Optimization. *Indonesian Journal of Electrical Engineering and Computer Science*, 2018, vol. 12, no. 2, p. 625. doi: **10.11591/ijeecs.v12.i2.pp625-633**.
32. Attia A.-F., El Sehiemy R.A., Hasanien H.M. Optimal power flow solution in power systems using a novel Sine-Cosine algorithm. *International Journal of Electrical Power & Energy Systems*, 2018, vol. 99, pp. 331-343. doi: **10.1016/j.ijepes.2018.01.024**.
33. Haddi S., Bouketir O., Bouktir T. Improved Optimal Power Flow for a Power System Incorporating Wind Power Generation by Using Grey Wolf Optimizer Algorithm. *Advances in Electrical and Electronic Engineering*, 2018, vol. 16, no. 4, pp. 471-488. doi: **10.15598/aeec.v16i4.2883**.
34. Slimani L., Bouktir T. Optimal Power Flow Solution of the Algerian Electrical Network using Differential Evolution Algorithm. *TELKOMNIKA (Telecommunication Computing Electronics and Control)*, 2012, vol. 10, no. 2, p. 199. doi: **10.12928/telkomnika.v10i2.778**.
35. Kouadri R., Musirin I., Slimani L., Bouktir T. OPF for large scale power system using ant lion optimization: a case study of the Algerian electrical network. *IAES International Journal of Artificial Intelligence (IJ-AI)*, 2020, vol. 9, no. 2, p. 252. doi: **10.11591/ijai.v9.i2.pp252-260**.
36. Mahdad B., Srairi K. Solving practical economic dispatch using hybrid GA-DE-PS method. *International Journal of System Assurance Engineering and Management*, 2013, vol. 5, no. 3, pp. 391-398. doi: **10.1007/s13198-013-0180-7**.
37. Herbadji O., Slimani L., Bouktir T. Optimal power flow with four conflicting objective functions using multiobjective ant lion algorithm: A case study of the algerian electrical network. *Iranian Journal of Electrical and Electronic Engineering*, 2019, vol. 15, no. 1, pp. 94-113. doi: **10.22068/IJEEE.15.1.94**.
38. Derai A., Diaf A.K.S. Etude de faisabilité technico-économique de fermes éoliennes en Algérie. *Rev. des Energies Renouvelables*, 2017, vol. 20, no. 4, pp. 693-712. (Fra).

Received 11.08.2020

Accepted 02.11.2020

Published 24.12.2020

Ramzi Kouadri¹, Ph.D Student,
Linda Slimani¹, Professor,
Tarek Bouktir¹, Professor,
¹Department of Electrical Engineering,
University of Ferhat Abbas Setif 1,
19000, Setif, Algeria.
e-mail: ramzikouadri@univ-setif.dz,
slimanibinda@gmail.com,
bouktir@univ-setif.dz

How to cite this article:

Kouadri R., Slimani L., Bouktir T. Slime mould algorithm for practical optimal power flow solutions incorporating stochastic wind power and static VAR compensator device. *Electrical engineering & electromechanics*, 2020, no. 6, pp. 45-54. doi: **10.20998/2074-272X.2020.6.07**.

A.V. Krasnozhon, R.O. Buinyi, I.V. Dihtyaruk, A.O. Kvytsynskyi

THE INVESTIGATION OF DISTRIBUTION OF THE MAGNETIC FLUX DENSITY OF OPERATING TWO-CIRCUIT POWER LINE 110 kV «CHTPP-CHERNIHIV-330» IN THE RESIDENTIAL AREA AND METHODS OF ITS DECREASING TO A SAFE LEVEL

Purpose. The problem of evaluation and analysis of magnetic flux density of overhead power lines is very relevant now, since the magnetic field of industrial frequency can have a negative effect on human health. The analysis of the magnetic field of the operating double-circuit overhead transmission line was made in this work. This overhead line is in the residential area of Chernihiv, Ukraine. The purpose of this work is to determine safe habitation conditions as a function of the magnetic flux density along the route of two-circuit power line with the voltage 110 kV «ChTPP-Chernihiv-330». Real modes of operation are taken into account. Recommendations are given for reducing the magnetic flux density level in the residential area to a value that will not exceed the standard value. *Methodology.* Methods of electromagnetic field theory were used to calculate the magnetic field of power lines. The location of the phase wires on different types of supports of the existing power transmission line and the minimum distance between the conductors and the ground were taken into account. The current value of the current in the phases of the transmission line was taken from the Company «Chernihivoblenergo». Also, the calculation of the magnetic flux density was made for the perspective loads of the transmission line. Estimation of the value of the magnetic flux density was made for the zone of one-story and multi-story buildings near power lines. The option of uniform loading of two power transmission lines was considered and the case where the entire load is transferred along one circuit was also considered. *Results.* In this work, the distribution of magnetic flux density at a height of 1.8 m in the direction perpendicular to the power transmission line for the sections built on supports of the U110-2 and PB110-2 types was obtained. The graphs show that the magnitude of the magnetic flux density at the boundary of the protection zone of the transmission line will be exceed twice the standard value 0.5 μT for the existing and perspective loads. This problem is relevant in the case of transmission lines in single-circuit mode. The graphs of distribution of magnetic flux density on the facade of an apartment building, located at a distance of 20 m from the axis of symmetry of the transmission line, were constructed. As a result, it is shown that at a height of 11 m from the earth's surface, magnetic flux density will be 1.5-2 μT . *Practical value.* It is determined that safe habitation along the route of two-circuit power line with the voltage 110 kV «ChTPP-Chernihiv-330» can be achieved when facades of an apartment building are removed from the axis of symmetry of the transmission line at a distance of 33 m for high-rise buildings and at a distance of 27 m for one-storey buildings. Recommendations for reducing the magnetic flux density of this power transmission line have been developed. References 16, figures 19.

Key words: overhead transmission line, electric loads, magnetic flux density, residential building.

За існуючих та перспективних електричних навантажень досліджено рівень магнітного поля двоколової повітряної ЛЕП напругою 110 кВ «ЧТЕЦ – Чернігівська-330», яка проходить по території одноповерхової та багатоповерхової забудови у м. Чернігів. Показано, що індукція магнітного поля в зоні забудови та на межі охоронної зони може перевищувати безпечний для людини рівень, особливо у випадку роботи ЛЕП у одноколовому режимі. Визначено безпечні умови для проживання населення поблизу даної ЛЕП, зокрема, безпечну відстань від осі траси ЛЕП до місць розташування одноповерхових та багатоповерхових будинків. Показано, що застосування векторної компенсації дозволяє досягти значного зменшення рівня магнітного поля. Бібл. 16, рис. 19.

Ключові слова: повітряна ЛЕП, електричні навантаження, індукція магнітного поля, житлова забудова.

При существующих и перспективных электрических нагрузках исследовано уровень магнитного поля двухцепной воздушной ЛЭП напряжением 110 кВ «ЧТЕЦ – Черниговская-330», которая проходит по территории одноэтажной и многоэтажной застройки в г. Чернигов. Показано, что индукция магнитного поля в зоне застройки и на границе охранный зоны может превышать безопасный для человека уровень, особенно в случае работы ЛЭП в одноцепном режиме. Определены безопасные условия для проживания населения вблизи данной ЛЭП, в частности, безопасное расстояние от оси трассы ЛЭП до мест размещения одноэтажных и многоэтажных домов. Показано, что применение векторной компенсации позволяет достичь значительного уменьшения уровня магнитного поля. Библ. 16, рис. 19.

Ключевые слова: воздушная ЛЭП, электрические нагрузки, индукция магнитного поля, жилая застройка.

Introduction. Recently, more and more attention is paid to the impact of magnetic fields on humans. One of the powerful sources of magnetic field of power frequency is overhead power lines, near which can be located residential buildings or offices. People who permanently live or work near power lines are in the area of the magnetic field influence. In developed countries, such as the United States, Canada, France, Sweden and others there are rather strict restrictions on the level of magnetic flux density of power frequency, it is constantly monitored in buildings and outdoors near overhead and cable power lines, on the territory of substations and outside them. There are a number of medical studies that show that the magnetic field acts on living organisms at

the cellular level, and it is noted that prolonged exposure to even a weak magnetic field over time leads to a variety of health problems [1]. Thus, according to the recommendations of the World Health Organization, the level of magnetic flux density of 0.2-0.4 μT is acceptable for long-term exposure to the population.

Much attention is paid around the world to the problem of reducing the level of the magnetic field [2, 3] to minimize its impact on the environment. It should be noted that in Ukraine the problem of normalization of the magnetic field level has not been finally resolved since Electrical Installation Regulations [4] contains a norm only for the magnetic field of cable lines, which is 0.5 μT

© A.V. Krasnozhon, R.O. Buinyi, I.V. Dihtyaruk, A.O. Kvytsynskyi

inside the premises. In [5], the problem of calculating the induced losses in overhead power lines is considered and it is shown that the reduction of the magnetic field also leads to an increase in the efficiency of electric energy transmission.

The problem of reducing the magnetic field becomes especially relevant in the conditions of increasing electric loads. In large cities, new neighborhoods are constantly being built, entire neighborhoods and residential complexes with multi-storey and single-storey buildings are being built, with appropriate infrastructure – shopping and entertainment complexes, commercial and communal enterprises, industrial enterprises, etc. As a result, the load on existing overhead power lines, which supply power to such cities and individual areas, is increasing. For example, in the city of Chernihiv in the last 15 years there is an active construction of new residential areas, such as Masany and N. Podusivka. These areas are supplied through substations connected to the existing 110 kV overhead transmission line «Ch TPP – Chernihiv-330», respectively, the load of this line has increased significantly in recent years and will continue to grow in the future. The above transmission line passes through the residential area which includes multi-storey and single-storey buildings. Therefore, there is a need to determine the safe living conditions of the population of the city of Chernihiv in the area adjacent to the specified transmission line, as well as, if necessary, the choice of methods to reduce the magnetic field to a safe level.

It should be noted that the problem of studying the magnetic field of overhead power lines [6, 7], as well as methods for reducing it, is being actively studied in Ukraine and around the world. For example, in [8, 9] the distribution of magnetic flux density of transmission lines in residential areas in the general case is considered and analyzed. It should be noted that a similar analysis should also be performed for a specific transmission line, taking into account the conditions of its operation, current and future loads, operating modes, distance of residential buildings from the transmission line route and the protection zone boundaries, features of construction in a residential area near transmission line (one-storey, multi-storey), etc.

In order to comply with the conditions of safe living of the population near overhead power lines, it is necessary to assess the distance from the route of the power line, on which one-storey and multi-storey buildings should be located. However, such measures are appropriate at the stage of designing new overhead power lines or when planning the construction of vacant land plots near power lines. But, in cities there is often a situation where the overhead power line already passes in the immediate vicinity of residential buildings, which can be located even in the protection zone of the power line. In this case, with a significant load of the transmission line, it is necessary to apply techniques of reducing the level of the magnetic field in the residential area.

There are a number of methods for reducing the level of the magnetic field of overhead power lines, which are considered in [10, 11]. Among those that can be applied to existing transmission lines, we should highlight

the shielding and optimization of the geometry of the suspension of conductors (vector compensation method). The latter method can be quite effective, as noted in [10].

In the case of a two-circuit overhead transmission line, the location of the phases of different circuits on the support is usually chosen to be the same in accordance with Fig. 1.

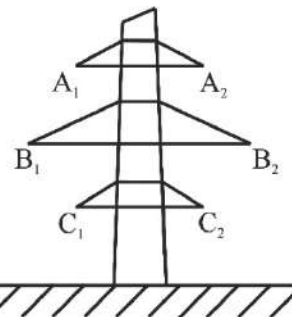


Fig. 1. Typical arrangement of phases of two circuits on the support of the two-circuit overhead transmission line

This phase arrangement option provides the highest level of magnetic field in the space around the transmission line. The most effective in terms of reducing the level of the magnetic field is the location of the phases of the two circuits in mirror symmetry [10], as shown in Fig. 2.

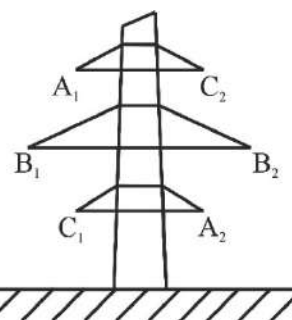


Fig. 2. Mirror arrangement of the phases of two circuits on the support of the two-circuit overhead transmission line

This method of reducing the level of the magnetic field of a two-circuit transmission line is quite easy to be implemented in practice, however, its efficiency for each transmission line may be different depending on the geometry of a particular line.

The goal of the paper is to determine the conditions for safe living of the population at the level of the magnetic field along the route of the two-circuit 110 kV transmission line «Ch TPP – Chernihiv-330» taking into account the real modes of its operation and to develop recommendations to reduce the magnetic field of this transmission line to the regulatory level.

The main materials of the study. The calculation of the electric and magnetic fields of overhead and cable transmission lines was performed in accordance with the method [12], which was substantiated in [13].

According to the method [12], for some calculation point $P(x_p, y_p)$ the effective values of the components or spatial components of the magnetic flux density induction vector from the current in each of the phase conductors of the transmission line should be determined by the formulas:

$$B_{xA} = \frac{\mu_0}{2\pi} \cdot \sum_{k=1}^2 \frac{I_k \cdot (y_p - y_{Ak})}{(x_p - x_{Ak})^2 + (y_p - y_{Ak})^2}; \quad (1)$$

$$B_{xB} = \frac{\mu_0}{2\pi} \cdot \sum_{k=1}^2 \frac{I_k \cdot (y_p - y_{Bk})}{(x_p - x_{Bk})^2 + (y_p - y_{Bk})^2}; \quad (2)$$

$$B_{xC} = \frac{\mu_0}{2\pi} \cdot \sum_{k=1}^2 \frac{I_k \cdot (y_p - y_{Ck})}{(x_p - x_{Ck})^2 + (y_p - y_{Ck})^2}; \quad (3)$$

$$B_{yA} = \frac{\mu_0}{2\pi} \cdot \sum_{k=1}^2 \frac{I_k \cdot (x_p - x_{Ak})}{(x_p - x_{Ak})^2 + (y_p - y_{Ak})^2}; \quad (4)$$

$$B_{yB} = \frac{\mu_0}{2\pi} \cdot \sum_{k=1}^2 \frac{I_k \cdot (x_p - x_{Bk})}{(x_p - x_{Bk})^2 + (y_p - y_{Bk})^2}; \quad (5)$$

$$B_{yC} = \frac{\mu_0}{2\pi} \cdot \sum_{k=1}^2 \frac{I_k \cdot (x_p - x_{Ck})}{(x_p - x_{Ck})^2 + (y_p - y_{Ck})^2}; \quad (6)$$

where I_k is the current in the phase of the k -th circuit of the transmission line, A; x_{Ak}, y_{Ak} are the coordinates of the location of phase A of the k -th circuit of the transmission line; x_{Bk}, y_{Bk} are the coordinates of the location of phase B of the k -th circuit of the transmission line; x_{Ck}, y_{Ck} are the coordinates of the location of the phase C of the k -th circuit of the transmission line; μ_0 is the magnetic permeability of vacuum ($4\pi \cdot 10^{-7}$ H/m).

Also in formulas (1)-(6) it is taken into account that the transmission line to be considered is two-circuit.

The effective value of the components or spatial components of the vector of magnetic flux density at the calculation point is found by the expressions:

$$B_x(x_p, y_p) = [B_{xA}^2 + B_{xB}^2 + B_{xC}^2 - B_{xA} \cdot B_{xB} - B_{xB} \cdot B_{xC} - B_{xC} \cdot B_{xA}]^{0.5} \quad (7)$$

$$B_y(x_p, y_p) = [B_{yA}^2 + B_{yB}^2 + B_{yC}^2 - B_{yA} \cdot B_{yB} - B_{yB} \cdot B_{yC} - B_{yC} \cdot B_{yA}]^{0.5} \quad (8)$$

The effective value of the magnetic flux density at the calculation point is found from the expression:

$$B(x_p, y_p) = \sqrt{B_x(x_p, y_p)^2 + B_y(x_p, y_p)^2}. \quad (9)$$

Overhead power lines often pass through areas with dense multi-storey and single-storey buildings, especially in large cities, including the city of Chernihiv. One such example is a two-circuit 110 kV transmission line «ChTPP – Chernihiv-330», the structural diagram of which is shown in Fig. 3.

Some sections of this transmission line in dense residential areas are made on supports type U110-2 and PB110-2. The dimension of this overhead transmission line according to its support scheme is 7.3 m (minimum distance from the lower wire of the transmission line to the ground). All the geometric dimensions necessary for the calculation of the magnetic field of the transmission line are shown in Fig. 4, 5 for sections on supports U110-2 and PB110-2, respectively.

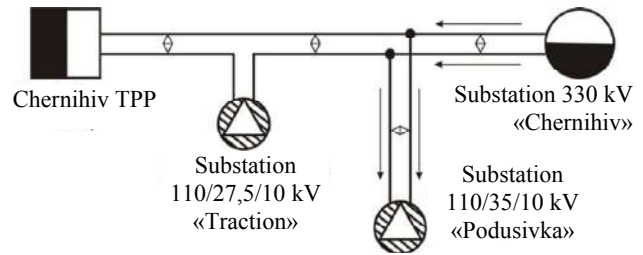


Fig. 3. Structural diagram of the electric network with 110 kV overhead transmission line «ChTPP – Chernihiv-330»

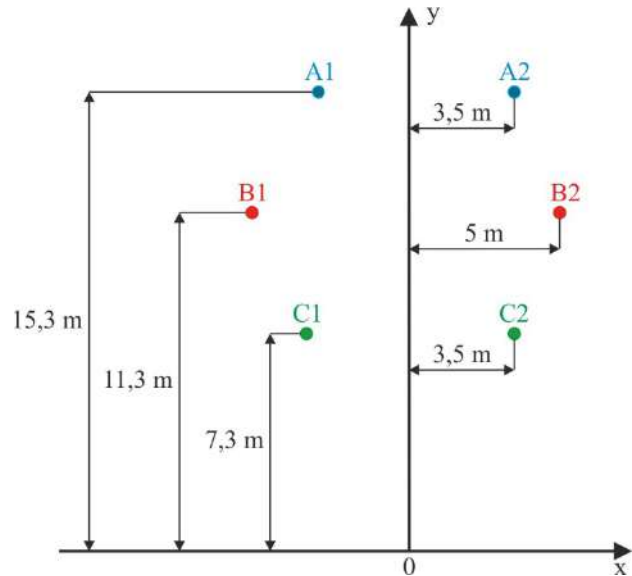


Fig. 4. Geometric model of the section of the 110 kV transmission line «ChTPP – Chernihiv-330» on U110-2 supports

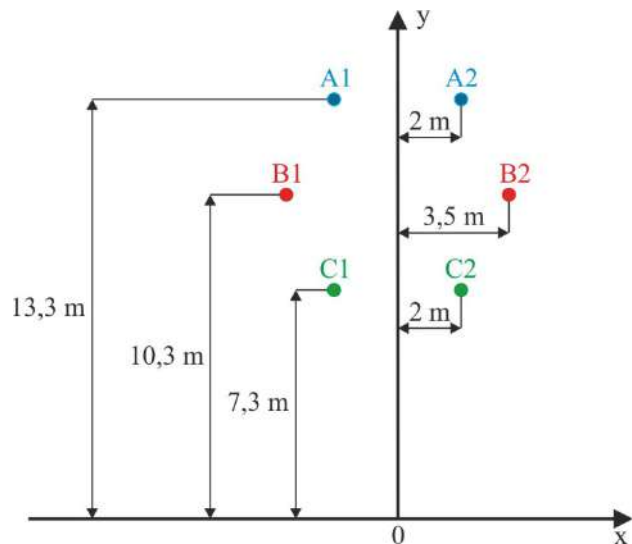
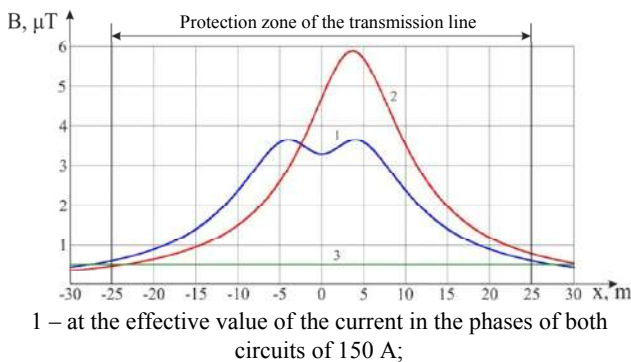


Fig. 5. Geometric model of the section of the 110 kV transmission line «ChTPP – Chernihiv-330» on PB110-2 supports

The calculation of the magnetic field level for the section of the above-mentioned transmission line, made on the supports U110-2, is performed at the level of 1.8 m from the ground surface in the direction perpendicular to the route of the transmission line. According to the data of JSC «Chernihivoblenergo» on electrical loads, the calculation maximum current of one circuit of the 110 kV overhead transmission is about 150 A, which may change

insignificantly during the day. In case of repair or emergency shutdown of one circuit, the second circuit will take over the entire load – about 300 A.

The results of the calculation of the distribution of the magnetic flux density of the transmission line along the coordinate «x» are shown in Fig. 6. It is obvious that at the boundary of the protection zone of the transmission line (at $x = \pm 25$ m) the magnetic flux density practically corresponds to the normative value of $0.5 \mu\text{T}$ under the current value of 150 A in the phases of both circuits. However, if one circuit is switched off, the magnetic flux density on the boundary of the protection zone on the right side of the transmission line (on the operating circuit side) is $0.77 \mu\text{T}$, and the point with safe magnetic flux density value is at a distance of 30 m from the transmission line axis. It should also be noted that some private houses, in particular, two-storey, are located almost below the extreme phases of this transmission line. In this case, the normative value of magnetic flux density will be exceeded several times.



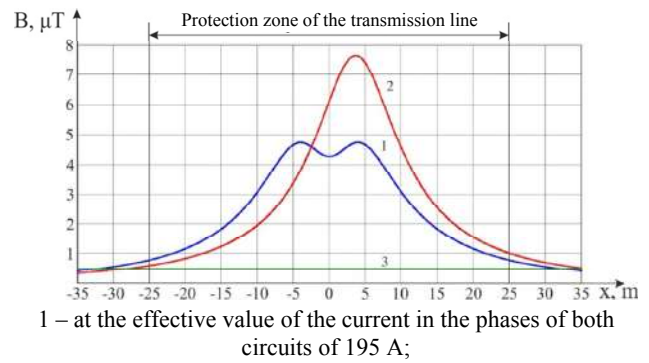
1 – at the effective value of the current in the phases of both circuits of 150 A;
2 – at disconnection of one circuit (effective value of the current of the second circuit is 300 A);
3 – line of the normative level of magnetic flux density of $0.5 \mu\text{T}$

Fig. 6. Distribution of the magnetic flux density of the 110 kV overhead transmission line «ChTTP – Chernihiv-330» at the level of 1.8 m from the earth's surface along the «x» coordinate for the section made on the U110-2 type supports

According to the predicted level of load growth for 10 years [14], the current in the section of this two-circuit transmission line can increase to 195 A for each circuit. The results of the calculation for this case are shown in Fig. 7.

The curves in Fig. 7 indicate an even higher level of magnetic flux density with a promising increase in electric loads. For example, with a uniform load of both circuits, the magnetic flux density at the boundary of the protection zone can reach $0.77 \mu\text{T}$, and when disconnecting one circuit is even equal to $1.0 \mu\text{T}$, the safe value of the magnetic flux density corresponds to the distance from the axis of 32 m and 35 m, respectively, i.e. beyond the protection zones.

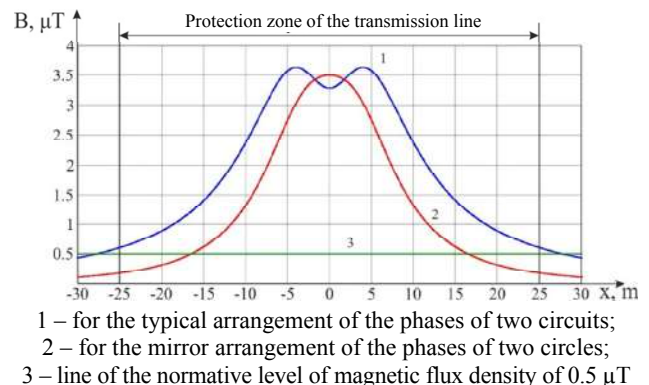
From the above we can conclude that it is necessary to limit the time of single-circuit mode of operation of this transmission line, as it is characterized by a significantly increased level of the magnetic field from the circuit that operates.



1 – at the effective value of the current in the phases of both circuits of 195 A;
2 – at disconnection of one circuit (effective value of the current of the second circuit is 390 A);
3 – line of the normative level of magnetic flux density of $0.5 \mu\text{T}$

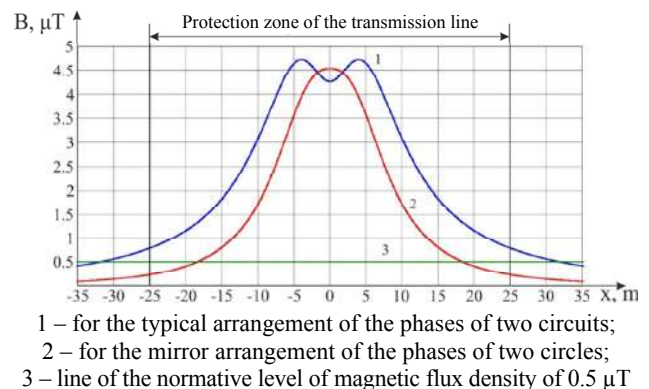
Fig. 7. Distribution of the magnetic flux density of the 110 kV overhead transmission line «ChTTP – Chernihiv-330» for the section made on the U110-2 type supports at the predicted increase in electrical loads

As mentioned above, one of the options to reduce the magnetic flux density of the transmission line may be the use of vector compensation due to the mirror arrangement of the phases of two circuits, the results of the corresponding calculations are shown in Fig. 8, 9 (compared to the traditional arrangement of phases).



1 – for the typical arrangement of the phases of two circuits;
2 – for the mirror arrangement of the phases of two circles;
3 – line of the normative level of magnetic flux density of $0.5 \mu\text{T}$

Fig. 8. Distribution of the magnetic flux density of the 110 kV overhead transmission line «ChTTP – Chernihiv-330» at the level of 1.8 m from the earth's surface along the «x» coordinate for the section made on supports type U110-2, with typical and the mirror arrangement of the phases of the circuits (effective value of the current in the phases of both circuits is 150 A)



1 – for the typical arrangement of the phases of two circuits;
2 – for the mirror arrangement of the phases of two circles;
3 – line of the normative level of magnetic flux density of $0.5 \mu\text{T}$

Fig. 9. Distribution of the magnetic flux density of the 110 kV overhead transmission line «ChTTP – Chernihiv-330» at the level of 1.8 m from the earth's surface along the «x» coordinate for the section made on supports type U110-2, with typical and the mirror arrangement of the phases of the circuits (effective value of the current in the phases of both circuits is 195 A)

It is obvious that the safe value of magnetic flux density of $0.5 \mu\text{T}$ at the mirror arrangement of the phases of two circuits and the phase current of one circuit of 150 A is achieved at a distance of 16.5 m from the centerline of the transmission line, i.e. within its protection zone.

Thus, even with the predicted increase in electrical loads, vector compensation will effectively reduce the level of the magnetic field of a two-circuit 110 kV transmission line «ChTPP – Chernihiv-330» (a point with a safe level of the magnetic flux density for humans is within the protection zone at a distance of 18.3 m from the axis of the power line).

In the area of passage of this transmission line at a distance of 20 m from its axis of symmetry is a residential multi-storey building with a height of about 20 m . Figure 10 shows the location of the building, as well as the location of the coordinate system for calculating the magnetic flux density on the facade of the building along the coordinate «y».

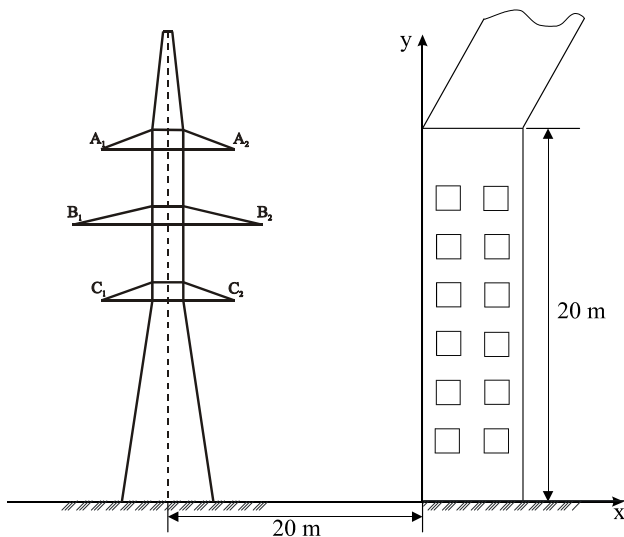
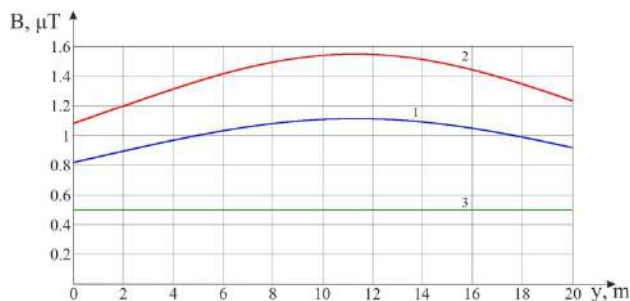


Fig. 10. Location of a multi-storey residential building in the protection zone of the two-circuit 110 kV transmission line «ChTPP – Chernihiv-330»

The results of the calculation of the distribution of the magnetic flux density on the facade of a residential building along the coordinate «y» are shown in Fig. 11.



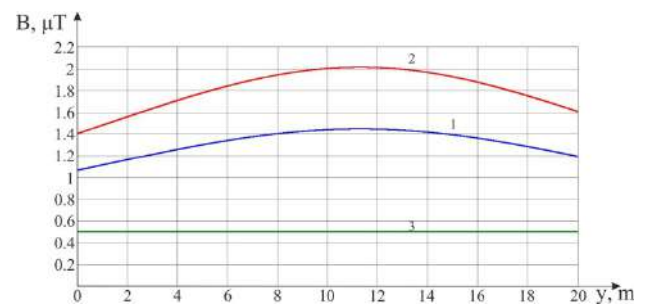
- 1 – at the effective value of the current in the phases of both circuits of 150 A ;
- 2 – at disconnection of one circuit (effective value of the current of the second circuit is 300 A);
- 3 – line of the normative level of magnetic flux density of $0.5 \mu\text{T}$

Fig. 11. Magnetic flux density of the 110 kV overhead transmission line «ChTPP – Chernihiv-330» on the facade of a multi-storey building

As can be seen from Fig. 11, on the facade of a multi-storey building, the normative value of the magnetic flux density of $0.5 \mu\text{T}$ is significantly exceeded more than 2 times with a uniform load of both circuits, and more than 3 times if one of the circuits is switched off. In [15, 16] and in a number of other investigations it is noted that the magnetic field penetrates into apartment houses practically without weakening.

Similar graphs are constructed for promising electrical loads (see Fig. 12).

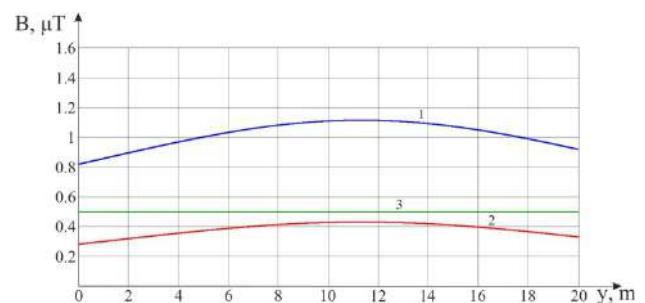
From curve 2 in Fig. 12, which corresponds to the single-circuit mode of operation, it is seen that at $y = 11 \text{ m}$ there is an excess of the magnetic flux density by 4 times. Obviously, it is necessary to use magnetic field reduction techniques here.



- 1 – at the effective value of the current in the phases of both circuits of 195 A ;
- 2 – at disconnection of one circuit (effective value of the current of the second circuit is 390 A);
- 3 – line of the normative level of magnetic flux density of $0.5 \mu\text{T}$

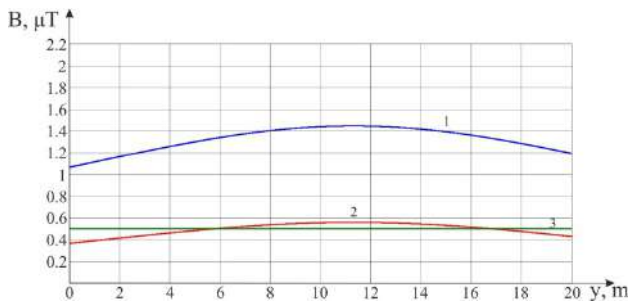
Fig. 12. Magnetic flux density of the 110 kV overhead transmission line ChTPP – Chernihiv-330» on the facade of a multi-storey building at the predicted increase in electrical loads

Figures 13, 14 show the results of the corresponding calculations under the condition of the mirror arrangement of the phases of the two circuits of the transmission line in comparison with the usual variant of their arrangement.



- 1 – for the typical arrangement of the phases of two circuits;
- 2 – for the mirror arrangement of the phases of two circuits;
- 3 – line of the normative level of magnetic flux density of $0.5 \mu\text{T}$

Fig. 13. Magnetic flux density of the 110 kV overhead transmission line «ChTPP – Chernihiv-330» on the facade of a multi-storey building with typical and the mirror arrangement of the phases of the circuits (effective value in the phases of both circuits is 150 A)

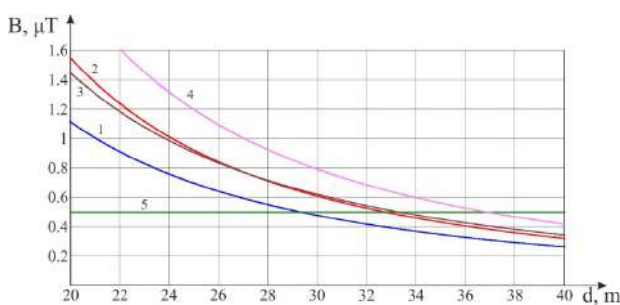


- 1 – for the typical arrangement of the phases of two circuits;
- 2 – for the mirror arrangement of the phases of two circles;
- 3 – line of the normative level of magnetic flux density of 0.5 μT

Fig. 14. Magnetic flux density of the 110 kV overhead transmission line «ChTPP – Chernihiv-330» on the facade of a multi-storey building with typical and the mirror arrangement of the phases of the circuits (effective value in the phases of both circuits is 195 A)

The location of the phases in the mirror symmetry allows to effectively reduce the magnetic field on the facade of a residential building. For phase currents of both circuits equal to 150 A, the excess of the normative value of the magnetic flux density is absent at all points, and for the perspective current of 195 A there will be a slight excess. Obviously, with a further increase in phase current (above 195 A), the vector compensation will no longer be sufficient and other methods of reducing magnetic flux density, such as shielding, will need to be used.

If we do not apply vector compensation, it is obvious that it is necessary to determine the safe distance from the axis of the transmission line to the facades of multi-storey residential buildings, which will be greater than 20 m. The results of the corresponding calculation are shown in Fig. 15. It is assumed that the facade of a multi-storey building can be located at a distance of 20 m to 40 m, and the value of the magnetic flux density is calculated for a point at a height of 11.3 m, as the graphs in Fig. 11, 12 show that it is at this height that the magnetic flux density reaches its maximum value.



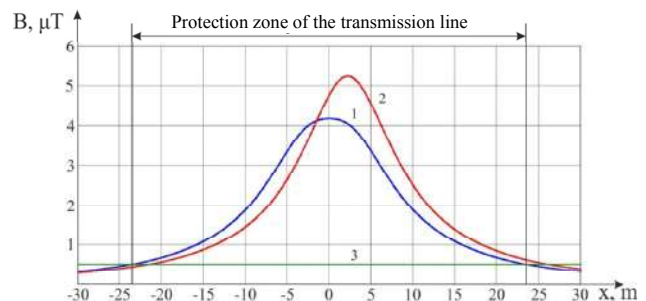
- 1 – at the effective value of the current in the phases of both circuits of 150 A;
- 2 – at disconnection of one circuit (effective value of the current of the second circuit is 300 A);
- 3 – at the effective value of the current in the phases of both circuits of 195 A;
- 4 – at disconnection of one circuit (effective value of the current of the second circuit is 390 A);
- 5 – line of the normative level of magnetic flux density of 0.5 μT

Fig. 15. Magnetic flux density of the 110 kV overhead transmission line «ChTPP – Chernihiv-330» at a height of 11.3 m when changing distance from the axis of the transmission line to the facade of a multi-storey building

Thus, without the use of vector compensation, the facade of a residential building must be located from the axis of the transmission line at a distance of 29 m at the same current in the phases of both circuits of 150 A. When single-circuit transmission lines operation with current of 300 A (or two-circuit operation with promising load of 195 A in the phases of both circuits), the safe distance should be 33 m, it is obvious that this distance is appropriate in the current situation. Provided that only one circuit with phase current of 195 A will operate, the corresponding distance should be 37 m.

The section of the transmission line «ChTPP – Chernihiv-330», built on supports of the PB110-2 type, runs mainly along the private sector of the city, and in some places the supports are actually located in the yards of private houses or close to the fence.

The results of the calculation of magnetic flux density in such a section at the level of 1.8 m in the direction perpendicular to the transmission line route are shown in Fig. 16.



- 1 – at the effective value of the current in the phases of both circuits of 150 A;
- 2 – at disconnection of one circuit (effective value of the current of the second circuit is 300 A);
- 3 – line of the normative level of magnetic flux density of 0.5 μT

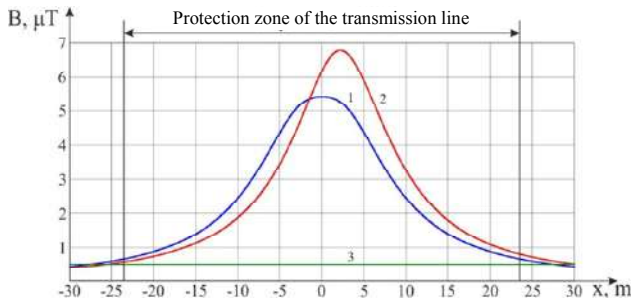
Fig. 16. Distribution of the magnetic flux density of the 110 kV overhead transmission line «ChTPP – Chernihiv-330» at the level of 1.8 m from the earth's surface for the section made on the PB110-2 type supports

Residential houses in this section of the transmission line are located at a distance of 6-10 m from its axis of symmetry, it is obvious that the field at such points can exceed the normative value by 6-8 times. At the boundary of the protection zone of the transmission line (± 23.5 m from the beginning of the coordinate system in Fig. 16) under uniform load of both circuits, the magnetic flux density corresponds to the normative value, in single-circuit mode it is 0.6 μT, and the point with safe magnetic flux density value in this mode corresponds to the coordinate $x = 26$ m. It should also be noted that all houses have attics, and some of them are generally two-story, respectively, the magnetic flux density in such premises will be even greater. It is obvious that the location of buildings within the protection zone of this section of the transmission line is unacceptable.

Similar graphs for the current in phase of 195 A are shown in Fig. 17.

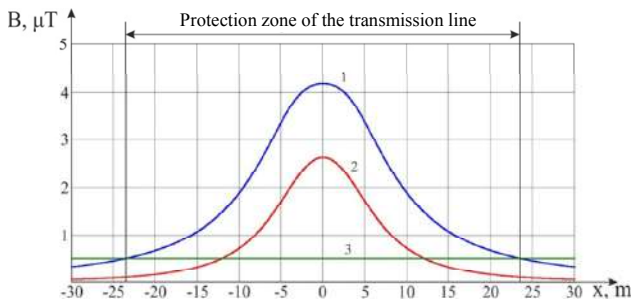
In the two-circuit mode of operation with uniform load on the border of the protection zone on the right side there will be magnetic flux density of 0.65 μT, and in the operation in the single-circuit mode – 0.8 μT. The safe

value of the magnetic flux density is observed at a distance of 27 m and 30 m, respectively.

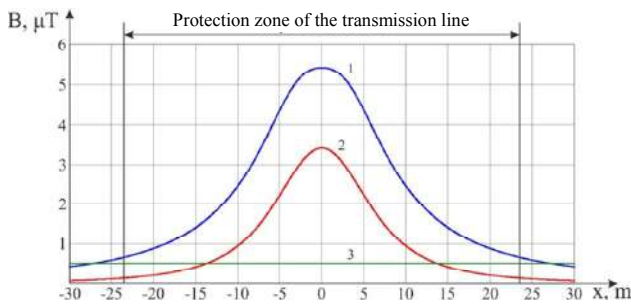


1 – at the effective value of the current in the phases of both circuits of 195 A;
 2 – at disconnection of one circuit (effective value of the current of the second circuit is 390 A);
 3 – line of the normative level of magnetic flux density of $0.5 \mu\text{T}$
 Fig. 17. Distribution of the magnetic flux density of the 110 kV overhead transmission line «ChTPP – Chernihiv-330» for the section made on the PB110-2 type supports at the predicted increase in electrical loads

The use of vector compensation in this case will also achieve a significant improvement in the situation, as seen in Fig. 18, 19.



1 – for the typical arrangement of the phases of two circuits;
 2 – for the mirror arrangement of the phases of two circles;
 3 – line of the normative level of magnetic flux density of $0.5 \mu\text{T}$
 Fig. 18. Distribution of the magnetic flux density of the 110 kV overhead transmission line «ChTPP – Chernihiv-330» at the level of 1.8 m from the earth's surface along the «x» coordinate for the section made on supports type PB110-2, with typical and the mirror arrangement of the phases of the circuits (effective value of the current in the phases of both circuits is 150 A)



1 – for the typical arrangement of the phases of two circuits;
 2 – for the mirror arrangement of the phases of two circles;
 3 – line of the normative level of magnetic flux density of $0.5 \mu\text{T}$
 Fig. 19. Distribution of the magnetic flux density of the 110 kV overhead transmission line «ChTPP – Chernihiv-330» at the level of 1.8 m from the earth's surface along the «x» coordinate for the section made on supports type PB110-2, with typical and the mirror arrangement of the phases of the circuits (effective value of the current in the phases of both circuits is 195 A)

For the case shown in Fig. 15, the safe value of the magnetic flux density of $0.5 \mu\text{T}$ is already at a distance of 12 m from the centerline of the transmission line route, at the boundary of the protection zone the magnetic flux density is $0.1 \mu\text{T}$. It should also be noted that for the section made on the supports PB110-2, the mirror arrangement of the phases of the circuits allows to significantly reduce the magnetic flux density at all points in space at the level of 1.8 m, including directly below the transmission line route.

Figure 19 shows that at currents in the phases of each circuit of 195 A changing the location of the phases of different circuits in mirror symmetry (vector compensation) also allows to effectively reduce the magnetic field of the transmission line, the magnetic flux density reaches a safe value at a distance of 13.8 m from the center the transmission line route, and at the boundary of the protection zone is $0.13 \mu\text{T}$.

The results of the calculation of the magnetic flux density at the currents obtained in JSC «Chernihivoblenergo» were checked using the device TM-192 of the TENMARS Company, which is designed to measure the magnetic flux density of power frequency in the range of $0.01\text{--}200 \mu\text{T}$. The measurement results confirm the correctness of the calculations.

Conclusions.

In this work the magnetic field of the two-circuit 110 kV overhead transmission line «ChTPP – Chernihiv-330» passing through the residential area in different modes of its operation (single-circuit and two-circuit) under current and perspective load is considered and the ways of its reduction to the safe level are investigated.

It is shown that the level of the magnetic flux density of the two-circuit 110 kV transmission line «ChTPP – Chernihiv-330» at existing and prospective loads (current of one phase of each circuit of 150 A and 195 A, respectively, or of 300 A and 390 A when operating in single-circuit mode) can exceed the normative level of $0.5 \mu\text{T}$ at the boundary of the protection zone up to twice, and a particularly significant level of the magnetic flux density will be observed during the operation of the transmission line in single-circuit mode at prospective load.

It is determined that safe living of the population along the route of this two-circuit transmission line is achieved if the facades of residential buildings are at least 33 m away from the axis of the transmission line for multi-storey buildings and at least 27 m for single-storey buildings.

When working in two-circuit mode in case of exceeding the normative level of the magnetic flux density, it is recommended to use the method of vector compensation [10], which is realized by the mirror location of the wires of different circuits of the transmission line. It is shown that this method allows to effectively reduce the level of the magnetic field of the given transmission line outside its route and, in particular, at the boundary of the protection zone.

Further reduction of the negative impact of the magnetic field on the population in the conditions of increasing electric loads can be achieved by limiting the operating time of two-circuit transmission lines in single-

circuit mode, characterized by increased magnetic field from the operating circuit, and the use of magnetic field shielding.

REFERENCES

1. Marincu A., Greconici M., Musuroi S. The electromagnetic field around a high voltage 400 kV electrical overhead lines and the influence on the biological systems. *Facta universitatis - series: Electronics and Energetics*, 2005, vol. 18, no. 1, pp. 105-111. doi: **10.2298/fuee0501105m**.
2. Conti R., Giorgi A., Rendina R., Sartore L., Sena E.A. Technical Solutions To Reduce 50 Hz Magnetic Fields from Power Lines. *Proceedings of Power Tech Conference IEEE 2003*, 23-26 June, 2003, Bologna (Italy), 2003, vol. 2, 6 p. doi: **10.1109/ptc.2003.1304685**.
3. Moro F., Turri R. Fast analytical computation of power-line magnetic fields by complex vector method. *IEEE Transactions on Power Delivery*, 2008, vol. 23, no. 2, pp. 1042-1048. doi: **10.1109/tpwr.2007.915212**.
4. *Electrical installation regulations*. Kharkiv, Fort Publ., 2017. 760 p. (Ukr).
5. Krasnozhon A.V., Buinyi R.O., Pentegov I.V. Calculation of active power losses in the grounding wire of overhead power lines. *Technical electrodyamics*, 2016, no. 4, pp. 23-25. (Ukr). doi: **10.15407/techned2016.04.023**.
6. Geri A., Locatelli A., Veca G.M. Magnetic fields generated by power lines. *IEEE Transactions on Magnetism*, 1995, vol. 31, no. 3, pp. 1508-1511. doi: **10.1109/20.376316**.
7. Moro F., Turri R. Accurate calculation of the right-of-way width for power line magnetic field impact assessment. *Progress In Electromagnetics Research B*, 2012, vol. 37, pp. 343-364. doi: **10.2528/pierb11112206**.
8. Pelevin D.Ye. The methods of reducing of the magnetic fields of overhead power lines outside security zones. *Technical Electrodyamics*, 2014, no. 5, pp. 14-16. (Rus).
9. Rozov V.Yu., Reutskiy S.Yu., Pelevin D.Ye., Yakovenko V.N. The research of magnetic field of high-voltage AC transmissions lines. *Technical Electrodyamics*, 2012, no. 1, pp. 3-9. (Rus).
10. Rozov V.Yu., Reutskiy S.Yu., Pelevin D.Ye., Pyliugina O.Yu. The magnetic field of power transmission lines and the methods of its mitigation to a safe level. *Technical Electrodyamics*, 2013, no. 2, pp. 3-9. (Rus).
11. Shangzun Y., Pengfei L., Ling N. Study on electromagnetic radiation of ultra-high voltage power transmission line. *International Conference on Computer Science and Information Technology*, 2008, pp. 402-406. doi: **10.1109/ICCSIT.2008.92**.
12. *SOU-N EE 20.179:2008. Calculation of electric and magnetic fields of power lines. Method (with changes)*. Kyiv, Minenergovugillja Ukrainy Publ., 2016. 37 p. (Ukr).
13. Rozov V.Yu., Reutskiy S.Yu., Piliugina O.Yu. The method of calculation of the magnetic field of three-phase power lines. *Technical electrodyamics*, 2014, no. 5, pp. 11-13. (Rus).
14. *Scheme of perspective development of 35-110 kV electric grids on PJSC «Chernihivoblenergo» for 2017-2027*. Kyiv, PJSC PTI «Kyivorgbud», 2017. (Ukr).
15. *Regulating Power Line EMF Exposure: International Precedents*. Available at: <https://elc.uvic.ca/wordpress/wp-content/uploads/2015/01/Regulating-Power-Line-EMF-Exposure.pdf> (Accessed 02 August 2020).
16. Burnett J., Yaping P.D. Mitigation of extremely low frequency magnetic fields from electrical installations in high-rise buildings. *Building and Environment*, 2002, vol. 37, no. 8-9, pp. 769-775. doi: **10.1016/S0360-1323(02)00043-4**.

Received 14.09.2020

Accepted 10.11.2020

Published 24.12.2020

A.V. Krasnozhon¹, Candidate of Technical Science,
R.O. Buinyi¹, Candidate of Technical Science,
I.V. Dihtyaruk¹, Candidate of Technical Science,
A.O. Kvytsynskiy², Candidate of Technical Science,
¹Chernihiv Polytechnic National University,
95, Shevchenko Str., Chernihiv, 14035, Ukraine,
e-mail: buinyiroman@gmail.com, Dihtyaruk.ihor@gmail.com,
red_john@ukr.net
²Department of research support of regulatory support
of the NPC Ukrenergo,
11/8, Dorohozhytska Str., Kyiv, 04112, Ukraine,
e-mail: Kvytsynskiy.AO@ua.energy

How to cite this article:

Krasnozhon A.V., Buinyi R.O., Dihtyaruk I.V., Kvytsynskiy A.O. The investigation of distribution of the magnetic flux density of operating two-circuit power line 110 kV «ChTPP-Chernihiv-330» in the residential area and methods of its decreasing to a safe level. *Electrical engineering & electromechanics*, 2020, no. 6, pp. 55-62. doi: **10.20998/2074-272X.2020.6.08**.

R. Lebled, R. Lalalou, H. Benalla, K. Nebti, I. Boukhechem

AMELIORATE DIRECT POWER CONTROL OF STANDALONE WIND ENERGY GENERATION SYSTEM BASED ON PERMANENT MAGNET SYNCHRONOUS GENERATOR BY USING FUZZY LOGIC CONTROL

Purpose. Electricity is a basic energy for life and its consumption increased so we need the discovery of new sources of energy such as wind energy for this ameliorate the quality of generated wind energy by using the intelligent artificial control, this control is made to optimize the performance of three-phase PWM rectifier working. **Methodology.** These strategies are based on the direct control of the instantaneous power, namely: the control direct power control (DPC) with classic PI regulator and direct power control with fuzzy logic regulator. The fuzzy characterized by its ability to deal with the imprecise, the uncertain has been exploited to construct a fuzzy voltage regulator. The simulation of these methods was implemented using Matlab/Simulink. **Results.** A comparison with the results obtained by the classic PI showed the improvement in dynamic performance. This makes the fuzzy controller an acceptable choice for systems requiring quick, precise adjustments and less sensitive to outside disturbances. **Originality.** The proposed this control strategy using for to obtain a performance adjustment of the DC bus voltage and sinusoidal currents on the network side. **Practical value.** Fuzzy logic is proven to be effective in terms of reducing the harmonic distortion rate of the currents absorbed, correct adjustment of the active and reactive power and DC voltage and unit power factor operation. References 26, tables 6, figures 15.

Key words: direct power control, fuzzy logic control, permanent magnet synchronous generator (PMSG), PWM technique, wind energy system.

Мета. Електроенергія є основною енергією для життя, і її споживання збільшується, тому нам необхідно відкриття нових джерел енергії, таких як енергія вітру. Для поліпшення якості енергії вітру, що генерується за допомогою управління на основі штучного інтелекту, таке управління призначене для оптимізації продуктивності роботи трифазного ШІМ випрямляча. **Методологія.** Дані стратегії засновані на прямому управлінні миттєвою потужністю, а саме: пряме управління потужністю з класичним ПІ-регулятором і пряме управління потужністю регулятором з нечіткою логікою. **Нечіткість,** що характеризується її здатністю справлятися з неточністю, невизначеністю, була використана для створення нечіткого регулятора напруги. **Моделювання** цих методів було реалізовано за допомогою Matlab/Simulink. **Отримані результати.** Порівняння з результатами, отриманими за допомогою класичного ПІ-регулятора, показало поліпшення динамічних характеристик. **Це робить нечіткий контролер прийнятним вибором для систем, що вимагають швидкої і точної настройки і менш чутливих до зовнішніх перешкод.** **Оригінальність.** Запропоновано стратегію управління, що використовує для отримання регулювання продуктивності напруги шини постійного струму і синусоїдальні струми на стороні мережі. **Практична цінність.** Доведено, що нечітка логіка ефективна з точки зору зниження коефіцієнта гармонійних спотворень поглинаються струмів, коректного регулювання активної і реактивної потужності і постійної напруги, а також коефіцієнта потужності роботи блоку. Бібл. 26, табл. 6, рис. 15.

Ключові слова: пряме управління потужністю, управління з нечіткою логікою, синхронний генератор з постійними магнітами, метод ШІМ, вітроенергетична система.

Introduction. The readily available renewable energy especially the abundant resources of solar energy and wind energy have led to a steady growth of interest concerning distributed generation units. As the adoption of system into the smart power grid is seen a tendency of becoming a new paradigm to sustainable energy, the integration of power converters to take control of the smart grid operation become one of the main research areas that require immense attention. The three phase grid connected voltage source converter which features Bidirectional power flow, nearly sinusoidal input currents, controllable power factor, and high quality DC output voltage have made it an increasingly important proportion in renewable energy system [1].

There are three type of renewable energy:

- mechanical energy (wind energy);
- electric energy (photovoltaic panels);
- energy in the form of heat (geothermal, solar [2]).

Wind energy, is one of the available non-conventional energy sources, which is clean and an infinite natural resource. Wind power is still the most promising renewable energy in the year of 2013. The wind turbine system (WTS) started with a few tens of kilowatt power in the

1980s. Now multi-megawatt wind turbines are widely installed even up to 6-8 MW [3] (Fig. 1).

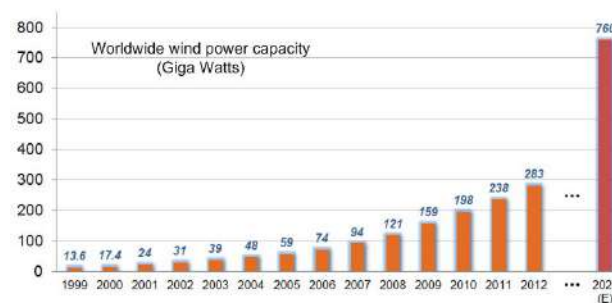


Fig. 1. Global cumulative installed wind power capacity from 1999 to 2020 [3]

Wind energy based power system operation is challenging under fluctuating nature of wind speeds and variable load conditions, particularly when the operation mode of the hybrid wind power system is stand alone. The changing wind speeds causes fluctuations in wind-turbine generator, which causes fluctuations in load

voltage and frequency in the stand-alone wind-energy system. Variable speed wind-turbine systems are more advantageous when compared with the fixed speed wind turbine systems. They generate maximum amount of power and gives less mechanical stress, higher power quality and efficiency than fixed speed wind-turbine systems [4, 5]. Standalone wind energy conversion systems are electric energy alternative sources for isolated area. They usually supplies air conditioning mechanical loads, ventilation and water pumps [6]. Various control strategies have been proposed in recent works on this type of PWM rectifier. It can be classified for its use of current rent loop controllers or active/reactive power controllers. The well-known method of indirect active and reactive power control is based on current vector orientation with respect to the line voltage vector. It is called voltage oriented control (VOC) [7]. VOC guarantees high dynamics and static performance via internal current control loops. However, the final configuration and performance of the VOC system largely depends on the quality of the applied current control strategy. Over the last few years, an interesting emerging control technique has been direct power control (DPC), developed analogously with the well-known direct torque control (DTC) used for adjustable speed drives [8]. Therefore, the wind generating system is found to be of a great potential as a very attractive supply option for industrial and domestic applications. Several electrical generators can be used to perform the electromechanical energy conversion. Permanent magnet synchronous generator (PMSG) offer significant advantages over conventional synchronous generators as a source of isolated supply. Brushless, absence of a separate DC source, and maintenance free are among the advantages. However the variable natural of wind and the fluctuation of load profiles lead to fluctuating torque of the wind turbine generator. This causes variation in the output voltage and frequency [9]. The relay control can be performed by selecting an optimum switching state of the converter, so that the active and reactive power errors can be restricted in appropriate hysteresis bands, which is possible by using a switching table and several hysteresis comparators. The latter is based on a calculation of the voltages for each switching state of the converter by detecting the line currents, and the calculation is performed by utilizing the active and reactive power as intermediate variables. Since this method deals with instantaneous variables in obtaining the voltages, it is possible to estimate not only a fundamental component [10]. Fuzzy logic control has found many applications in the past two decades. This is so largely increasing because fuzzy logic control has the capability to control nonlinear uncertain systems even in the case where no mathematical model is available for the control system [11]. This paper proposes a novel DPC for a three phase PWM rectifier, which makes it possible to achieve unity power factor operation by directly controlling its instantaneous active and reactive power without any power-source voltage sensors. In this situation, the DPC based on fuzzy logic control is used instead of DPC. This control technique greatly lowers the

fluctuations of the active and reactive power and the harmonic distortion rate THD [12].

This paper is organized into the following sections:

- Section I describes about the stand-alone wind energy system configuration with PMSG modeling;
- Section II represented different control strategies;
- Section III discusses about the simulation results;
- Conclusions.

Section I. Stand-alone wind energy supply system. The system consists of the following components (parameters are presented in Appendix in Tables A.1 – A.3):

- wind turbine;
- PMSG which is directly driven by the wind turbine without using a gearbox;
- uncontrolled rectifier PWM.

Profile wind turbine model. The first step necessary for a wind production project is the geographical choice of the site. The properties of wind are interesting for the study of the whole wind energy conversion system, since its power, under ideal conditions, is proportional to the cube of the wind speed. To know the characteristics of a site, it is essential to have measurements of the wind speed and its direction, over a long period of time. It is modeled by an addition of a number of harmonics and the wind speed variation is according to the following equation [13, 14]:

$$V = 6.5 + (0.2 \sin(0.1074t) + 2 \sin(0.2665t) + \sin(1.2930t) + 0.2 \sin(3.6645t)). \quad (1)$$

Turbine modeling. The turbine is a device used to convert wind energy into mechanical energy. The mechanical power P of wind turbine extracted from the wind can be expressed as follows [15]

$$P = C_p P_\omega = \frac{1}{2} C_p \rho \pi R^2 V^3, \quad (2)$$

where C_p is the power coefficient which is a function of the pitch angle of rotor blades θ [deg] and of the tip-speed ratio λ ; P_ω is the dynamic force; ρ [kg/m³] is the air density; R [m] is the blade turbine radius; V [m/s] is the wind speed.

The dynamic force accessible:

$$P_\omega = \frac{1}{2} \rho S V^3 = \frac{1}{2} \rho \pi R^2 V^3. \quad (3)$$

The tip-speed ratio λ is defined as

$$\lambda = \frac{\Omega R}{V}, \quad (4)$$

where Ω is the angular mechanical speed of the turbine rotor.

Modeling of PMSG. AC machines are generally modeled by non-linear equations (differential equation). This non-linearity is due to the inductances and coefficients of the dynamic equations which depend on the rotor position and time. A three phase – two phase transformation necessary to simplify the model (reduce the number of equations). In the PMSG, the rotor excitation is supposed constant. The electrical equation represented by [16, 17]:

$$V_d = -R_s I_d - L_d \frac{d}{dt} I_d + \omega_r L_q I_q; \quad (5)$$

factor. The following expression gives the line currents i_a , i_b , i_c in the stationary coordinates $\alpha - \beta$

$$\begin{bmatrix} i_\alpha \\ i_\beta \end{bmatrix} = \sqrt{\frac{2}{3}} \begin{bmatrix} 1 & -\frac{1}{2} & -\frac{1}{2} \\ 0 & \frac{\sqrt{3}}{2} & -\frac{\sqrt{3}}{2} \end{bmatrix} \begin{bmatrix} i_a \\ i_b \\ i_c \end{bmatrix}. \quad (28)$$

We can write the expressions of the active and reactive powers as follows [21]:

$$P = \underline{V}_{(abc)} \cdot i_{(abc)} = \underline{V}_\alpha i_\alpha + \underline{V}_\beta i_\beta; \quad (29)$$

$$Q = \underline{V}_{(abc)} \wedge i_{(abc)} = \underline{V}_\alpha i_\beta - \underline{V}_\beta i_\alpha. \quad (30)$$

The matrix writing of the expressions (29) and (30) is:

$$\begin{bmatrix} P \\ Q \end{bmatrix} = \begin{bmatrix} V_\alpha & V_\beta \\ -V_\alpha & V_\beta \end{bmatrix} \begin{bmatrix} i_\alpha \\ i_\beta \end{bmatrix}. \quad (31)$$

The matrix equation (31) can be rewritten, depending on the line current (measured) and the power (estimated), as follows:

$$\begin{bmatrix} V_\alpha \\ V_\beta \end{bmatrix} = \frac{1}{i_\alpha^2 + i_\beta^2} \begin{bmatrix} i_\alpha & -i_\beta \\ i_\beta & i_\alpha \end{bmatrix} \begin{bmatrix} P \\ Q \end{bmatrix}. \quad (32)$$

Concordia's inverse transform of line voltages is written [22]:

$$\begin{bmatrix} V_a \\ V_b \\ V_c \end{bmatrix} = \sqrt{\frac{2}{3}} \begin{bmatrix} 1 & 0 \\ -\frac{1}{2} & \frac{\sqrt{3}}{2} \\ \frac{1}{2} & -\frac{\sqrt{3}}{2} \end{bmatrix} \begin{bmatrix} V_\alpha \\ V_\beta \end{bmatrix}. \quad (33)$$

Hysteresis controller. The main idea behind the DPC method is to maintain the instantaneous active and reactive powers within a desired band. DPC consists of two hysteresis comparators whose inputs are the errors between the reference and estimated values of the active and reactive powers, respectively.

$$\begin{cases} \Delta P = P_{ref} - P; \\ \Delta Q = Q_{ref} - Q. \end{cases} \quad (33)$$

The hysteresis comparators provide two logic outputs d_p and d_q . The state «1» corresponds to an increase in the controlled variable (P and Q), while «0» corresponds to a decrease

$$\begin{cases} \text{if } \Delta P \geq h_p \Rightarrow d_p = 1; \\ \text{if } \Delta P < -h_p \Rightarrow d_p = 0; \\ \text{if } \Delta Q \geq h_Q \Rightarrow d_Q = 1; \\ \text{if } \Delta Q < -h_Q \Rightarrow d_Q = 0, \end{cases} \quad (35)$$

where h_p and h_Q denote the hysteresis bands [21].

Switching table. The digital error signals S_p and S_Q and the working sector are the inputs of the switching table where the switching states S_a , S_b and S_c the PWM rectifier are stored. By using the table, the optimum switching state of the converter can be chosen at each switching state according to the combination of the digital signals S_p and S_Q sector number, that is to say, that the choice of the optimum switching state is made so that the error of the active power can be restricted in a hysteresis

band of width $2H_p$, and likewise for the error of reactive power, with a band of width [22].

The sectors can be numerically expressed as:

$$(n-2)\frac{\pi}{6} \leq \theta_n \leq (n-1)\frac{\pi}{6}, \quad (36)$$

where $n = 1, 2, \dots, 12$.

By using several comparators, it is possible to specify the sector where the voltage vector exists. The digitized error signals S_p and S_Q digitized voltage phase are θ_n input to the switching table in which every switching state of the converter is stored, as shown in Table 1. By using this switching table, the optimum switching state S_a , S_b and S_c of the converter can be selected uniquely in every specific moment according to the combination of the digitized input signals (Fig. 3). The selection of the optimum switching state is performed so that the power errors can be restricted within the hysteresis bands [23].

Table 1

Possible switching table							
S_p	S_Q	θ_1	θ_2	θ_3	θ_4	θ_5	θ_6
0	0	v_6	v_1	v_1	v_2	v_2	v_3
	1	v_1	v_2	v_2	v_3	v_3	v_4
1	0	v_5	v_6	v_6	v_1	v_1	v_2
	1	v_3	v_4	v_4	v_5	v_5	v_6
S_p	S_Q	θ_7	θ_8	θ_9	θ_{10}	θ_{11}	θ_{12}
0	0	v_3	v_4	v_4	v_5	v_5	v_6
	1	v_4	v_5	v_5	v_6	v_6	v_1
1	0	v_2	v_3	v_3	v_4	v_4	v_5
	1	v_6	v_1	v_1	v_2	v_2	v_3

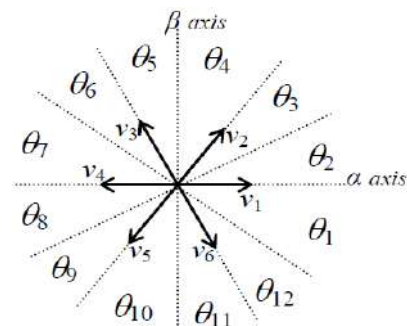


Fig. 3. The vector plane divided into 12 sectors

External voltage regulation loop. The external regulation loop maintains a load assimilated to a resistance R . The impedance thus formed is charged by the current i_{dc} from the PWM rectifier. The current i_{dcref} is the current from the PWM rectifier (Fig. 4). The product of the reference DC with the DC voltage gives the active power of reference. Capacitance voltage DC at a reference voltage is u_{dcref} . The capacity C is in parallel with load (resistance).

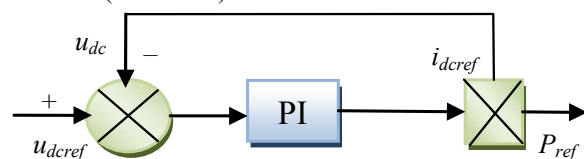


Fig. 4. DC voltage regulation

Fuzzy logic control for DPC. Improving the quality of the currents absorbed by the PWM rectifier and maintaining of the DC voltage at the output around the of the DC voltage at the output around the reference requires voltage regulation and fast and robust currents[24]. For this reason presents a DPC operating with a fuzzy logic controller which replaces voltage in conventional commands. Figure 5 gives the block diagram of the proposed fuzzy logic controller for DPC of three-phase PWM rectifier.

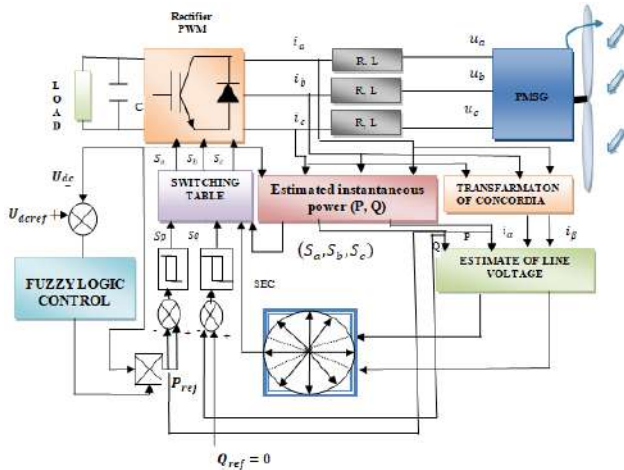


Fig. 5. The block diagram of fuzzy logic controller for DPC of three-phase PWM rectifier

The configuration of the voltage loop is illustrated in Fig. 6, it is composed of [25]:

- normalization factors relate to the error (e) and the variation of the command (Δe);
- a block of fuzzification of the error and its variation;
- rule of inference. The control strategy is presented by an inference matrix presented in table;
- a defuzzification block used to convert the fuzzy control variation into a digital value.

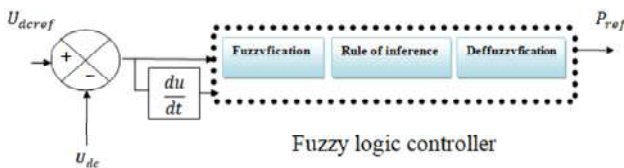


Fig. 6. Diagram of the proposed fuzzy logic controller for DPC

Fuzzification. This step deals with the transformation of numeric values to inputs into fuzzy values or linguistic variables. The input variables which are the velocity error and its variation are subjected to a fuzzification operation and therefore converted to fuzzy sets. The normalized universe of speech of each variable of the regulator (the error, its variation and the variation of the command) is subdivided into seven fuzzy sets; these are characterized by the following standard designations:

- large negative noted LN;
- average negative noted AN;
- small negative noted SN;
- about zero noted AZ;

- positive small noted PS;
- average positive noted AP;
- large positive noted LP.

For the membership functions we chose for each variable the triangular and trapezoidal shapes.

Inference rules. The rule base represents the control strategy and desired goal through linguistic control rules. It makes it possible to determine the decision or action at the output of the fuzzy controller and to express qualitatively the relationship that exists between the input variables and the output variable. From the study of the behavior of the system, we can establish the control rules, which connect the output with the inputs. As we mentioned, each of the two linguistic inputs of the fuzzy controller has seven fuzzy sets.

Fuzzy rules table (Table 2) showing change in control output [26].

Table 2

Fuzzy rules table

$e \backslash \Delta e$	LN	AN	SN	AZ	PS	AP	LP
LN	LN	LN	LN	LN	AN	SN	AZ
AN	LN	LN	LN	AN	SN	AZ	PS
SN	LN	LN	AN	SN	AZ	PS	AP
AZ	LN	AN	SN	AZ	PS	AP	LP
PS	AN	SN	AZ	PS	AP	LP	LP
AP	SN	AZ	PS	AP	LP	LP	LP
LP	AZ	PS	AP	LP	LP	LP	LP

The logic for determining this matrix of rules is based on a global or qualitative knowledge of the functioning of the system. As an example, consider the following two rules:

- if e is LP and Δe is LP then Δu is LP;
- if e is AZ and Δe is AZ then Δu is AZ.

They indicate that if the speed is too small compared to its reference (e is LP and Δe is LP), then a large torque demand (Δu is PG) is needed (to bring the speed back to its reference). And if the speed meets its reference and settles (e is AZ and Δe is AZ) then keep the same torque (Δu is EZ).

Defuzzification. When the fuzzy output is calculated, it must be transformed into a numeric value. There are several methods to achieve this transformation. The most used is the center of gravity method, which we have adopted in our work. The abscissa of the center of gravity corresponding to the output of the regulator is given by:

$$\Delta U = \frac{\int x\gamma(x)dx}{\int \gamma(x)dx} \quad (37)$$

Section III. Discusses about the simulation results and discussion. Simulations and results of DPC are presented in Fig. 7-15. We present the wind turbine profile (Fig. 7); the stator voltages of PMSG (Fig. 8); the stator voltage and current of PMSG (Fig. 9); the rectified

voltage DPC (Fig. 10); the active (Fig. 11) and reactive (Fig. 12) power for classic DPC and fuzzy DPC technique (Fig. 13-15).

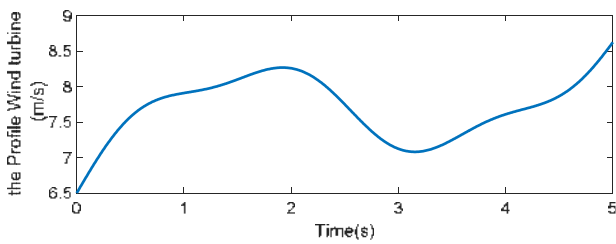


Fig. 7. The profile wind turbine

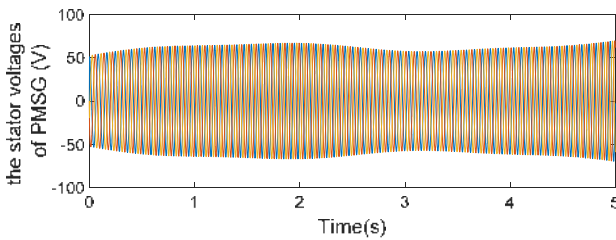


Fig. 8. The stator voltages of PMSG

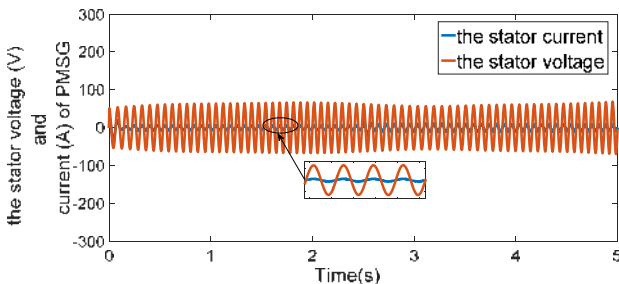


Fig. 9. The stator voltage and current of PMSG

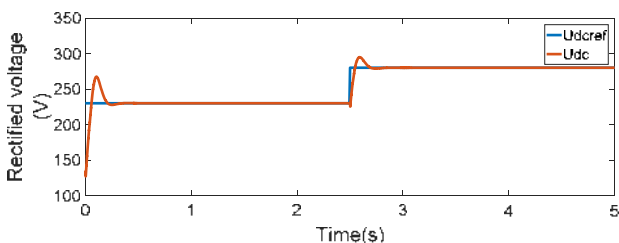


Fig. 10. The rectified voltage DPC

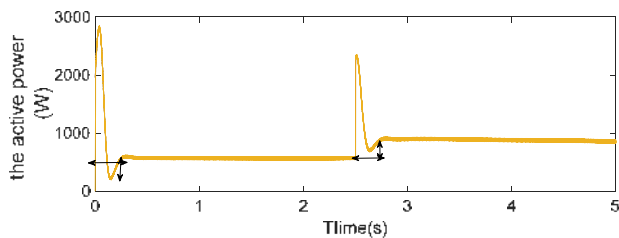


Fig. 11. The active power DPC

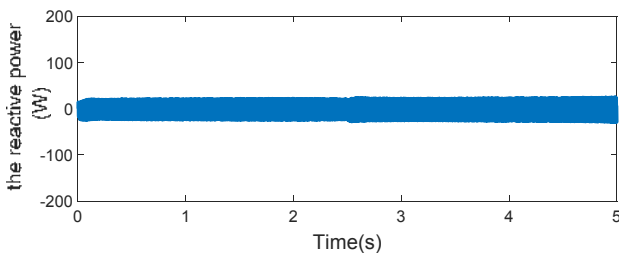


Fig. 12. The reactive power DPC

Simulations and results of Fuzzy logic control for DPC.

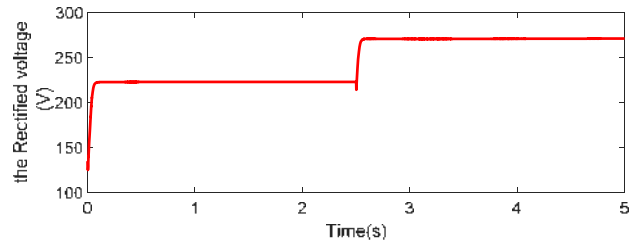


Fig. 13. Rectified voltage DPC fuzzy logic

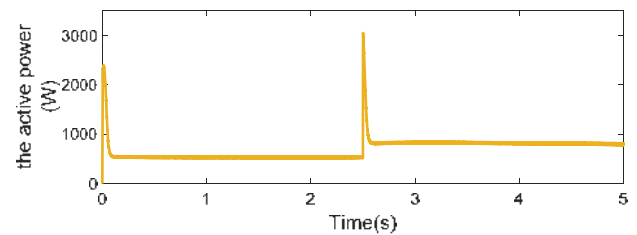


Fig. 14. The active power DPC fuzzy logic

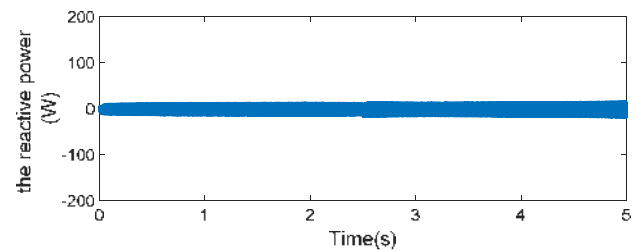


Fig. 15. The reactive power DPC fuzzy logic

During the transient response (Fig. 10) shows that there is an overshooting in the rectifier output voltage caused by PI parameters choice and the signal produced by the start of the PMSG, but at ($t = 0.3$ to 2.5 s), note that the direct voltage reaches its reference value (230 V) and (280 V), but for fuzzy logic the direct voltage reaches its reference value from ($t = 0$ to 0.025 s) (Fig. 13), and the instantaneous powers (P , Q) followed by the reference power ($P = 550$ W) and ($P = 850$ W) in the Fig. 11, and ($q = 0$ vAR) with a considerable presence of oscillations around the reference (Fig. 12), but for the DPC by PI regulator from ($t = 0$ to 0.3 s) the response very slow and from ($t = 2.5$ to 2.8 s) it there is a disturbance produced by the change of the reference voltage on the other hand fuzzy logic DPC instantaneous powers (P , Q) followed by the reference power from ($t = 0.24$ s) and response time speed very and the absence of disturbance produced by the change in the reference voltage (Fig. 14) and decrease in oscillations around the reference (Fig. 15), the voltage and current of the PMSG are in phase, and the line currents are sinusoidal (Fig. 9).

The active and reactive power responses follow their references perfectly, these results, show the superiority of fuzzy regulator compared to the conventional PI. With fuzzy regulators no overshoot is produced, fast response in transient conditions and the static error is nearly zero.

THD comparative study. The objective of this study is to show the contribution of each two methods presented throughout this work. The two criteria taken into account in evaluating the performance of these

controls are: the rate of distortion of the network currents (THD). Table 3 shows the THD values obtained in steady state for the two control modes. All of these commands give acceptable THD values of less than 5 %. We also notice the superiority of fuzzy logic regulator over the other control; in fact, it can reduce the THD to a low value of approximately 1.87 %.

Table 3

THD values		
Control	Classical regulator PI for DPC	Fuzzy logic control for DPC
THD % ($f=12.8$ Hz)	3.58 %	1.87 %

Conclusion.

The proposed control is simple, robust, not sensitive to the parametric disturbance and variation of the system, and with very good dynamic characteristics. For DPC fuzzy the value of rectified voltage is 0.025 s and very speed time response of disturbance produced by the change in the reference voltage 0.01 s. It can be said that the use of fixed PI regulators gives a robust control system and an acceptable response 0.3 s, but the conventional problems of the PI regulator such as the response time and the robustness against external disturbances have appeared, and to solve the problems mentioned above we will use the fuzzy control to establish a regulator robust.

The fuzzy logic adjustment gives a very programmatic approaches, allowing integrating the knowledge acquired by the operators.

Spectral analysis of line current shows that all low-order harmonics are well attenuated which gives a THD around to 3.6 %.

The fuzzy DPC simulation results obtained good performance in steady state and transient conditions especially for the case of current harmonic distortion rate which is good for other techniques; it is able to reduce the THD to a low value of around 1.87 % with better convergence of active power ($P=550$ W and $P=850$ W), however reactive power ($q=0$ VAR) towards their respective references.

APPENDIX

Wind turbine parameters

Table A.1

Parameter	Symbol	Value
Power	P	7.5 kW
Radius	R	3.24 m
Inertia	J	7.5 kg·m ²
Friction coefficient	F	0.06 N·m·s/rad

PMSG parameters

Table A.2

Parameter	Symbol	Value
Direct stator inductance	L_d	0.012 H
Stator quadrature inductance	L_q	0.0211 H
Permanent magnet flux	φ_r	0.9 Wb
Stator resistance	R_s	0.895 Ω
Inertia	J	0.00141 kg·m ²
Number of poles	n_p	3
Friction force	F	0 N·m/rad·s

Rectifier parameters

Parameter	Symbol	Value
Line resistance	R_l	0.7 Ω
Line inductance	L	0.01 H
Filtering capacity	C	0.0033 F
DC voltage reference	U_{dref}	230 – 280 V

REFERENCES

- Rodriguez J.R., Dixon J.W., Espinoza J.R., Pontt J., Lezana P. PWM regenerative rectifiers: state of the art. *IEEE Transactions on Industrial Electronics*, 2005, vol. 52, no. 1, pp. 5-22. doi: 10.1109/TIE.2004.841149.
- Singh M., Chandra A., Singh B. Sensorless Power maximization of PMSG based isolated wind-battery hybrid system using adaptive neuro-fuzzy controller. *2010 IEEE Industry Applications Society Annual Meeting*, Oct. 2010. doi: 10.1109/IAS.2010.5615370.
- Blaabjerg F., Ke Ma. Future on power electronics for wind turbine systems. *IEEE Journal of Emerging and Selected Topics in Power Electronics*, 2013, vol. 1, no. 3, pp. 139-152. doi: 10.1109/JESTPE.2013.2275978.
- Barton J.P., Infield D.G. Energy storage and its use with intermittent renewable energy. *IEEE Transactions on Energy Conversion*, 2004, vol. 19, no. 2, pp. 441-448. doi: 10.1109/TEC.2003.822305.
- Barote L., Marinescu C., Cirstea M.N. Control structure for single-phase stand-alone wind-based energy sources. *IEEE Transactions on Industrial Electronics*, 2013, vol. 60, no. 2, pp. 764-772. doi: 10.1109/TIE.2012.2206346.
- Badran O. Wind turbine utilization for water pumping in Jordan. *Journal of Wind Engineering and Industrial Aerodynamics*, 2003, vol. 91, no. 10, pp. 1203-1214. doi: 10.1016/S0167-6105(03)00073-4.
- Malinowski M., Kazmierkowski M.P., Trzynadlowski A. Review and comparative study of control techniques for three-phase PWM rectifiers. *Mathematics and Computers in Simulation*, 2003, vol. 63, no. 3-5, pp. 349-361. doi: 10.1016/S0378-4754(03)00081-8.
- Larrinaga S.A., Vidal M. A. R., Oyarbide E., Apraiz J. R. T. Predictive control strategy for DC/AC converters based on direct power control. *IEEE Transactions on Industrial Electronics*, 2007, vol. 54, no. 3, pp. 1261-1271. doi: 10.1109/TIE.2007.893162.
- Mendis N., Muttaqi K.M., Perera S. Management of battery-supercapacitor hybrid energy storage and synchronous condenser for isolated operation of PMSG based variable-speed wind turbine generating systems. *IEEE Transactions on Smart Grid*, 2014, vol. 5, no. 2, pp. 944-953. doi: 10.1109/TSG.2013.2287874.
- Noguchi T., Tomiki H., Kondo S., Takahashi I., Katsumata J. Instantaneous active and reactive power control of PWM converter by using switching table. *IEEE Transactions on Industry Applications*, 1996, vol. 116, no. 2, pp. 222-223. doi: 10.1541/ieejias.116.222.
- Idir A., Kidouche M. Direct torque control of three phase induction motor drive using fuzzy logic controllers for low torque ripple. *Proceedings Engineering & Technology*, 2013, vol. 2, pp. 78-83.
- Boukhechem I., Boukadoum A., Boukelkoul L., Lebied R. Sensorless direct power control for three-phase grid side converter integrated into wind turbine system under disturbed grid voltages. *Electrical engineering & electromechanics*, 2020, no. 3, pp. 48-57. doi: 10.20998/2074-272X.2020.3.08.
- Mirecki A., Roboam X., Richardeau F. Architecture complexity and energy efficiency of small wind turbines. *IEEE Transactions on Industrial Electronics*, 2007, vol. 54, no. 1, pp. 660-670. doi: 10.1109/tie.2006.885456.

14. Tran D.-H., Sareni B., Roboam X., Espanet C. Integrated optimal design of a passive wind turbine system: an experimental validation. *IEEE Transactions on Sustainable Energy*, 2010, vol. 1, no. 1, pp. 48-56. doi: **10.1109/tste.2010.2046685**.
15. Cho Y., Lee K.-B., Song J.-H., Lee Y.I. Torque-ripple minimization and fast dynamic scheme for torque predictive control of permanent-magnet synchronous motors. *IEEE Transactions on Power Electronics*, 2015, vol. 30, no. 4, pp. 2182-2190. doi: **10.1109/TPEL.2014.2326192**.
16. Chinchilla M., Arnaltes S., Burgos J.C. Control of permanent-magnet generators applied to variable-speed wind-energy systems connected to the grid. *IEEE Transactions on Energy Conversion*, 2006, vol. 21, no. 1, pp. 130-135. doi: **10.1109/TEC.2005.853735**.
17. Kim H.-W., Kim S.-S., Ko H.-S. Modeling and control of PMSG-based variable-speed wind turbine. *Electric Power Systems Research*, 2010, vol. 80, no. 1, pp. 46-52. doi: **10.1016/j.epsr.2009.08.003**.
18. Seyoum D., Rahman M.F., Grantham C. Terminal voltage control of a wind turbine driven isolated induction generator using stator oriented field control. *Eighteenth Annual IEEE Applied Power Electronics Conference and Exposition*, 2003. APEC '03. doi: **10.1109/APEC.2003.1179315**.
19. Bouafia A., Gaubert J.-P., Krim F. Predictive direct power control of three-phase pulsewidth modulation (PWM) rectifier using space-vector modulation (SvM). *IEEE Transactions on Power Electronics*, 2010, vol. 25, no. 1, pp. 228-236. doi: **10.1109/TPEL.2009.2028731**.
20. Malinowski M., Kazmierkowski M.P., Trzynadlowski A. Review and comparative study of control techniques for three-phase PWM rectifiers. *Mathematics and Computers in Simulation*, 2003, vol. 63, no. 3-5, pp. 349-361. doi: **10.1016/S0378-4754(03)00081-8**.
21. Bouafia A., Gaubert J.-P., Krim F. Analysis and design of new switching table for direct power control of three-phase PWM rectifier. *2008 13th International Power Electronics and Motion Control Conference*, Sep. 2008. doi: **10.1109/epemc.2008.4635347**.
22. Hussein M.M., Senjyu T., Orabi M., Wahab M.A.A., Hamada M.M. Load power management control for a stand alone wind energy system based on the state of charge of the battery. *2012 IEEE International Conference on Power and Energy (PECon)*, Dec. 2012. doi: **10.1109/pecon.2012.6450352**.
23. Noguchi T., Tomiki H., Kondo S., Takahashi I. Direct power control of PWM converter without power-source voltage sensors. *IEEE Transactions on Industry Applications*, 1998, vol. 34, no. 3, pp. 473-479. doi: **10.1109/28.673716**.
24. Ohnuki T., Miyashita O., Lataire P., Maggetto G. Control of a three-phase PWM rectifier using estimated AC-side and DC-side voltages. *IEEE Transactions on Power Electronics*, 1999, vol. 14, no. 2, pp. 222-226. doi: **10.1109/63.750174**.
25. Benbouhenni H., Boudjema Z. Comparative study between neural hysteresis, fuzzy PI, and neural switching table for an IM DTC control. *Proceedings of the World Congress on Engineering and Computer Science*, 2018, vol. 5.
26. Bouafia A., Krim F., Gaubert J.-P. Design and implementation of high performance direct power control of three-phase PWM rectifier, via fuzzy and PI controller for output voltage regulation. *Energy Conversion and Management*, 2009, vol. 50, no. 1, pp. 6-13. doi: **10.1016/j.enconman.2008.09.011**.

Received 05.09.2020

Accepted 19.10.2020

Published 24.12.2020

Ryma Lebled¹, Ph.D.,
Rachid Lalalou¹, Doctor of Electrotechnical,
Hocine Benalla², Doctor of Electrotechnical, Professor,
Khalil Nebti², Doctor of Electrotechnical,
Ismail Boukhechem¹, Ph.D.,

¹ Electrotechnical Laboratory Skikda (LES),
University 20 August 1955,
Department of Electrical Engineering,
26 Road El Hadaiek 21000, Skikda, Algeria.

² Electrical Engineering Laboratory of Constantine, LEC,
Department of Electrical Engineering,
University of Constantine 1, 25000 Constantine, Algeria.
e-mail: r.lebled@univ-skikda.dz; rlalalou@yahoo.fr;
benalladz@yahoo.fr; idor2003@gmail.com;
sameu25@gmail.com

How to cite this article:

Lebled R., Lalalou R., Benalla H., Nebti K., Boukhechem I. Ameliorate direct power control of standalone wind energy generation system based on permanent magnet synchronous generator by using fuzzy logic control. *Electrical engineering & electromechanics*, 2020, no. 6, pp. 63-70. doi: **10.20998/2074-272X.2020.6.09**.

Матеріали приймаються за адресою:

Кафедра "Електричні апарати", НТУ "ХПИ", вул. Кирпичова, 21, м. Харків, 61002, Україна

Електронні варіанти матеріалів по e-mail: a.m.grechko@gmail.com

Довідки за телефонами: +38 050 653 49 82 Клименко Борис Володимирович

+38 067 359 46 96 Гречко Олександр Михайлович

Передплатний індекс: 01216